Growth of InAs photodiode structures from metalorganic compounds

S. S. Kizhaev, M. P. Mikhaĭlova, C. C. Molchanov, N. D. Stoyanov, and Yu. P. Yakovlev

A. F. Ioffe Physicotechnical Institute, Russian Academy of Sciences, St. Petersburg
(Submitted October 15, 1997)
Pis'ma Zh. Tekh. Fiz. **24**, 1–7 (April 12, 1998)

InAs layers were grown on *p*-InAs substrates by epitaxy from metalorganic compounds. Photodiodes were fabricated using the *p–n* junctions obtained. The current–voltage, capacitance–voltage, and spectral characteristics of the photodiode structures were investigated. © *1998 American Institute of Physics.* [S1063-7850(98)00104-9]

Indium arsenide is of interest as a material for infrared optoelectronic devices. Photodiodes, light-emitting diodes, and lasers operating in the 2–5 μm range, which is important for gas analysis and environmental monitoring, can be produced from InAs in combination with multicomponent solid solutions (InAsSb, InAsSbP, and others).[1–3] The materials were grown mainly by liquid-phase epitaxy (LPE), but also by epitaxy from metalorganic compounds (MOC).[4–10] In the present Letter we report the results of investigations of InAs layers obtained on InAs substrates by epitaxy from MOC as well as the results of measurements of the electric and photoelectric properties of the structures obtained.

The InAs layers were grown by epitaxy from MOC in a planar reactor 30 cm in diameter at atmospheric pressure. The substrate holder was heated with a three-zone resistance heater, separated from the interior volume of the chamber by

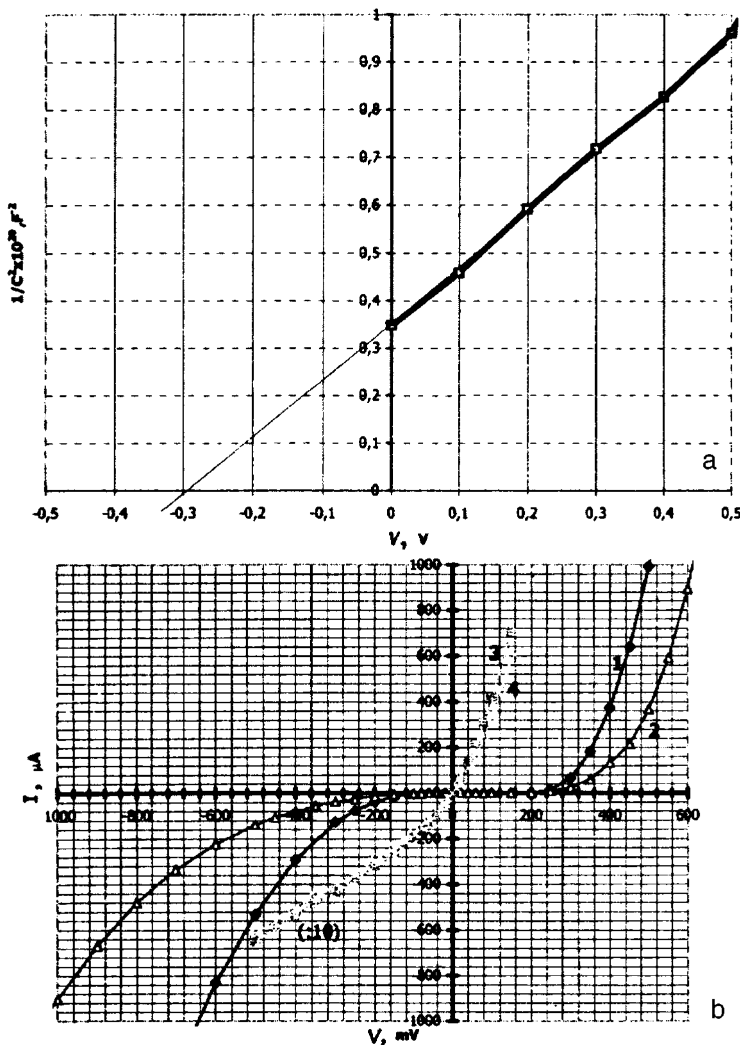

FIG. 1. a — Capacitance versus reverse bias for InAs photodiode structure No. 96 at $T=77$ K; b — current–voltage characteristics of InAs photodiode structures Nos. 95 and 96 at $T=77$ K (curves *1* and *2*, respectively) and $T=300$ K (curves *3* and *4*).

 © 1998 American Institute of Physics

a quartz cap. The vapor-gas mixture was fed from the periphery of the cap to the center. The substrates rotated about the central axis. Arsine (AsH_3) diluted to 20% in hydrogen and trimethyl indium (TMI) served as sources of arsenic and indium, respectively. The temperature of the evaporator with TMI was +18 °C. To avoid parasitic reactions, the AsH_3 and TMI were fed into the reactor through separate channels and mixing occurred in the reactor chamber. In all experiments, an additional hydrogen flow (30 liters/min) from the top zone of the chamber in a direction perpendicular to the substrates was used to decrease parasitic deposition on the chamber walls. Zinc-doped p-InAs (100) substrates (carrier density $p=1\times10^{17}$ cm^{-3} at $T=300$ K and $p=6\times10^{15}$ cm^{-3} at $T=77$ K) were used in all experiments. Before each process the substrates were washed in carbon tetrachloride and isopropyl alcohol, etched,[11] washed in distilled water, dried, and immediately loaded into the reaction chamber. The experiments were performed in the temperature range 450–600 °C. The AsH_3 flows were varied in the interval 10–125 ml/min, while the hydrogen flows through the evaporator with TMI were varied in the interval 200–400 ml/min. The molar ratio AsH_3/TMI ranged from 2.5 to 50. TMI was fed into the reactor 2 min after the AsH_3 flow was turn on.

At substrate temperatures below 500 °C the surface of the layers appeared porous, probably because of weak decomposition of arsine at low temperatures. The layers grown at temperatures close to 600 °C were shiny. The layers grew at an average rate of less than 0.5 μm/h.

Hall coefficient measurements showed n-type conduction. The p–n structures grown were used to produce photodiodes. The photosensitive structures in the form of mesa-diodes with a n layer were prepared by conventional photolithography. The diameter of the sensitive area was equal to 600–800 μm. The current–voltage, capacitance–voltage, and spectral characteristics of the photodiode structures at temperatures 77 and 300 K were investigated. Capacitance was measured by the standard bridge method at 1 MHz. The photoresponse spectra were measured with a SPM-2 monochromator with a LiF prism and a globar as the radiation source.

The voltage dependence of the capacitance corresponded to the law $1/C^2\sim V$ (Fig. 1a) and attested to the presence of a sharp p–n junction. The capacitance was much lower than that in ordinary InAs photodiodes prepared by LPE and fell within the interval 100–200 pF with zero bias for diodes 1 mm in diameter. These data were used to estimate the charge carrier density in the layer, 10^{16} cm^{-3} at $T=77$ K, and the width of the space charge region, 2×10^{-5} cm $(V=0)$. The experimental structure was close to a p–i–n photodiode and should possess a fast response $\tau<1$ ns, determined by the product RC, where R is the series resistance of the p–n junction.

Figure 1b displays the current–voltage characteristics for two photodiodes (Nos. 95 and 96) at $T=77$ K and $T=300$ K. At voltages up to 100 mV ($T=77$ K) the reverse currents were equal to several nanoamperes. The voltage intercept on the abscissa for the forward branch was equal to $V=0.3$ V. The differential resistance in the experimental diodes with zero bias fell within the range $R_0=100-700$ kΩ (77 K) and

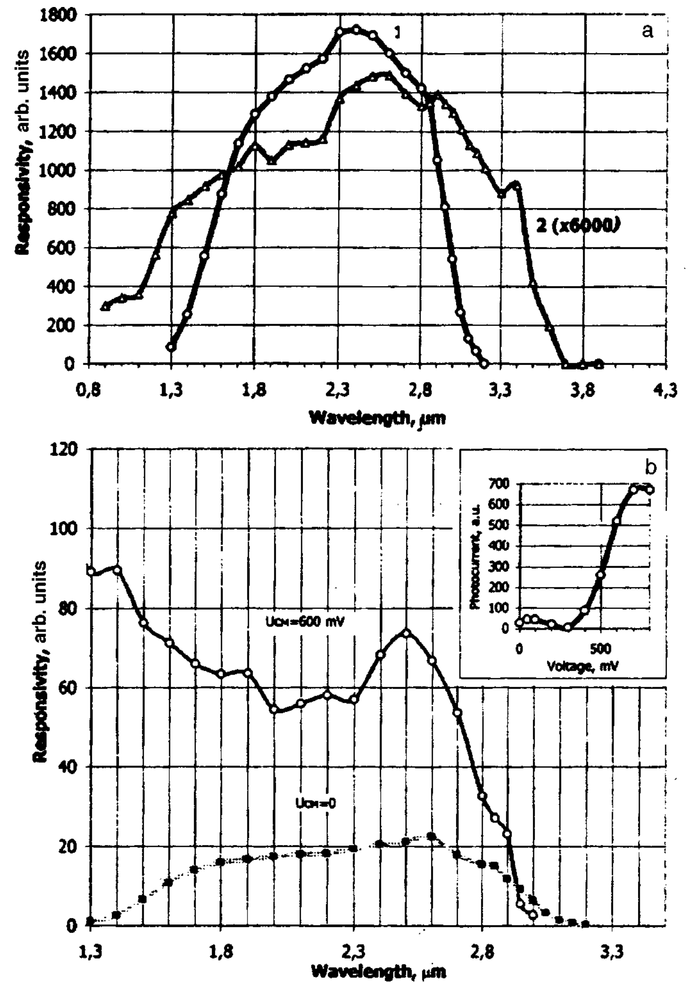

FIG. 2. a — Photosensitivity spectra of an InAs photodiode (No. 95) at $T=77$ K (curve *1*) and $T=300$ K (curve *2*). b — Photosensitivity spectrum of the photodiode structure No. 95 with zero bias (curve *1*) and with a reverse bias of 600 mV (curve *2*). Inset: Photocurrent versus reverse bias under illumination with $\lambda=1.5$ μm monochromatic light.

$R_0=30-55$ Ω (300 K), depending on the growth regimes. The reverse current at low temperatures in the region up to 500 mV was determined by generation and recombination in the space-charge layer[13]

$$I_{G-R}=qn_iWA/\tau_{\rm eff}, \quad (1)$$

where q is the electron charge, A is the area of the p–n junction, n_i is the intrinsic charge-carrier density, and $\tau_{\rm eff}$ is the effective lifetime. The value obtained $\tau_{\rm eff}=6\times10^{-6}$ s agrees well with the radiative recombination time in p-InAs.[12]

Figure 2a shows the photosensitivity spectra of the InAs photodiode structure at two temperatures. An estimate of the band gap according to the half-maximum of the sensivity gives $h\nu=0.423$ eV ($\lambda_{1/2}=2.93$ μm) at 77 K and $h\nu=0.360$ eV ($\lambda_{1/2}=3.43$ μm) at 300 K. High power–voltage sensitivities, reaching 20 kV/W, were obtained at 77 K. As the temperature increased to room temperature, the photosensitivity decreased in inverse proportion to R_0. It was observed that the photoresponse increased rapidly with the application of a reverse voltage in the interval from 300 to 800 mV (inset in Fig. 2b) and illumination with strongly ab-

sorbed light ($\lambda = 1.5\ \mu$m). At the same time the photocurrent gain reached 35–40. This effect is most likely due to avalanche multiplication of holes from the *n* layer in the strong field of the space charge region. As shown in Ref. 12, the electric field for initiating impact ionization in InAs for holes from the spin-orbit split band is low and equals $E \cong 4 \times 10^4$ V/cm.

We also calculated the thermal noise in the experimental InAs photodiodes ($i^2 = 4kT\Delta f/R_0$) and estimated the detectivity at the wavelength of the maximum of the spectrum according to the well-known formula[13]

$$D^*(\mathrm{cm}\cdot\mathrm{Hz}^{1/2}\cdot\mathrm{W}^{-1}) = A^{1/2}/\mathrm{NEP}, \qquad (2)$$

where A is the area of the photodiode and NEP (W/Hz$^{1/2}$) is the noise-equivalent power. Estimating the quantum efficiency of the photodiode as $\eta = 0.7$, taking into account the reflection coefficient of the surface, we obtained the photosensitivity $S = 1.6$ A/W at 77 K and 1.42 A/W at 300 K. The detectivity varied from $D^*_\lambda = 1.2 \times 10^{11}$ cm $\cdot$ Hz$^{1/2}\cdot$ W^{-1} at 77 K down to $D^*_\lambda = 10^9$ cm $\cdot$ Hz$^{1/2}\cdot$ W^{-1} at 300 K. These data are comparable to standard commercial InAs photodiodes (see Ref. 14).

In summary, samples of photosensitive *n*-InAs layers on bulk *p*-InAs substrates were prepared by epitaxy from MOC. It was shown that this technology holds promise for producing high-efficiency photodiode structures. Further improvement of the technology will make it possible not only to improve substantially the characteristics of InAs photodiodes but also to develop the foundation for growing ternary and quaternary compounds based on indium arsenide.

We thank M. N. Mizerov and B. V. Pushnyĭ for supporting this work and also A. S. Usikov for helpful suggestions.

[1] T. N. Danilova, O. G. Ershov, A. N. Imenkov, M. V. Stepanov, V. V. Shersnev, and Yu. P. Yakovlev, Fiz. Tekh. Poluprovodn. **30**, 1244 (1996) [Semiconductors **30**, 656 (1996)].
[2] H. K. Choi, G. W. Turner, and S. J. Eglash, IEEE Photonics Technol. Lett. **6**, 7 (1994).
[3] M. P. Mikhaĭlova, S. V. Slobodchikov, N. D. Stoyanov, N. M. Stus', and Yu. P. Yakovlev, Pis'ma Zh. Tekh. Fiz. **22**(8), 63 (1996)) [Tech. Phys. Lett. **22**, 672 (1996)].
[4] B. Baliga and K. Ghandhi, J. Electrochem. Soc. **121**, 1642 (1974).
[5] T. Fukui and Y. Horikoshi, Jpn. J. Appl. Phys. **18**, 2157 (1979).
[6] T. Fukui and Y. Horikoshi, Jpn. J. Appl. Phys. **19**, L551 (1980).
[7] T. Fukui and Y. Horikoshi, Jpn. J. Appl. Phys. **20**, 587 (1981).
[8] S. K. Haywood, R. W. Martin, N. J. Mason, and P. J. Walker, J. Cryst. Growth **97**, 489 (1989).
[9] R. M. Biefeld, K. C. Baucom, and S. R. Kurtz, J. Cryst. Growth **137**, 231 (1994).
[10] W. Duncan, A. S. M. Ali, E. M. Marsh, and P. C. Spurdens, J. Cryst. Growth **143**, 155 (1994).
[11] *Etching of Semiconductors*, Mir, Moscow, 1965.
[12] M. Levinshtein, S. Rumyantsev and M. Shur [Eds.], *Handbook Series on Semiconductor Parameters*, World Scientific Publish. Co. Pte. Ltd, Vol. 1.
[13] S. Sze, *Physics of Semiconductor Devices*, Wiley, N. Y.; Mir, Moscow, 1984.
[14] *Infrared Detectors*, EG & G Optoelectronic JUDSON, 1995, 53 pp.

Translated by M. E. Alferieff
Edited by David L. Book

Behavior of epitaxial GaAs layers as α particle detectors

V. M. Botnaryuk, Yu. V. Zhilyaev, A. M. Ivanov, N. B. Strokan, and L. M. Fedorov

A. F. Ioffe Physicotechnical Institute, Russian Academy of Sciences, St. Petersburg

(Submitted October 9, 1997)
Pis'ma Zh. Tekh. Fiz. **24**, 8–15 (April 12, 1998)

The properties of epitaxial GaAs-based p^+-n structures used as light-ion (α particle) were studied. A comparison is made with the latest published data on the possibilities of present-day semi-insulating GaAs (SI–GaAs). It is noted that the content of impurities and structural defects forming deep levels in the band gap of the material is two orders of magnitude lower in epitaxial layers. The deep levels determine the conditions of transport of nonequilibrium carriers in the detector, allowing for trapping of the carriers, and they also determine the electric-field profile. The charge-carrier lifetime was found to be $\geqslant$200 ns. This is two orders of magnitude longer than the values for SI–GaAs, in complete agreement with the lower content of deep centers. It is shown how deep centers influence the field profile, forming a quite large region of low field values. © *1998 American Institute of Physics.* [S1063-7850(98)00204-3]

The first attempts to use epitaxial GaAs as nuclear-radiation detectors were made back in the 1970s.[1,2] The authors were attracted by the possibility that the detectors could operate at room temperature because the band gap is larger than in the traditional material Si (and correspondingly the reverse currents and noise are lower). The higher stopping power of GaAs is also a substantial advantage over Si. Ultimately, emphasis was placed on the spectrometry of characteristic x-ray radiation (energy <100 keV) in problems of analyzing the composition of materials (see, for example, Ref. 3).

Recently, great interest in semi-insulating GaAs (SI–GaAs) has appeared in high-energy physics. The problem is to produce detectors with the maximum possible working region, represented by the electric-field region of a reverse-biased p^+-n structure. An obvious obstacle here is the high degree of conductivity compensation in SI–GaAs. This is due to a high density of impurities and intrinsic defects that form deep levels (DLs) in the band gap of the material. The deep levels participate both in the formation of the electric-field region in the reverse-biased structure of the detector and in the trapping of nonequilibrium current carriers. In this connection charge transfer in SI–GaAs detectors as well as the many DLs present in SI–GaAs are being studied intensively. In Ref. 4 seven levels at depths in the range 0.15–0.81 eV were found.

It is of interest to observe the manifestation of DLs in GaAs detectors under conditions when their number is much lower than in SI–GaAs. To this end, in the present work the structures of the detectors were fabricated using $\simeq 100$ μm epitaxial-GaAs layers. Alpha particles were used as the radiation source. Deep-level-induced features of nonequilibrium-carrier transport, the parameters of the deep centers (DCs) present in the material, and the capacitance of the detector as a function of the reverse bias were analyzed.

1. Layers n^0-GaAs on a n^+-GaAs substrate were obtained in an open chloride system.[5] Ga and $AsCl_3$ with a purity of 99.9999% were used directly as sources of gallium and arsenic. The perfection of the layers with respect to the content of DLs was monitored by capacitance methods (measurement of the capacitance–voltage characteristics) as well as DLTS spectra.

The first characteristic was seen in the dependence of the reciprocal of the capacitance versus the bias. Specifically, $1/C$ was found to be a linear function, if U instead of $\sqrt{U}$ is used as the abscissa. A model for explaining this dependence in the case of SI–GaAs has recently been advanced in the literature.[6] The model is based on the appearance of an imbalance between the electron-capture–emission cross sections of the dominant level EL2 in fields 10^4-10^5 V/cm. However, in our case the fields were weaker. Moreover, two sections with different impurity densities 1.1×10^{14} cm^{-3} and 2.3×10^{13} cm^{-3} were clearly distinguished in the conventional coordinates $1/C=f(\sqrt{U})$ (Fig. 1). For this reason, we are inclined to interpret the observation of a linear variation $1/C=f(U)$ as an approximation (in a comparatively narrow voltage interval) of the complicated capacitance variation caused by a decrease of the impurity density into the volume of the film.

The construction of Fig. 1 revealed at the same time the presence of a depletion region at the coordinate $U+U_c=0$, where U_c is the contact potential difference. The appearance of such a region is explained by the fact that the occupancy of levels below the Fermi level (E_F) does not change even under nonequilibrium conditions.[7,8] For this reason, the compensation of, say, shallow donors (N_D) by deep acceptors (N_A) persists over a distance

$$w\sim\sqrt{(E_F-E_A)/(N_D-N_A)},$$

where E_A is the position of an acceptor center. For the sample in Fig. 1 we have $w=11.8$ μm. We stress that the data in Fig. 1 were obtained at temperature 78 K with probe signal frequency $f=100$ kHz. However, virtually the same values of w correspond to room temperature and frequency

 © 1998 American Institute of Physics

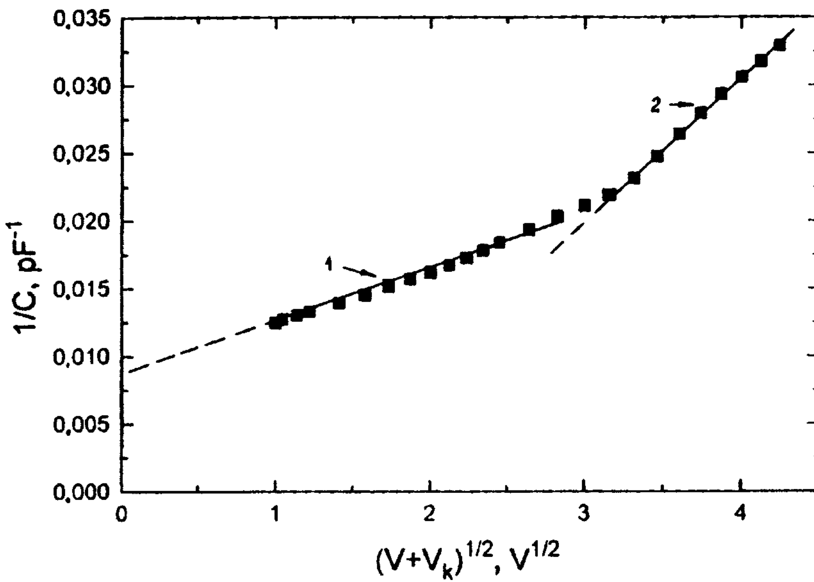

FIG. 1. Reciprocal of the capacitance versus the blocking bias on a $p^+-n_0-n^+$ GaAs structure with an epitaxial base layer. Measurement conditions: temperature 78 K; probe signal frequency 100 kHz. Impurity density in sections *1* and *2* respectively: 1.1×10^{14} and 2.3×10^{13} cm^{-3}.

$f=1$ kHz. This shows that levels located at depths of less than 0.45 eV participate in compensation ($\sigma=3\times10^{-14}$ cm^{-2} was taken for trapping cross section). The position and density of the levels were determined directly by DLTS. The spectra showed the presence of three DLs, exchanging majority carriers with the conduction band. A hole-injection regime was used to investigate the bottom half of the band. Three DLs exchanging holes with the valence band were also found here. The main DCs located at $E_c-0.81$ eV and possessing an electron trapping cross section $\sigma_n=1\times10^{-13}$ cm^2 (EL2 in the conventional terminology) were present with density $\sim5\times10^{13}$ cm^{-3}, i.e., very low compared with SI–GaAs. The density of centers located at $E_c-0.48$ eV ($\sigma_n=2.7\times10^{-15}$ cm^2) and $E_v+0.52$ eV ($\sigma_p=2.4\times10^{-16}$ cm^2) was also $\leqslant3\times10^{13}$ cm^{-3}. The content of shallower centers was approximately an order of magnitude lower. Therefore such centers will not determine the characteristics of the material. This latter conclusion agrees with the result of the capacitance measurements presented above.

Since EL2 is, according to the data of Ref. 9 , one of the DCs responsible for recombination, its comparatively low content serves as a prerequisite for a high charge-carrier lifetime. Correspondingly, nonequilibrium-charge transport in the detectors should occur with low trapping losses.

2. The detector characteristics of the structures were measured for ≈5.8 MeV α particles from Cm^{244}. The standard arrangement was used: charge preamplifier—amplifier—pulse-height analyzer. The transmission band of the amplifier was formed by ladder differentiation–integration circuits with a time constant of 1 μs. Figures 2a and 2b show, respectively, the variation of the normalized signal amplitude and the line width as functions of the length W of the field region. Note that the particle range was $R=21.6$ μm, while W was varied by changing the voltage on the detector. Normalization was done with respect to the Si signal of a high-precision detector, taking account of the ratio of the average electron–hole pair production energies.

One can see from Fig. 2a that three sections appear in the increase of the amplitude. The steepest rise of the signal is observed in the first section, for $W\leqslant22$ μm. This is followed by a section (up to $W\leqslant33$ μm) of slower, linear growth, which passes into the last section where saturation occurs. We recall that the signal amplitude is proportional to the nonequilibrium charge transported in the field region of the detector. From this position, according to Fig. 2a, the signal behavior can be explained as follows.

For $R<W$ an α-particle track emerges outside the field region and transport of this terminal portion of the charge proceeds by hole diffusion to the boundary of the field. It is obvious that the comparatively slow diffusion is due to large recombination losses of charge. The start of the second section corresponds to the track being wholly contained in the region of the field. However, as the capacitance measurements showed, the field region is divided into two zones with different field strengths (F). In addition, the extent (measured from the surface into the interior of the layer) and the values of F in the second zone are independent of the bias. Another characteristic feature of this zone is the low value of F. However, as bias increases, the extent of and value of F in the first field zone increase. Thus, a dwindling portion of the track falls within the weak-field zone. Since the field separates the charge carriers in the track, preventing carrier recombination, the amplitude continues to grow, but the rate of growth is different from that in the first section.

Finally, when the track falls entirely within the strong-field zone, i.e., $W-w=W-11.8$ μm $\geqslant21.6$ μm, the particle-induced charge is transported quite completely. This corresponds to the signal saturation stage in Fig. 2a. In summary, the following appear successively in the three observed sections: participation of diffusion in charge transport and carrier separation and drift of carriers in weak and strong fields.

As far as the absolute value of the transported charge is concerned, calibration with a Si detector shows a deficit λ of the order of 1% for the plateau (Fig. 2a). This value in turn makes it possible to estimate the carrier lifetime τ from the well-known relation for dense tracks $\lambda=10^{-5}/(F\tau)$, where the value of the field is taken at the center of gravity of the

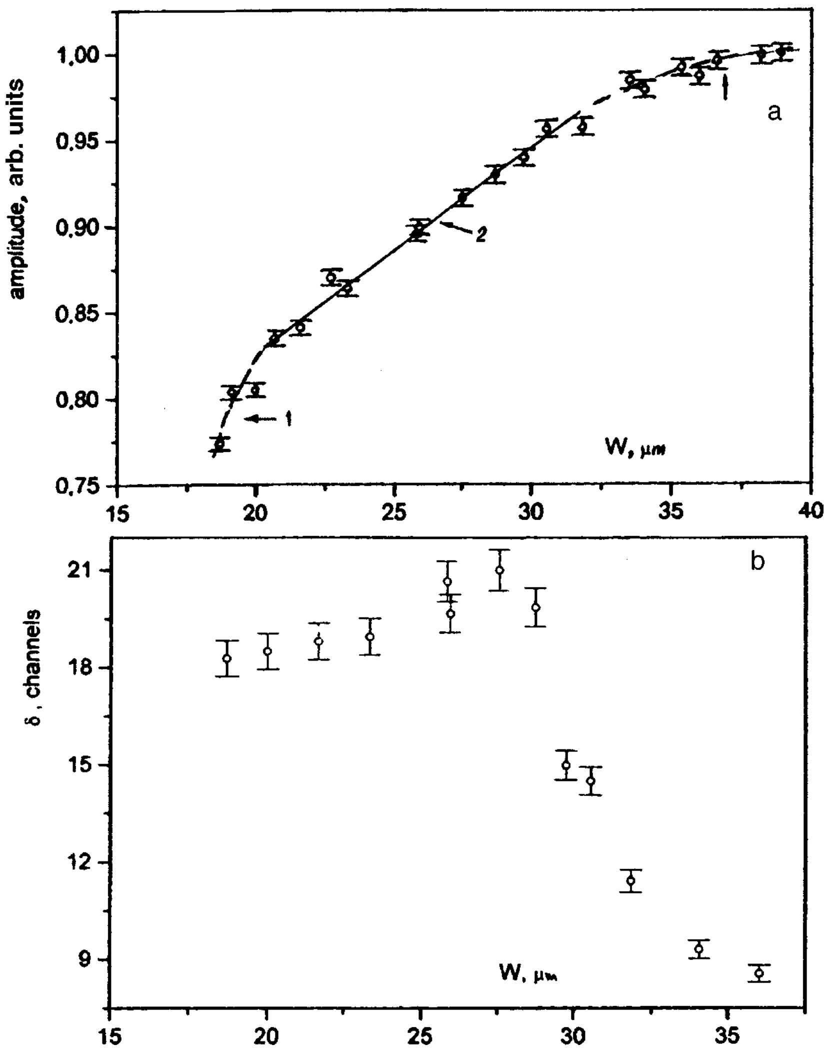

FIG. 2. As functions of the extent W of the electric-field region during the detection of 5.8 MeV α particles: a — Normalized signal amplitude (see text for an explanation of the three observed sections); b — width of the spectral line. The value of the analyzer channel is 8.09 keV.

carrier distribution in the track.[10] For our case we obtain $\tau \geqslant 200$ ns. We note that in Ref. 4 the values $\tau \approx$ ns were obtained for SI–GaAs. The latter should be attributed to the two orders of magnitude higher content of EL2 centers in SI–GaAs.

Figure 2b shows under the same conditions the variation of the width δ of the spectral line at half-maximum. It is known[11] that δ is determined as the product of the charge deficit by the factor γ characterizing the nonuniformity of the losses over the volume. One would think that as the charge losses decrease (the amplitude increases), the line width should decrease monotonically. However, two sections can be distinguished in Fig. 2b: very weak growth up to $W \approx 28$ μm followed by a sharp drop of δ and then a tendency toward saturation. We note that δ starts to decrease before absorption of the track by the strong-field zone.

The observed behavior can be explained qualitatively by the difference in the conditions of carrier spreading and accordingly averaging the fluctuations in the charge losses over the volume of a track. Let us assume that the initial geometry of the track has the the form of a thin filament. It is obvious that in the case when diffusion participates, as well as in weak fields F, before being sorbed on the electrodes of the detector the charge carriers spread over a larger volume than under strong-field conditions. At the same time, the losses are more completely averaged and the nonuniformity factor γ thereby increases. Then, moving leftward from the maximum, the increase in losses λ will be counterbalanced by the decrease in the factor γ. The latter circumstance flattens out the left-hand part of the graph. On the right-hand side of the graph the decrease in charge losses plays the main role, while the factor γ must be assumed to change very little.

Conclusions. The structures of ion detectors based on epitaxial GaAs layers have been fabricated. The characteristics of the structures were compared with the case when SI–GaAs, a semi-insulating material, is used as the initial material.

It was established that the purity of epitaxial GaAs is much higher than that of SI–GaAs. We are referring to the fact that the content of deep centers associated with impurities and structural defects is two orders of magnitude lower.

The comparatively low density of deep centers is manifested nonetheless in the formation of the field region in the reverse-biased structure, forming a ≈ 10 μm weak-field zone.

The carrier lifetime in an α-particle track in our case was $\tau \geqslant 200$ ns, which is two orders of magnitude longer than in the case of SI–GaAs. The lifetime τ completely corre-

sponds to the lower content of deep centers, mainly EL2 structural defects.

We wish to thank V. V. Bel'kov and V. K. Eremin for a helpful discussion.

[1] J. E. Eberhardt, R. D. Ryan, and A. J. Tavendale, NIM, No. 3, 463 (1971).

[2] T. Kobayashi and T. Sugita, NIM, No. 1, 179 (1972).

[3] S. P. Golenestkiĭ, V. M. Zaletin, I. I. Protasov, and A. T. Dudarev, Prib. Tekh. Éksp. , No. 3, 63 (1980).

[4] F. Nava, M. Alietti, C. Canali, A. Cavallini, C. Chiossi, C. Papa, V. Re, and C. Lanzieri, IEEE Trans. Nucl. Sci. **43**, 1130 (1996).

[5] Yu. V. Zhilyaev, *Doctoral Dissertation in Mathematical Physics*, A. F. Ioffe Physicotechnical Institute, Russian Academy of Sciences, Leningrad, 1991.

[6] D. S. McCregor, R. A. Rojeski, G. F. Knoll, F. L. Terry, J. East, and Y. Eisen, J. Appl. Phys. **75**, 7910 (1994).

[7] C. T. Sah and V. G. K. Reddi, IEEE Trans. Electron Devices **ED-11**, 345 (1964).

[8] L. L. Makovskiĭ, S. M. Ryvkin, N. B. Strokan, V. P. Subasheva, and A. Kh. Khusainov, *Physics of Electron–Hole Transitions and Semiconductor Devices* [in Russian], Nauka, Moscow, 1969, p. 88.

[9] V. M. Botnaryuk, Yu. V. Zhilyaev, A. G. Kechek, N. I. Kuznetsov, A. A. Lebedev, and Yu. N. Shul'ga, Pis'ma Zh. Tekh. Fiz. **14**, 181 (1988) [Sov. Tech. Phys. Lett. **14**, 80 (1988)].

[10] A. Quaranta, A. Taroni, and G. Zanarini, IEEE Trans. Nucl. Ser. **15**, 373 (1968).

[11] E. M. Verbitskaya, V. K. Eremin, A. M. Malyarenko, N. B. Strokan, and V. L. Sukhanov, Fiz. Tekh. Poluprovodn. **21**, 1883 (1987) [Sov. Phys. Semicond. **21**, 1140 (1987)].

Translated by M. E. Alferieff

Edited by David L. Book

Recombination properties of silicon passivated with rare-earth oxide films

A. I. Petrov and V. A. Rozhkov

Samara State University

(Submitted July 23, 1997)
Pis'ma Zh. Tekh. Fiz. **24**, 16–21 (April 12, 1998)

The recombination properties of silicon passivated with films of rare-earth oxides were investigated. The films were obtained by thermal resistive sputtering of a rare-earth metal followed by thermal oxidation of the obtained layer in air at 400 °C. It was established that the effective nonequilibrium charge-carrier lifetime measured by photoconductivity relaxation is 2–3 times higher after deposition of the rare-earth oxide film. Surface recombination rates at the silicon–rare-earth oxide interface were determined to be 290–730 cm/s for different rare-earth oxides. The combination of high optical transmittance of the experimental materials and low recombination losses in silicon coated with a rare-earth oxide film makes it possible to recommend rare-earth oxide films as optical antireflection and passivating coatings for silicon photoelectric devices. © *1998 American Institute of Physics.* [S1063-7850(98)00304-8]

Among materials showing promise as antireflection coatings for silicon photoelectric devices, rare-earth oxides are noted for their high transmittance in the working region of the spectrum, chemical and thermal stability, and optimal refractive index for this application. Investigations have shown[1,2] that the spectral reflectance of a silicon surface can be decreased to 0.01–1.2% and the spectral value of the short-circuit photocurrent of a silicon photoelectric transducer can be increased by more than 50% by depositing on the silicon surface a film consisting of an oxide of a rare-earth element. An important requirement for optical coatings of semiconductor devices is that the interface with the semiconductor must possess low recombination losses. However, the recombination characteristics of silicon coated with a rare-earth oxide film have still not been determined. In this connection, in the present work we investigated the effective lifetime and surface recombination rate of nonequilibrium charge carriers in silicon wafers passivated with films of some rare-earth oxides.

The experimental samples were cut from polished wafers of KÉF-20 single-crystal (100) silicon and had characteristic dimensions $10\times5\times0.34$ mm. Prior to the preparation of a rare-earth oxide film, the silicon wafers were subjected to chemical treatment for the purpose of removing the natural oxide. The treatment consisted of etching in a water solution of hydrofluoric acid with the composition $HF:H_2O$ (1:10). In some cases, after this treatment the samples were boiled in an ammonium hydroxide–hydrogen peroxide solution (APS) with the composition $NH_4OH:H_2O_2:H_2O$ (1:1:3). After each chemical treatment the samples were repeatedly washed in twice-distilled water and dried on a filter. Cerium, europium, dysprosium, samarium, yttrium, gadolinium, and ytterbium oxide films were prepared on both surfaces of the silicon wafer by thermal oxidation of a predeposited layer of rare-earth metal in air at 400 °C for 30 min. The rare-earth metal film was deposited by thermal sputtering from a molybdenum boat in a 10^{-5} Torr vacuum in a VUP-4 apparatus. Dysprosium and aluminum, successively deposited on silicon samples through a stencil by thermal sputtering in vacuum, were used as ohmic contacts. The ohmicity of the contacts was determined from measurements of the (linear) voltage drop distribution along the sample.

The effective lifetime τ was measured by the widely used method of photoconductivity relaxation with the sample illuminated with square light pulses. An AL-106A gallium phosphide light-emitting diode, to which square current pulses from a G6-26 generator were fed at a repetition frequency of 1 kHz, was used as the light source. The kinetics of the voltage drop on the sample was measured with a S1-112 oscillograph. The temperature dependences of the effective lifetime were measured in the temperature range 290–410 K in a 10^{-1} Torr vacuum.

It is well known[3] that the effective lifetime is determined by the combined effect of recombination and trapping of carriers in the interior and on the surface of the semiconductor. The presence of traps for charge carriers can have a large effect on the time constant of photoconductivity decay measured by this method, as a result of which the value obtained

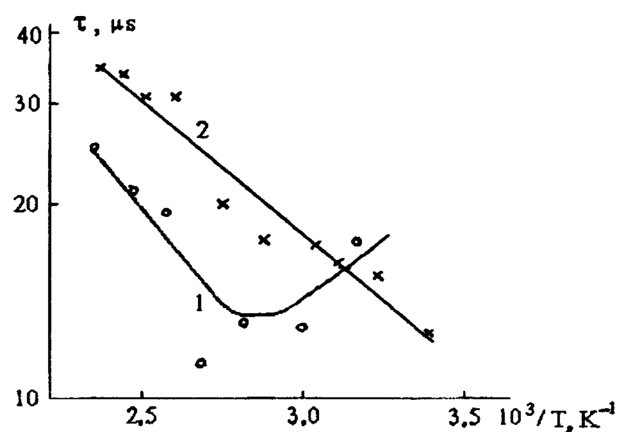

FIG. 1. Temperature dependence of the effective lifetime of nonequilibrium charge carriers in silicon without a coating (*1*) and with a dysprosium oxide film (*2*).

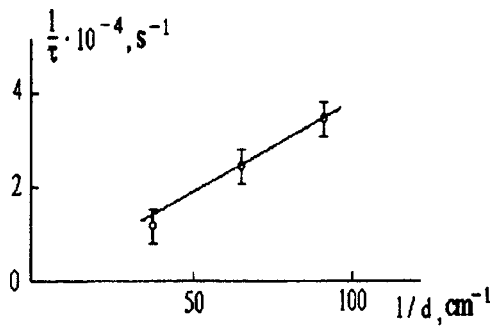

FIG. 2. Effective lifetime of nonequilibrium charge carriers in a silicon wafer versus the wafer thickness.

TABLE II. Effective lifetimes and surface recombination rates in silicon at 400 K.

Film material	Form of silicon surface treatment	τ, μs	S, cm/s
no film	$HF:H_2O$	18.5	920
CeO_2	$HF:H_2O$	24	720
Dy_2O_3	$HF:H_2O$ + APS	50	340
Gd_2O_3	$HF:H_2O$	23	730
Gd_2O_3	$HF:H_2O$ + APS	54	330
Yb_2O_3	$HF:H_2O$ + APS	58	290
Y_2O_3	$HF:H_2O$ + APS	30	520
Y_2O_3	$HF:H_2O$	54	310

for the carrier lifetime is higher than the real value. To clarify the role of trapping in the relaxation of photoconductivity, the temperature dependence of the time constant of photoconductivity decay kinetics, presented in Fig. 1, was investigated. As one can see from the figure, the effective lifetime for samples without a rare earth oxide film (curve *1*) at first decreases with increasing temperature, and then increases at temperatures above 340 K. A dependence of this form is characteristic for a real silicon surface,[4] the descending section being determined by trapping and the ascending section by recombination of charge carriers on the silicon surface. For silicon samples coated with a rare-earth oxide film (curve *2*, Fig. 1) τ increases monotonically with temperature. This growth is due to surface recombination. These results attest to the fact that for high measurement temperatures $T \geqslant 370$ K attachment can be neglected for all experimental samples. In this case, the effective lifetime for thin samples with a comparatively low surface recombination rate can be expressed as[4]

$$\frac{1}{\tau}=\frac{1}{\tau_0}+\frac{2S}{d},$$

where τ_0 is the lifetime of nonequilibrium charge carriers in the volume of the semiconductor, d is the thickness of the semiconductor, and S is the surface recombination rate. This formula makes it possible to find the surface recombination rate if the volume lifetime is known.

TABLE I. Effective lifetimes in silicon samples before (τ^{in}) and after (τ^f) deposition of a rare-earth oxide film at temperature 293 K.

Film material	Form of silicon surface treatment	τ^{in}, μs	τ^f, μs
CeO_2	$HF:H_2O$	11.3	25.3
Eu_2O_3	$HF:H_2O$	9	13
Dy_2O_3	$HF:H_2O$	8.5	11.9
Gd_2O_3	$HF:H_2O$	9	18.3
CeO_2	$HF:H_2O$ + APS	16	34–36
Dy_2O_3	$HF:H_2O$ + APS	18–19	31–34
Dy_2O_3	$HF:H_2O$ + APS	18	31
Y_2O_3	$HF:H_2O$ + APS	19	23
Y_2O_3	$HF:H_2O$	11	31
Sm_2O_3	$HF:H_2O$	9	13–17

The dependence of the effective lifetime on the thickness of the semiconductor sample was used to determine the volume lifetime. Figure 2 shows the indicated dependence, obtained from measurements of τ, for samples of different thickness, prepared by etching silicon in SR-8 etchant consisting of a 3:1 mixture of nitric and hydrofluoric acids. The experimental values follow well a straight line in the coordinates $1/\tau$ versus $1/d$. This result is evidence that the surface recombination rate is constant for samples of different thickness. This was to be expected, considering that the surface treatment conditions during sample preparation were the same. The estimated volume lifetime determined from the experimental dependences is $\tau_0 \geqslant 250$ μs for all experimental samples.

Table I shows the results of measurements of the room-temperature effective lifetime for silicon samples subjected to different chemical treatment before (τ^{in}) and after (τ^f) deposition of a rare-earth oxide film. As one can see from Table I, after the rare-earth oxide film is deposited, τ is always higher, the greatest increase occurring for ammonium-peroxide treated samples. Characteristically, annealing an uncoated sample in air at temperature 400 °C for 30 min does not change τ.

The surface recombination rate was determined from measurements of the effective lifetime at 400 K, since, as shown earlier, charge-carrier trapping can be neglected at temperatures $T \geqslant 370$ K. Since the measured effective lifetimes were less than 50 μs and satisfied $1/\tau \gg 1/\tau_0$, the quantity $1/\tau_0$ was neglected in the expression for the surface recombination rate. Table II gives the values obtained for the surface recombination rate in silicon samples before and after deposition of a rare-earth oxide film.

The results presented show that the surface recombination rate decreases when a rare-earth oxide film is deposited. Comparing the recombination characteristics obtained shows that the surface recombination rate in the system Si–rare-earth oxide is one to two orders of magnitude lower than in the structures $Si-SiO_2$ and $Si-SiO_2-Si_3N_4$ widely employed in semiconductor electronics.[5,6]

[1] V. A. Rozhkov and A. I. Petrov, Izv. Vyssh. Uchebn. Zaved. Fiz., No. 7, 99 (1994).
[2] Yu. A. Anoshin, A. I. Petrov, V. A. Rozhkov, and M. B. Shalimova, Zh. Tekh. Fiz. **64**, 118 (1994) [Tech. Phys. **39**, 1039 (1994)].

[3] A. L. Fahrenbruch and R. H. Bube, *Fundamentals of Solar Cells*, Academic Press, N. Y., 1987; Énergoatomizdat, Moscow, 1987, 278 pp.
[4] A. V. Rzhanov, *Electronic Processes in Semiconductors Surfaces* [in Russian], Nauka, Moscow (1971), 480 pp.
[5] V. G. Litovchenko and A. P. Gorban', *Fundamentals of the Physics of Metal–Insulator–Semiconductor Microelectronic Systems* [in Russian], Naukiva Dumka, Kiev (1978), 316 pp.
[6] A. V. Sachenko, B. A. Novominskiĭ, and A. S. Kalshabekov, in *Abstracts of Reports at the 12th All-Union Scientific Conference on Micorelectronics* [in Russian], Tbilisi, 1987, Part 3, p. 143.

Translated by M. E. Alferieff

Edited by David L. Book

Mutual synchronization and desynchronization of Lorenz systems

V. S. Anishchenko, A. N. Sil'chenko, and I. A. Khovanov

N. G. Chernyshevskiĭ Saratov State University

(Submitted September 26, 1997)
Pis'ma Zh. Tekh. Fiz. **24**, 22–30 (April 12, 1998)

The dynamics of two symmetrically coupled Lorenz systems is investigated by means of a numerical experiment. A bifurcation analysis of the synchronization process is presented. The results are compared with numerical experiments. It is shown that changing the coupling can synchronize or desynchronize the subsystems. © *1998 American Institute of Physics.* [S1063-7850(98)00404-2]

Synchronization of systems demonstrating chaotic dynamics has been the subject of numerous investigations and discussions during the last ten years.[1] Several basic approaches to determining the chaotic synchronization have been developed.[2–9] In these treatments, as in most studies of chaotic synchronization, ordinarily the problem of finding functionals that make it possible to perform diagnostics of the cross correlations between subsystems is solved and little attention is given to determining the bifurcation mechanism of the phenomenon. The difficulty of bifurcation analysis of chaotic synchronization is due to the fact that in most cases the mathematical image of chaotic oscillations is a quasiattractor, which includes, together with a nontrivial hyperbolic subset of saddle trajectories, a countable set of stable periodic orbits.[10] On this basis the Lorenz system, for certain values of whose parameters the phase space contains a single attractor, the Lorenz attractor,[11] is the most suitable for analyzing the bifurcation mechanism of chaotic synchronization.

Our objective in the present Letter is to investigate the dynamics of two symmetrically coupled Lorenz systems and to study the bifurcations of saddle cycles and states of equilibrium that give rise to the effects observed accompanying a change in the coupling parameter.

The dynamical system studied here is described by the equations

$$\begin{aligned}\dot{x}_{1,2}&=\sigma(y_{1,2}-x_{1,2})+\gamma(x_{2,1}-x_{1,2}),\\ \dot{y}_{1,2}&=r_{1,2}x_{1,2}-x_{1,2}z_{1,2}-y_{1,2},\\ \dot{z}_{1,2}&=x_{1,2}y_{1,2}-z_{1,2}b.\end{aligned}\tag{1}$$

The values of the parameters ($\sigma=10$, $r_1=28.8$, $r_2=28$, $b=8/3$) are such that a Lorentz attractor exists in each subsystem. The most general approach for studying synchronization of chaotic systems is one based on the concept of an analytical signal and which admits the concepts of instantaneous amplitude and instantaneous phase of the chaotic oscillations.[6,12] The expressions for the instantaneous amplitude and phase of a signal, which were introduced by means of a Hilbert transform, are

$$A(t)=\sqrt{s^2(t)+\tilde{s}^2(t)},\qquad \phi(t)=\tan^{-1}\frac{\tilde{s}(t)}{s(t)},$$

where

$$\tilde{s}(t)=1/\pi\int_{-\infty}^{\infty}\frac{s(\tau)}{t-\tau}d\tau$$

is the Hilbert transform of the initial signal $s(t)$. Figure 1a shows the phase difference, averaged over an ensemble of realizations, as a function of time for different values of the coupling between the subsystems. As one can see from the figure, in the case of zero coupling (curve *1*) the phases of the subsystems are uncorrelated and their difference increases monotonically with time. It is entirely natural to expect that introducing coupling between the subsystems will cause correlations between their phases, whose difference will remain bounded. However, the results of numerical experiments (curves *2* and *3* in Fig. 1) show the opposite: for values of γ from 0 to 2 the phase difference does not decrease, but rather, grows more and more strongly, i.e., phase desynchronization of the subsystems occurs! As the coupling increases further, the phase difference becomes bounded at $\gamma=4.1$ (curve *5* in Fig. 1), thereby giving rise to phase synchronization of the subsystems. The behavior of the average frequencies $\Omega_{1,2}=\langle\dot{\phi}(t)\rangle$, whose dependence on the coupling parameter is shown in Fig. 1b, likewise makes it possible to conclude that phase synchronization of the subsystems is preceded by their desynchronization (the average frequencies diverge for values of γ from 0 to 2). We note that the behavior of the average frequencies Ω_1 and Ω_2, calculated by means of a Hilbert transform, turned out to be completely equivalent to the behavior of the average switching frequency, which we analyzed in a previous work.[13]

One of the characteristics most commonly used for studying chaotic synchronization is the spectrum of Lyapunov exponents. The four largest Lyapunov exponents of the system (1) are presented in Fig. 1c as a function of the coupling. It is evident from the figure that in the case of weak coupling the system possesses three positive Lyapunov exponents λ_1, λ_2, and λ_3 (one of the zero exponents became positive). For $\gamma=1.3$ one exponent becomes negative (in our case λ_3), which in the case of the interaction of Rössler systems is accompanied by phase sychronization of the subsystems.[6] In our case a different situation is observed: Phase synchronization does not occur despite a change in

 © 1998 American Institute of Physics

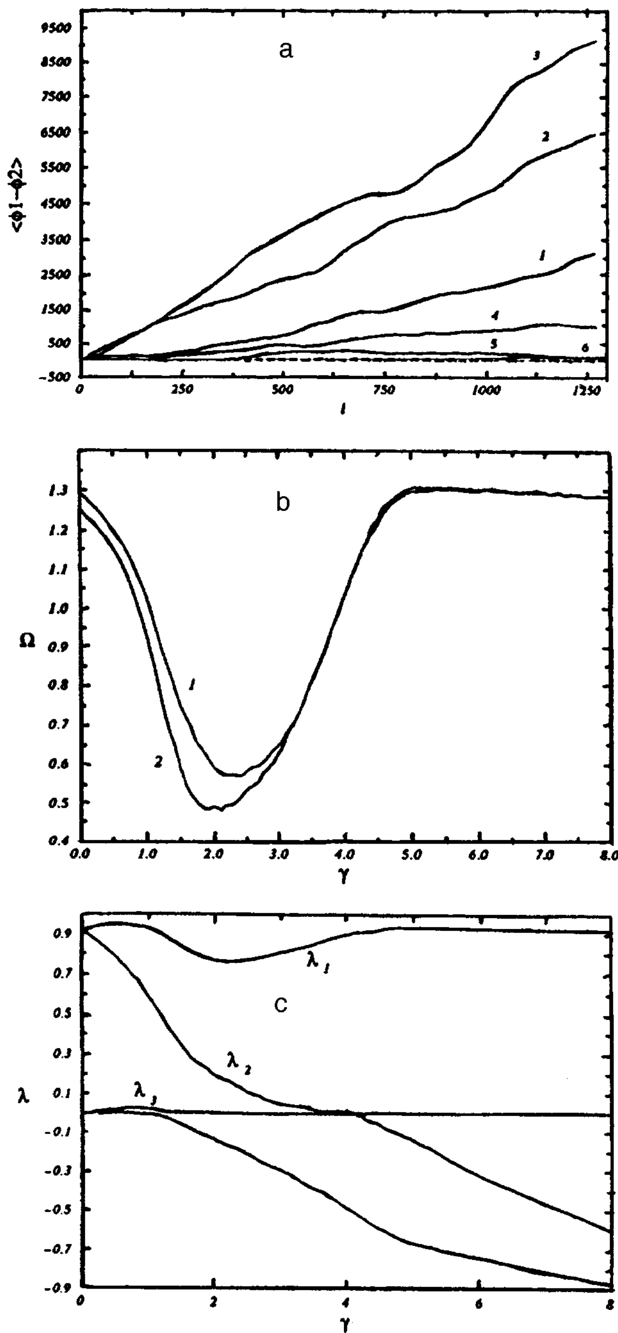

FIG. 1. a — Average phase difference versus time; b — average frequencies: 1 — Ω_1 and 2 — Ω_2 versus the coupling coefficient; c — four largst Lyapunov exponents versus the coupling coefficient.

sign of one exponent. On the contrary, as already mentioned above, phase desynchronization occurs for coupling between 0 and 2. Phase synchronization starts only at $\gamma=4.1$, when the exponent λ_2 becomes negative.

Analysis of bifurcations occurring with increasing coupling parameter showed the following. For relatively weak coupling ($\gamma<0.27$) the structure of the partitioning of the phase space R^6 is determined by families of saddle cycles, coinciding in pairs with the families existing at zero coupling. Increasing the coupling parameter ($\gamma>0.27$) gives rise to a chain of tangent bifurcations, as a result of which there appear two families of saddle cycles C_n^{+1} and C_n^{-1} (the lines $l_{11}^{+1} l_{12}^{+1}$ in Fig. 2a—lines of creation of two pairs of saddle cycles belonging to the indicated families) located near the symmetric ($x_1=x_2$, $y_1=y_2$, $z_1=z_2$) and asymmetric ($x_1=-x_2$, $y_1=-y_2$, $z_1=-z_2$) subspaces, respectively. These families evolve differently with increasing coupling. As one can see from Figs. 2a and 2b, the dimension of the stable manifold of the saddle cycles from the family C_n^{+1} increases from 3 to 4 (in the bifurcation diagram this corresponds to the lines l_{11}, l_{12}, and l_{14}), while the saddle cycles from the family C_n^{-1} become increasingly unstable and vanish as a result of tangent bifurcations (Fig. 2d). The line l_d in Fig. 2a is the line of vanishing of the family C_n^{-1}.

Together with the saddle-cycle bifurcations studied above, bifurcations of states of equilibrium also occur in the system (1). The local properties of the flux near states of equilibrium were investigated by means of the well-known LOCBIF computer program.[14] The investigations showed that when coupling is introduced between the subsystems, the states of equilibrium P_1-P_8 undergo Hopf bifurcations in pairs, as a result of which saddle cycles are created. The states of equilibrium undergo Hopf bifurcation as follows: P_1 and P_5 for $\gamma=0.515$, P_3 and P_7 for $\gamma=0.7944$, P_4 and P_8 for $\gamma=1.191$, and P_2 and P_6 for $\gamma=1.473$. Of the eight saddle cycles created as a result of Hopf bifurcations the cycles C_0^1 and C_0^2 play the most important role (Fig. 2a). Created at $\gamma=0.515$, these saddle cycles have a stable manifold with dimension 2. As the coupling increases, a pair of their complex-conjugate multipliers becomes less than 1 in magnitude at $\gamma=0.7944$, while the dimension of the stable manifold increases to 4. Since the dimension of the stable manifolds of saddle cycles from the family C_n^{+1} for given values of the coupling ($1<\gamma<4$) equals 3, the cycles C_0^1 and C_0^2 become the most strongly attracting saddle cycles in the phase space R^6. For this reason, the probability that a phase trajectory falls within their neighborhood becomes higher than the probability of falling within a neighborhood of a symmetric space. This results in the observed desynchronization of the subsystems. As already mentioned above, phase synchronization occurs in the system (1) for coupling parameter $\gamma\approx4.1$. For this value of the coupling the dimension of the stable manifold of the saddle cycle C_{11}^{+1} increases from 3 to 4, so that it is reasonable to regard the line l_{11} in Fig. 2a as the boundary of the region of phase synchronization. As the coupling parameter increases further, stable manifolds of saddle cycles grow from the family C_n^{+1}, which becomes stable with respect to transverse perturbations for large values of γ and forms an attractor serving as a mathematical image of synchronous chaotic oscillations.

In summary, our investigations of the dynamics of two symmetrically coupled Lorenz systems have shown that desynchronization and synchronization of the subsystems occur as the coupling parameter increases. A detailed bifurcation analysis of the system (1) showed that the observed effects are due to tangential bifurcations of saddle cycles and bifurcations of states of equilibrium occurring with a change in coupling and leading to a restructuring of the partitioning of the phase space R^6 into trajectories. The results obtained in the course of the bifurcation analysis of chaotic synchronization are apparently quite general. The degree of their uni-

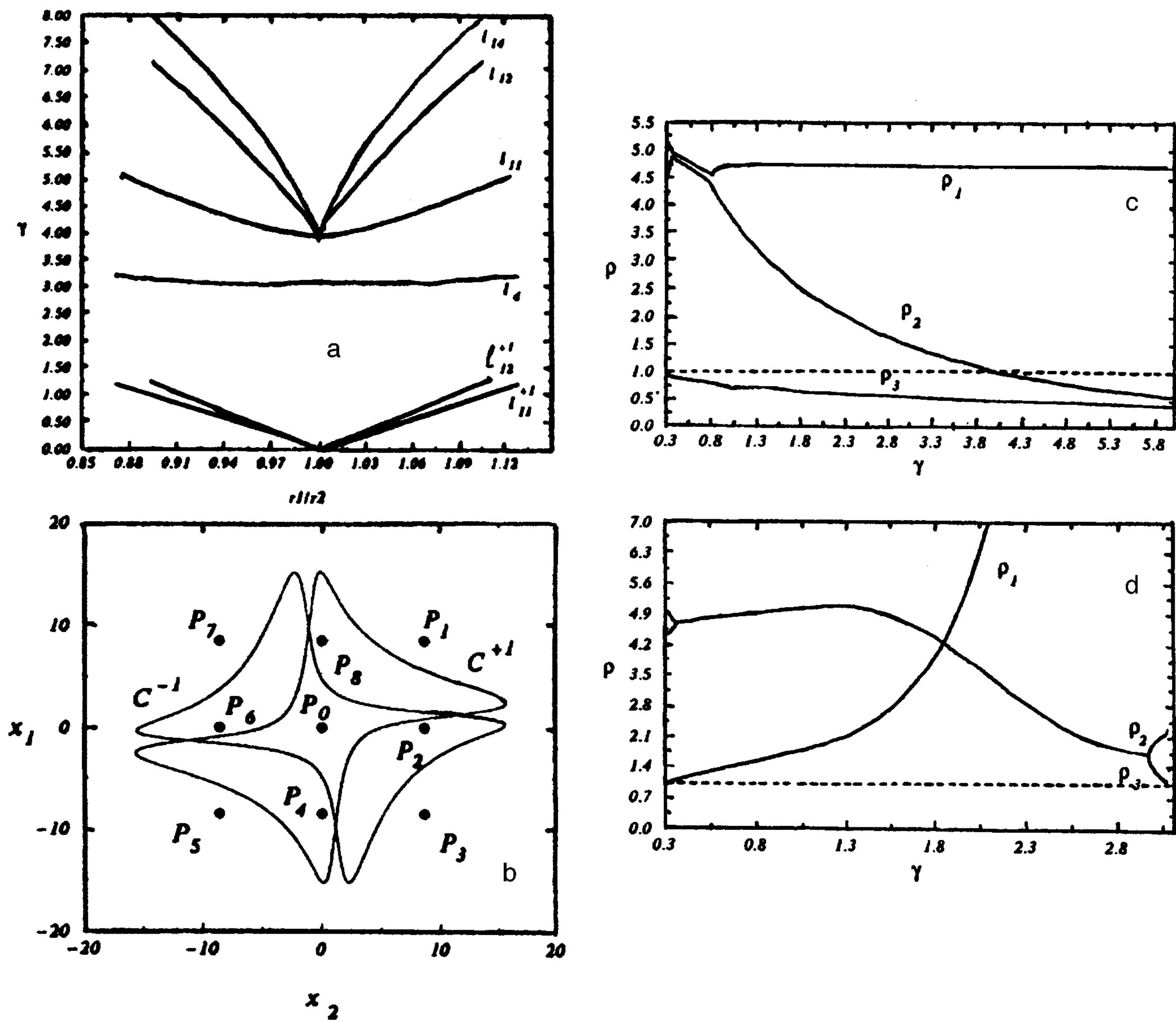

FIG. 2. a — Bifurcation diagram, b — cross phase projection of the saddle cycles C_{11}^{+1} and C_{11}^{-1} created by a tangential bifurcation (P_0-P_8 — states of equilibrium of the system); c — multipliers of the saddle cycle C_{11}^{+1} versus the coupling parameter; d — multipliers of the saddle cycle C_{11}^{-1} versus the coupling parameter.

versality and, specifically, their validity for chaotic systems with attractors of the saddle-focus type are subjects for futher investigations.

This work was financed in part by the Russian Fund for Fundamental Research (Grant 95-0-8.3-66).

[1] I. I. Blekhman, P. S. Landa, and M. G. Rosenblum, Appl. Mech. Rev. **48**, 733 (1995).
[2] V. S. Afraĭmovich, N. N. Verichev, and M. I. Rabinovich, Izv. Vyssh. Uchebn. Zaved. Fiz. **29**, 795 (1986).
[3] L. M. Pecora and T. L. Carroll, Phys. Rev. Lett. **64**, 821 (1990).
[4] V. S. Anishchenko, T. E. Vadivasova, D. E. Postnov, and M. A. Safonova, Chaos **2**, 644 (1992).
[5] V. S. Anishchenco, *Dynamical Chaos—Models and Experiments,* World Scientific, Singapore, 1995, 400 pp.
[6] M. G. Rosenblum, A. S. Pikovsky, and J. Kurths, Phys. Rev. Lett. **76**, 1804 (1996).
[7] V. S. Anishchenko, *Dynamical Chaos in Physical Systems: Experimental Investigation of Self-Oscillating Circuits*, Teubner, Leipzig, 1989; Nauka, Moscow, 1990.
[8] N. N. Verichev, in *Mezhvyz. tematich. sb. nauch. tr.* (Topical Collection of Scientific Works of Schools of Higher Learning), Gor'kiĭ, 1986.
[9] Yu. I. Neĭmark and P. S. Landa, *Stochastic and Chaotic Oscillations*, Kluwer, Dordrecht, 1992; Nauka, Moscow, 1987.
[10] V. S. Afraĭmovich, in *Proceedings of the International Conference on Nonlinear Oscillations* [in Russian], Naukova dumka, Kiev, 1984, Vol. 2, p. 34.
[11] V. V. Bykov and A. L. Shil'nikov, in *Mezhvyz. tematich. sb. nauch. tr.* (Topical Collection of Scientific Works of Schools of Higher Learning), Gor'kiĭ, 1987.
[12] J. S. Bendat and A. G. Piersol, *Random Data: Analysis and Measurement Procedures*, Wiley, N. Y., 2nd edition; Mir, Moscow, 1989.
[13] V. S. Anishchenko, A. N. Sil'chenko, and I. A. Khovanov, Pis'ma Zh. Tekh. Fiz. **23**(8), (1997) [Tech. Phys. Lett. **23**, 300 (1997)].
[14] A. I. Khibnik, Y. A. Kuznetzov, V. V. Levitin, and E. V. Nikolaev, Physica D **62**, 360 (1992).

Translated by M. E. Alferieff
Edited by David L. Book

As_4 incorporation kinetics in GaAs (001) molecular-beam epitaxy

Yu. G. Galitsyn, I. I. Marakhovka, S. P. Moshchenko, and V. G. Mansurov

Institute of Semiconductor Physics, Siberian Branch of the Russian Academy of Sciences, Novosibirsk
(Submitted November 18, 1997)
Pis'ma Zh. Tekh. Fiz. **24**, 31–38 (April 12, 1998)

A kinetic model of epitaxial growth on a Ga-stabilized GaAs (001) surface from As_4 and Ga beams is proposed. Elementary surface processes are studied: adsorption–desorption of As_4, bimolecular reaction of As_4^*, and incorporation of As_2^{chem} in lattice sites. The model correctly describes the experimental results for the growth rate at low and high As_4 pressures. The role of As_4 desorption from the surface in the epitaxial growth of GaAs crystals is analyzed.
© *1998 American Institute of Physics.* [S1063-7850(98)00504-7]

The (001) GaAs system of homoepitaxial growth from As_4 and Ga beams has been studied the most and can serve as a model system for studying the elementary processes of molcular-beam epitaxy (MBE).[1–7] Even for this system, however, there are substantial discrepancies in the interpretation of the kinetics and mechanisms of growth.

In the first place, in Refs. 1 and 5–7 the dissociative chemisorption of As_4 is considered to be bimolecular, whereas in Ref. 2 some growth results were interpreted on the basis of monomolecular dissociation of As_4.

In the second place, an investigation of the temperature dependence of the incorporation ratio (S) of the arsenic tetramer at relatively high pressures ($P \geqslant 3\times10^{-6}$ Torr) revealed a very weak variation of S with temperature.[1,2] As an example, Ref. 1 gives $S \simeq 0.415$ at $T \simeq 570$ °C, but $S \simeq 0.495$ at $T \simeq 360$ °C. The total change in S is $\sim 20\%$. However, the growth investigations performed in Refs. 6–8 at pressures $P \leqslant 10^{-6}$ Torr in the temperature range 500 -600 °C showed that the incorporation ratio varies by a considerable factor. Such large temperature variations of the growth rate (or S) at relatively low pressures do not occur in the kinetic growth model proposed in Ref. 1.

In the present Letter we propose a kinetic model of GaAs (001) growth from As_4 and Ga beams that takes account of the regions of both high and low arsenic pressures (As_4).

The kinetics of arsenic incorporation in growth is ordinarily studied according to intensity oscillations of the mirror reflection in HEED which are induced by the incident As_4 flux on a Ga-stabilized surface with an uncontrollable quantity of Ga on the surface.[1,3,8] We employed an alternative method of delivering Ga and As_4 to the surface with a precisely fixed Ga concentration on the surface and we measured by the HEED method the conversion time t of gallium into a two-dimensional epitaxial layer of GaAs for some sample temperatures T and arsenic (As_4) pressures P.[6,7]

The P and T dependences of the conversion time t of a gallium monolayer (or the quantity $V=1/t$) were analyzed by means of the following kinetic scheme:

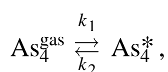

$$As_4^{gas} \underset{k_2}{\overset{k_1}{\rightleftarrows}} As_4^*,$$

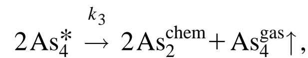

$$2As_4^* \xrightarrow{k_3} 2As_2^{chem} + As_4^{gas}\uparrow,$$

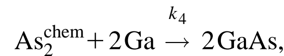

$$As_2^{chem} + 2Ga \xrightarrow{k_4} 2GaAs,$$

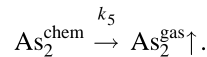

$$As_2^{chem} \xrightarrow{k_5} As_2^{gas}\uparrow.$$

Here k_i are the elementary rate constants of simple reactions.

The Arrhenius approximation can be used for the rate constants $k_i = k_i^0 \exp(-E_i/kT)$. The constants k_1 and k_2 are the rate constants of the adsorption–desorption process of the interaction of the surface with gas molecules (As_4^{gas}) and molecules (As_4^*) adsorbed in a "precursor state." The constant k_3 is the rate constant of the bimolecular interaction reaction of As_4, leading to dissociation of As_4^* molecules and the formation of two chemisorbed molecules As_2^{chem}, with simultaneous desorption of one molecule As_4^{gas} into the vacuum. This process of dissociative chemical adsorption of As_4^* was first proposed by Foxon and Joyce.[9] This bimolecular reaction on the surface is analogous to the Langmuir–Hinshelwood reaction and, as we shall show below, describes the experimental results on growth better than does the monomolecular dissociation of As_4^*, proposed in Ref. 2. Moreover, this process determines the maximum As_4 incorporation ratio $S=0.5$.[9] The reaction with the rate constant k_4 is a process of incorporation of As_2^{chem} in lattice sites, i.e., $1/t = V = k_4[As_2^{chem}]$ is the epitaxial growth rate or the formation rate of the new phase GaAs. In Refs. 6 and 7 it was shown that the incorporation reaction is zeroth order in the gallium concentration. Desorption of As_2^{chem} is described by the reaction with the rate constant k_5. For GaAs this reaction is important at temperatures above 600 °C. Figure 1 shows schematically the elementary stages of growth on a Ga-stabilized surface (4×2). From this diagram we find the following expression for the rate V under conditions such that the intermediate products As_4^* and As_2^{chem} are stationary:

$$V = \frac{k_4}{k_4+k_5}\, k_3 \left(\frac{k_2+k_1P}{2k_3}\right)^2 (\sqrt{1+x}-1)^2, \tag{1}$$

where $x = k_1P/k_3((k_2+k_1P)/2k_3)^{-2}$. All the constants k_i and k_1P and the surface concentrations of the intermediate

 © 1998 American Institute of Physics

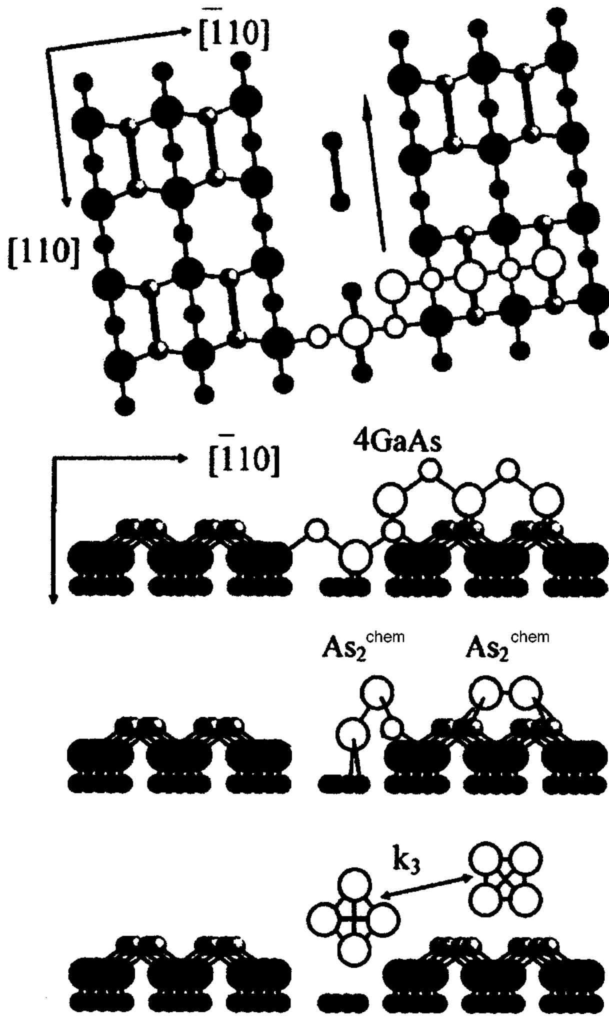

FIG. 1. Schematic of the elementary stages of epitaxial growth on a Ga-stabilized surface (4×2). Large and small black spheres — surface arsenic and gallium atoms, respectively. White spheres — atoms of the new phase GaAs. Gallium atoms which are not bound with arsenic are not indicated in the scheme. The arrow marks the possible direction of growth of the 4GaAs critical nucleus.

particles are normalized so that the dimension of the epitaxial growth rate V is expressed in monolayers per second.

The parameter x has a simple physical meaning. It is the ratio of two stationary concentrations C_1 and C_2, i.e., $x=4C_1/C_2$. The quantity $C_1=k_1P/(k_2+k_1P)$ is the stationary concentration of As_4^* for the conventional adsorption–desorption process of interaction of As_4 molecules with a surface, neglecting bimolecular dissociative chemisorption of As_4. The quantity $C_2=(k_2+k_1P)/k_3$ is the stationary concentration of As_4^* for which the monomolecular desorption flux k_2C_2 equals the bimolecular reaction flux $k_3C_2^2$ $(k_2C_2=k_3C_2^2)$.

Since we are analyzing the growth on a Ga-stabilized GaAs surface, both normalized As_4^* concentrations are much less than unity $(C_1, C_2\ll1)$. For $k_1P\ll k_2$ we have

$$V=A(T)k_3\left(\frac{k_2}{2k_3}\right)^2(\sqrt{1+4C_1/C_2}-1)^2, \tag{2}$$

where $A(T)=k_4/(k_4+k_5)$. Estimates show that for $P\sim10^{-7}-10^{-6}$ Torr and $T\sim600-570$ °C the concentration

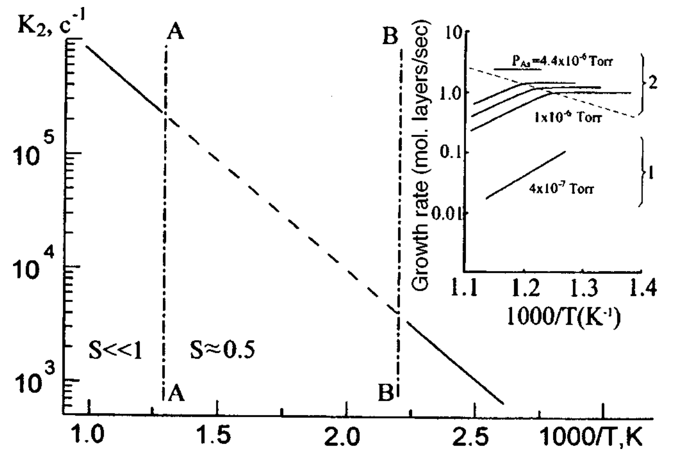

FIG. 2. Temperature dependence of the desorption constant $k_2(T)$. The dashed lines determine the region of intense epitaxial growth $S\simeq0.5$. The line A–A is drawn for $P\simeq10^{-6}$ Torr. An increase or decrease of As_4 pressure displaces the A–A line into the high- or low-temperature region, respectively. The line B–B is drawn according to the data of Ref. 9 Inset: Arrhenius plots of the growth rate at different As_4 pressures. 1 — experimental data of this work, 2 — experimental data of Ref. 8.

C_1 lies in the range $10^{-7}-10^{-6}$ monolayers, while C_2 lies in the range $10^{-6}-10^{-5}$ monolayers. Therefore it is entirely possible to realize growth conditions such that $x\ll1$. Then we have for the epitaxy rate

$$V\simeq A(T)k_3\left(\frac{k_1P}{k_2}\right)^2=B(T)P^n=V_0\exp(E_{\rm eff}/kT) \tag{3}$$

with effective activation energy $E_{\rm eff}=2E_2-E_3-2E_1$. Such an exponential dependence of the growth rate on the reciprocal of the temperature at quite low As_4 pressures has been observed experimentally in Refs. 6 and 7 and in Ref. 8 (see inset in Fig. 2). The growth rate as a function of As_4^* pressure was found to have the power-law exponent $n\simeq1.5$ in Refs. 6 and 7 and $n\simeq1.4$ in Ref. 8.

The condition $4k_3/k_1P\gg1$ is always satisfied for the As_4 pressures ordinarily employed, so for the other limiting case $k_1P\gg k_2$ we have

$$V=\frac{k_4}{k_4+k_5}k_1P=A(T)k_1P. \tag{4}$$

Such a linear dependence of the growth rate on P has been observed experimentally in our investigations as well as in Refs. 1 and 8 for relatively high pressures $P>2\times10^{-6}$ Torr and relatively low temperatures $T<570$ °C. In these temperature and pressure ranges intense growth of a new phase GaAs occurs $(S\simeq0.5)$. Then the problem arising in this analysis of epitaxial growth on a Ga-stabilized (001) GaAs surface is whether the condition $k_1P\gg k_2(T)$ can actually be realized. The constant $k_2=k_2^0e^{-E_2/kT}$ has been determined well for low temperatures $T\leqslant150$ °C, $k_2^0\simeq0.625\times10^8$ 1/s and $E_2\simeq0.4$ eV.[9] In the temperature range from 150 to 600 °C it varies from 2.4×10^3 1/s up to 3×10^5 1/s (Fig. 2). Thus, even if the As_4 pressure is increased to 10^{-5} Torr it is impossible to satisfy the condition $k_1P\gg k_2$. For $P\sim10^{-5}$ Torr $k_1P\sim10^2$ 1/s, while $k_2\gg10^2$ 1/s in the temperature from 150 °C and above.

Is it possible that extrapolation of $k_2(T)$ from low to high temperatures is invalid? In Ref. 8 the desorption flux of As_4^* at pressures $P \simeq 10^{-6}$ Torr was determined for the temperature range $T > 580$ °C. Extrapolation of the temperature dependence $k_2(T)$ into this high-temperature region leads to the correct value of the measured desorption flux. This flux at $T \simeq 635$ °C equals approximately one monolayer per second ($J_{des} = k_2(T)C \simeq 10^6 \times 10^{-6} \simeq 1$ monolayer per second). Therefore there are no grounds for believing that the desorption rate constant $k_2(T)$ changes sharply at intermediate temperatures, where intense epitaxial growth occurs and the expression (4) is correct (Fig. 2). The question arises as to why the desorption flux is suppressed in a given temperature range. Moreover, at a fixed pressure P the transition from the exponential dependence of the rate (3) to the virtually temperature-independent rate (4) occurs in a very narrow temperature interval ΔT, for example, $\Delta T \sim 3-5$ °C near $T = 543$ °C.[8] We believe that the transition to intense epitaxial growth (where $S \simeq 0.5$) is associated with a sharp change in the ratio of the desorption ($k_2 C$) and reaction ($k_3 C^2$) fluxes.

When the growth temperature is decreased at fixed arsenic pressure or the pressure is increased at fixed temperature, the standard thermodynamic barrier against growth of a new phase GaAs is overcome. Critical supersaturation with respect to As_4^* is eliminated by rapid formation of two-dimensional nucleation centers (2D nucleation). A large number of critical nuclei (''4GaAs'') develop, whose further growth sharply decreases the As_4^* concentration at the surface to a new stationary value C^*, for which $k_2 C^* \ll k_3'(C^*)^2$ (and also $k_2 C^* \ll k_1 P$). With an overwhelming probability As_4^* will participate in the reaction $k_3'(C^*)^2$ before desorbing from the surface. Estimates show that even for $C^* \sim 10^{-7}$ and $k_3' \sim 10^{13}$ 1/s the reaction lifetime of As_4^* ($1/k_3' C^* \sim 10^{-6}$ 1/s) is short compared with the desorption time of As_4^* ($1/k_2 \sim 10^{-5}$ 1/s). In order for the surface morphology to change in the 2D-nucleation regime the constant k_3 must change to k_3' such that $k_3' \gg k_3$.

The decrease of the As_4^* concentration to C^* in the 2D-nucleation regime is analogous to a rapid decrease in the concentration of Ga adatoms in MBE on an As-stabilized surface (2×4) when 2D GaAs nuclei form on this surface.[10]

We shall now make a number of remarks concerning Ref. 1. In the first place, the weak temperature dependence of the growth rate in that study was attributed there to the term $A(T)$ in the expression (4). However, as follows from our analysis, in order not to ''entrain'' the sharp temperature dependence of the growth rate given by the expressions (2) and (3) and to guarantee applicability of Eq. (4), the critical point of the transition to Eq. (4) must be determined at a fixed As_4 pressure. Tok *et al.*[1] did not perform such investigations. In the second place, they employed a function which is unacceptable for analyzing the incorporation ratio S: $2S/1-2S$. For $S \simeq 0.5$ this function can be arbitrarily large, and hence it magnifies sharply the experimental errors made in the measurements of S.

This work was supported by the Russian Fund for Fundamental Research (Grants Nos. 96-03-33916a and 95-02-04618a).

[1] E. S. Tok, J. H. Neave, J. Zhang, B. A. Joyce, and T. S. Jones, Surf. Sci. **374**, 397 (1997).
[2] S. Yu. Karpov and M. A. Maiorov, Surf. Sci. **344**, 434 (1995).
[3] E. S. Tok, J. H. Neave, J. Zhang, F. E. Allegretti, B. A. Joyce, and T. S. Jones, Surf. Sci. **371**, 277 (1997).
[4] S. Yu. Karpov and M. A. Maĭorov, Pis'ma Zh. Tekh. Fiz. **23**(1), 64 (1997) [Tech. Phys. Lett. **23**, 38 (1997)].
[5] A. K. Ott, S. M. Casey, A. L. Alstrin, and S. R. Leone, J. Vac. Sci. Technol. **14**, 2742 (1996).
[6] Yu. G. Galitsyn, V. G. Mansurov, and I. I. Marahovka, Phys. Low-Dimens. Semicond. Struct. **5/6**, 75 (1997).
[7] Yu. G. Galitsyn, V. G. Mansurov, and I. I. Marahovka, Phys. Low-Dimens. Semicond. Struct. **7**, 55 (1997).
[8] J. C. Garcia, C. Neri, and J. Massies, J. Cryst. Growth **98**, 511 (1989).
[9] C. T. Foxon and B. A. Joyce, Surf. Sci. **50**, 434 (1975).
[10] A. K. Myers-Beaghton and D. D. Vvedensky, Phys. Rev. B **42**, 5544 (1990).

Translated by M. E. Alferieff
Edited by David L. Book

Reconstruction of the x-ray emission spectrum of a nanosecond creeping discharge

P. N. Dashuk, S. L. Kulakov, and E. K. Chistov

St. Petersburg State Technical University
(Submitted December 22, 1997)
Pis'ma Zh. Tekh. Fiz. **24**, 39–44 (April 12, 1998)

A method is proposed for determining the soft x-ray emission spectrum of a nanosecond creeping discharge. The method includes a determination of the photoelectron density from photocurrent measurements and a calculation of the spectral flux density. The results are compared with experimental data on the wavelength interval of maximum radiation intensity.
© *1998 American Institute of Physics.* [S1063-7850(98)00604-1]

It is well known that a nanosecond creeping discharge is an efficient source of soft x radiation (SXR) which has applications in different fields of science and technology, for example, in the preionization systems of high-power pulsed gas lasers, in the manufacture of submicron-size devices for microelectronics, and in medicine and biology. The efficient use of SXR in all these cases requires a detailed knowledge of the spectral composition of the radiation.

In the present Letter we propose a method for calculating the x-ray emission spectrum of a nanosecond creeping discharge from the experimentally obtained dependence of the photoelectron density on the distance to the radiation source. This method includes reconstruction of the rate of charged-particle production and the total photoelectron density from photocurrent measurements.

The experimental apparatus for measuring the photocurrent consisted of a high-voltage pulse generator built around a strip forming line, impulsive charging circuits, a discharge ignition unit, a system for forming a creeping discharge (the SXR emitter), and a chamber and a sensor for recording the photoelectron density. The profile of the surface of formation of the creeping discharge, the thickness of the dielectric, and the interelectrode spacing were chosen according to the recommendations of Ref. 1. The rate of increase of the voltage powering the discharge was on the order of 10^{14} V/s, the rise time of the voltage pulse was 1–3 ns, and the amplitude of the voltage pulse was 200–400 kV. The photoelectron sensor consisted of a chamber where a uniform electric field was formed between the entrance window grid and the flat detecting electrode. A 4 mm interelectrode gap provided, for a fixed voltage of the sensor equal to 1.6 kV, an electric field sufficient for recording a photocurrent of 0.1–1 Å. The low-inductance construction of the sensor made it possible to record the change in the photoelectron density with a temporal resolution of less than 10 ns.

The energy distribution $Y(\lambda,t)$ in the continuous spectrum of the x radiation is related to the ionization rate $q(x,t)$, where x is the distance measured from the ionizer and t is the time, by the relation[2]

$$q(x,t)=\exp(-bd)\int_{\lambda_{\min}}^{\lambda_{\max}}(Y(\lambda,t)\times\exp(-\mu(\lambda)x)\gamma(\lambda))/\varepsilon d\lambda. \quad (1)$$

Here $\mu(\lambda)$ is the linear attenuation coefficient, $\gamma(\lambda)$ is the electronic conversion factor, and ε is the average ionization energy. The quantity e^{-bd} accounts for the attentuation of radiation in the entrance window of the measuring chamber; d is the thickness of the window. We introduce the spectral flux density

$$B(\lambda)=\int_0^{\tau_p}Y(\lambda,t)dt$$

(τ_p is the SXR generation time in the discharge) and integrate the expression (1) over t. We obtain the integral equation

$$n(x)=\exp(-bd)\int_{\lambda_{\min}}^{\lambda_{\max}}(B(\lambda)\exp(-\mu(\lambda)x)\gamma(\lambda))/\varepsilon d\lambda \quad (2)$$

for determining the spectral flux density from the experimental dependence of the photoelectron density $n(x)$. Equation (2) is a Fredholm equation of the first kind. The problem of solving this equation is ill-posed. It can be solved by the variational method of regularization.[3] In this method the solution of Eq. (2) is equivalent to the problem of finding the functional $K(x,\lambda)=\exp(-bd-\mu(\lambda)x)\gamma(\lambda)/\varepsilon$ that minimizes

$$J=\int_{x_{\min}}^{x_{\max}}\left(\int_{\lambda_{\min}}^{\lambda_{\max}}K(x,\lambda)B(\lambda)d\lambda-n(x)\right)^2dx,$$

where $x_{\min}$ and $x_{\max}$ are the minimum and maximum distances from the ionizer to the sensor. In Ref. 3 it is shown that the problem of minimizing the functional

$$J_1=\int_{x_{\min}}^{x_{\max}}\left(\int_{\lambda_{\min}}^{\lambda_{\max}}K(x,\lambda)B(\lambda)d\lambda-n(x)\right)^2dx + \alpha\int_{\lambda_{\min}}^{\lambda_{\max}}B^2(\lambda)+(dB/d\lambda)^2)d\lambda$$

is properly posed and its solution approximates the minimum of the initial functional J. The number α is called the regularization parameter.

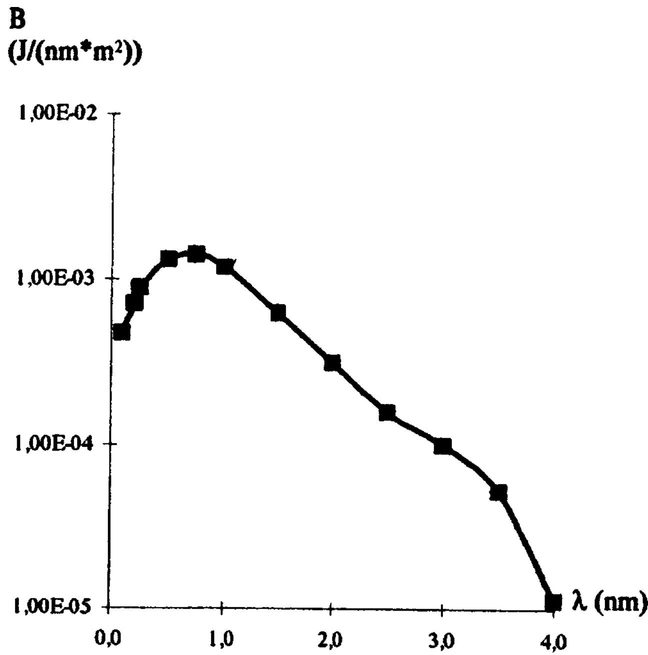

FIG. 1. SXR spectral flux density versus wavelength.

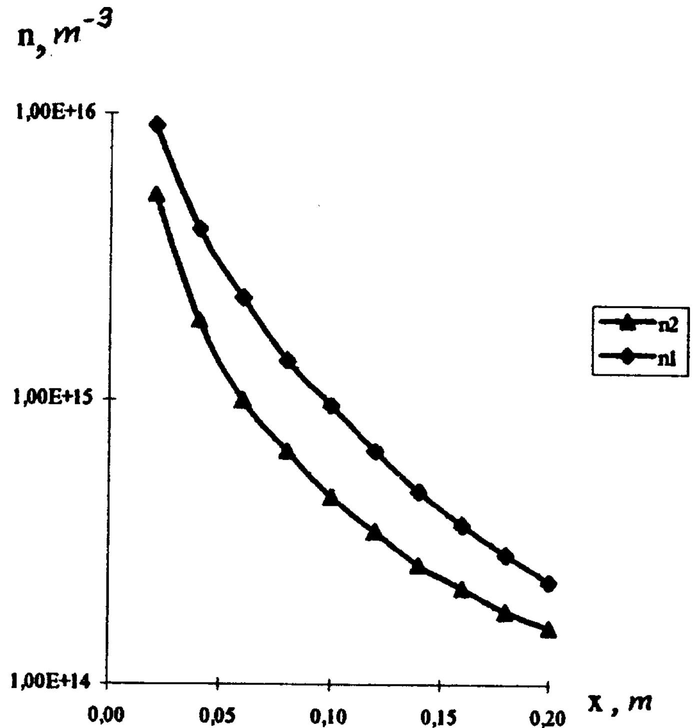

FIG. 2. Photoelectron density versus distance to ionizer: 1 — Experimental curve; 2 — Curve obtained by the inverse calculation.

We introduce on the rectangle $\lambda_{\min}<\lambda<\lambda_{\max}$, $x_{\min}<x<x_{\max}$ the grid $\{x_i, \lambda_j, i=1,\dots,N; j=0, \dots,M+1\}$, where $x_1=x_{\min}$, $x_N=x_{\max}$, $\lambda_0=\lambda_{\min}$, $\lambda_{M+1}=\lambda_{\max}$. We choose $\lambda_{\min}$ and $\lambda_{\max}$ so that the boundary conditions $B(\lambda_{\min})=B(\lambda_{\max})=0$ are satisfied with sufficient accuracy. We shall now construct a difference scheme for the problem. We approximate the integrals appearing in the functional J_1 using the trapezoidal rule, replacing at the same time the derivatives with a difference expression, and we obtain a finite-dimensional approximation of the functional J_1. To solve the finite-dimensional problem of finding the minimum of the functional, we equate to zero the derivatives with respect to B_i, where $B_i=B(\lambda_i)$, $i=1,\dots,M$. We obtain a system of linear algebraic equations for B_i:

$$\alpha B_i-\alpha\Lambda(B_i)+h_\lambda\sum_{j=1}^{M} Q_{ij}B_j=\Phi_i, \quad i=1,\dots,M, \tag{3}$$

where $h_x=x_{i+1}-x_i$, $h_\lambda=\lambda_{i+1}-\lambda_i$, $\Lambda(B_i)=(B_{i-1}-2B_i+B_{i+1})/h_\lambda^2$, $2\leqslant i\leqslant M-1$; $\Lambda(B_1)=(2B_1-B_2)$, $\Lambda(B_M)=(2B_M-B_{M-1})$; $Q_{ij}=h_x\Sigma b_n k_{ni}k_{nj}$, $\Phi_i=h_x\Sigma b_n K_{ni}n_n$, $K_{nm}=K(x_n,\lambda_m)$, $n_n=n(x_n)$, $b_n=1/2$ for $n=1$ and N and $b_n=1$ for $2\leqslant n\leqslant N-1$.

The system (3) was solved by a direct method. In the course of the calculations the regularization parameter α was varied in the range $0.5\times10^6-0.5\times10^{12}$. From the various $B(\lambda)$ obtained for different values of α we chose that which had no sharp oscillations and did not pass through zero and had the smallest error in the quadratic deviation of $n(x)$. Figure 1 displays the results of the reconstruction of the x-ray emission spectrum of the creeping-discharge ionizer from the dependence of the photoelectron density on the distance to the ionizer presented in Fig. 2 (nitrogen, pressure 55 kN/m^2, voltage pulse amplitude 300 kV, rise time 1.5 ns). Figure 2 also shows the results of the inverse calculation of $n(x)$ from the spectral flux density.

The experimental data, obtained by different methods, on the wavelength interval of maximum intensity ($\Delta\lambda_{\max}$) agree well with the calculations. The method of differential gas filters gave $\Delta\lambda_{\max}\simeq0.4-1$ nm, while the method of attenuation in beryllium foils gave $\Delta\lambda_{\max}\simeq0.35-0.9$ nm. It should be especially underscored that this method, in contrast to the experimental methods presented above, makes it possible to calculate the absolute value of the spectral flux density.

This work was performed as part of Project No. 97-02-18225 financed by the Russian Fund for Fundamental Research.

[1] P. N. Dashuk, S. L. Kulakov, and Yu. V. Rubin, Pis'ma Zh. Tekh. Fiz. **11**, 438 (1985) [Sov. Tech. Phys. Lett. **11**, 182 (1985)].
[2] K. K. Aglintsev, *Dosimetry of Ionizing Radiations* [in Russian], State Publishers of Technical and Theoretical Literature, Moscow, 1967, p. 503.
[3] N. N. Kalitkin, *Numerical Methods* [in Russian], Nauka, Moscow, 1978, p. 512.

Translated by M. E. Alferieff
Edited by David L. Book

Model of high-T_c superconductivity in low-coordination semiconductors and polymers

B. P. Popov and K. D. Tsе́ndin

St. Petersburg State Technical University, A. F. Ioffe Physicotechnical Institute, Russian Academy of Sciences, St. Petersburg

(Submitted December 23, 1997)
Pis'ma Zh. Tekh. Fiz. **24**, 45–50 (April 12, 1998)

We propose a model in which the state with anomalously high conductivity observed in some low-coordinated semiconductors and polymers when the temperature of the surrounding medium is $T_0 \approx 300$ K, is described by the theory of the superconducting properties of a system of localized electron pairs. The superconducting properties of the model are determined by transport along a bipolaron band formed by localized pairs of carriers belonging to U^- centers, i.e., intrinsic defects with a negative effective correlation energy. © *1998 American Institute of Physics.*
[S1063-7850(98)00704-6]

The nature of the highly conducting channels formed in films of low-coordination semiconductors[1] and polymers[2] is currently being widely discussed. In micron-thick (L) films of chalcogenide glassy semiconductors (CGSs) the high-conductivity channels are produced by a strong electric field ($\sim 10^5$ V/cm). The channel temperature was taken to be $T = 300-360$ K in Ref. 3 and $T \approx 500$ K in Ref. 4. The main voltage drop and hence the main resistance are concentrated in a narrow $\sim 0.1L$ long region near the contacts. The voltage on the remaining $0.9L$ length of the channel and correspondingly its conductivity are, strictly speaking, unknown. In what follows we shall be concerned with only the properties of this part of the channel. A large number of works devoted to the explanation of the high-conductivity state are analyzed in Refs. 1 and 5, whence it follows that none of the explanations is final and universally accepted. This fact together with the possibility of assigning to the main part of the channel an arbitrarily high conductivity suggest the following hypothesis.

The main type of intrinsic defects in CGSs are centers on which there exists, on account of the interaction of the electrons with the lattice, an effective attraction between the electrons so that electron pairs are localized on them. The density of these so-called U^- centers is $10^{17}-10^{19}$ cm^{-3}. At the same time the superconducting properties of a system of U^- centers were studied theoretically back at the beginning of the 1980s.[6,7] We shall describe a U^- center for glassy Se, the simplest CGS. In Fig. 1 the dashed circle on the left in Fig. 1 encloses the main structural unit C_2^0 (the super- and subscripts denote the charge state and the coordination number, respectively) together with the electrons belonging to it. The two black dots represent two lone-pair electrons (p-type LP electrons) that do not participate in bonds with nearest neighbors. The dashed circle at the center encloses a C_3^+ defect which is formed by single ionization of a C_3^0 neutral defect. According to Ref. 8, C_3^0 has the lowest formation energy E among all neutral defects. The value of E is even lower in charged defects in CGSs, i.e., the reaction

$$2C_3^0 \rightarrow C_3^+ + C_1^- \quad (1)$$

is exothermal. The dashed circle on the right-hand side in Fig. 1 the right-hand dashed circle distinguishes the defect C_1^- and it is shown schematically how this defect forms from the defect C_3^0 by breaking of the bond indicated by the dashed line. The density N of charged defects is high on account of the low coordination and lack of participation of LP (p) electrons in the formation of a chemical bond with nearest neighbors in the main network of the CGS. This is why the LP (p) electrons can enter into a chemical bond accompanying the appearance of defects and thereby produce defects with a low value of E. Taking $N = N_0 \times \exp(-E/kT)$, we obtain $E = 0.25$ eV for $N_0 = 10^{22}$ cm^{-3}, $N = 10^{18}$ cm^{-3}, and $T = 300$ K.

Statistically speaking, the reaction (1) signifies that the charged defects each spend the same amount of time in one or the other charged state, exchanging charges with neighbors in the process. As the temperature decreases, the state with simultaneous synchronous charge transfer on a macroscopic number of defects can become the ground state of the system of U^- centers, i.e., a coherent state appears.

We write the Hubbard Hamiltonian for this model as

$$\mathrm{H} = -U \sum_i n_i \uparrow n_i \downarrow + \sum_{ij\sigma} t_{ij} a_{i\sigma}^+ a_{j\sigma}, \quad (2)$$

where $n_{i\sigma} = a_{i\sigma}^+ a_{i\sigma}$ are the occupation numbers and $a_{i\sigma}^+$ and $a_{i\sigma}$ are operators creating and annihilating electrons with spin σ on defect i. We shall assume, as was done in Refs. 6 and 7, that the charged defects form a cubic lattice and all transfer integrals equal t. The specific nature of the model is reflected in the magnitude and sign of the coefficient $-U$. The minus sign corresponds to attraction of electrons at a defect i. The BCS description of superconductivity corresponds to $t \gg U$, when a wide band of single-electron states exists, while pairing of electrons concerns only electrons whose energy is close to the Fermi energy E_f. A gap and a pair appear simultaneously, while the superconducting current is transported only by a small number of electrons with energy $\sim E_f$.

 © 1998 American Institute of Physics

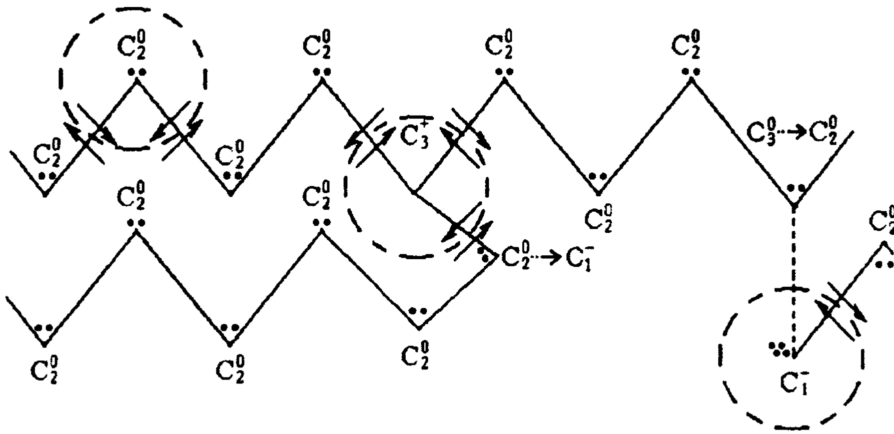

FIG. 1. Schematic diagram of the structure of glassy Se. See text for explanation.

The reverse relation $t \ll U$ describes the localized-pair model.[6,7] For $t=0$ all pairs are localized on the defects C_1^- and C_3^+. In the single-electron band diagram (Fig. 2) these states can be represented by the thermal ionization ε_1 of the defect C_1^-, which then transforms into the defect C_3^0, and the thermal ionization energy ε_2 required for the latter defect to transform into the state C_3^+. In this case $\varepsilon_2 - \varepsilon_1 = -U < 0$. The finiteness of the transport integral t makes possible the appearance of a bipolaron band of width $W = 2zt^2/U$, where $z=6$ is the number of defects (closest to the given defect) along which a bipolaron can move. According to Refs. 6 and 7, the superconducting state arises at temperature

$$T_c = W(1-2\nu)/\ln(\nu^{-1}-1), \quad (3)$$

where ν is the ratio of the number of bipolarons to the total number N of locations along which the bipolarons can move. The gap appearing in the spectrum at $T < T_c$ equals $\Delta = W|\alpha|^2$, where $|\alpha|$ the absolute value of the order parameter.

One can see that the transition temperature and gap in the localized-pair model are of the same order of magnitude as the band width W itself. This is because localized pairs also exist for $W=0$, while the correlation in their motion arises as a result of interdefect transitions. In contrast to the BCS theory, all electrons participate in superconducting transport. The experimental data presented above were obtained on CGSs with band gap $E_g \approx 1$ eV. Ordinarily, $U \sim E_g/2$, so that we shall take $U=0.5$ eV. For estimation purposes we shall write the transfer integral in the form $t = t_0 \exp(-2r/a)$, where r is the distance between defects and a is the radius of the wave function. According to Ref. 9, for estimates it can be assumed that $t_0 \approx 5$ eV. We shall set $\nu \sim 1/4$. This means that acceptors that compensate U^- centers are present in the material and therefore $\nu < 1/2$. At $T = 500$ K the number of defects increases to $\sim 5 \times 10^{19}$ cm^{-3}, whence $r = 25$ Å. According to Refs. 8 and 10, electronic states on C_3^+ and C_1^- are similar to shallow donor and acceptor states, so that the radius a can be taken to be ~ 10 Å. Substituting these values into Eq. (3), we obtain $T_c = 500$ K. Therefore we have obtained that the presence of defects with density $5 \cdot 10^{19}$ cm^{-3} in a system of U^- centers can explain high-T_c superconductivity with a transition temperature above room temperature.

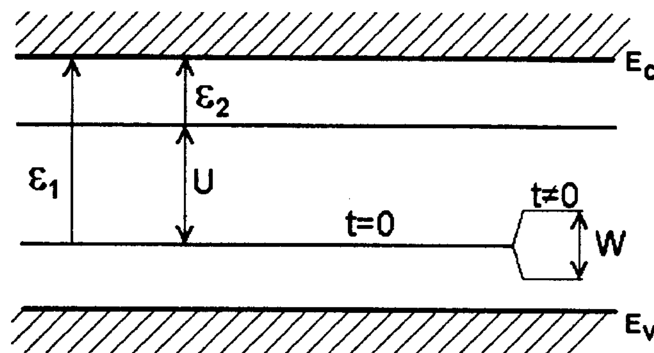

FIG. 2. Energy diagram of a system of U^- centers. ε_1 and ε_2 — first and second thermal ionization energies of an isolated center ($t=0$). W — width of the bipolaron band arising with a finite value of the transfer integral $-t$.

Conducting channels in polymer films ($L \sim 10$ μm) arise under the combined effect of a voltage $V \leqslant 10^3$ V and uniaxial pressure. Experiments in which electrodes are transferred into a superconducting state are especially impressive; the resistance of the channel was no greater than instrumental error, while the estimate of the conductivity of the channel exceeded that of the best metals.[11,12] An anomalously high conductivity has been observed in oxide films. Oxygen occupies the same group of the periodic chart as Se and, just as Se, in an overwhelming number of cases its valence is 2, leaving two of its LP (p) electrons not engaged in bonds with nearest neighbors. This circumstance together with the low-coordination nature of the polymers (their lability) suggest that, just as in CGSs, a quite high density of U^- centers can appear in oxidized polymers.

We thank A. M. El'yashevich, V. A. Zakrevskiĭ, A. N. Ionov, and V. F. Masterov for helpful discussions and the Russian Fund for Fundamental Research for support (Grant No. 97-02-18079).

[1] É. A. Lebedev and K. D. Tséndin, in *Electronic Phenomena in Chalcogenide Glassy Semiconductors* [in Russian], edited by L. D. Tséndin, Nauka, Russian Academy of Sciences, St. Petersburg, 1996, pp. 224–279.
[2] H. Pagnia and N. Sotnik, Phys. Status Solidi A **108**, 11 (1988).
[3] K. E. Petersen and D. Adler, Appl. Phys. Lett. **27**, 625 (1975).
[4] B. T. Kolomiets, É. A. Lebedev, I. A. Taksami, and K. D. Tséndin, Fiz. Tekh. Poluprovodn. **17**, 119 (1983) [Sov. Phys. Semicond. **17**, 75 (1983)].

[5] A. Madan and M. Shaw, *The Physics and Applications of Amorphous Semiconductors*, Academic Press, N. Y., 1988; Mir, Moscow (1991), 670 pp.
[6] I. O. Kulik and A. G. Pedan, Zh. Éksp. Teor. Fiz. **79**, 1469 (1980) [Sov. Phys. JETP **52**, 742 (1980)].
[7] L. N. Bulaevskiĭ, A. A. Sobyanin, and D. I. Khomskiĭ, Zh. Éksp. Teor. Fiz. **87**, 1490 (1984) [Sov. Phys. JETP **60**, 856 (1984)].
[8] M. Kastner, D. Adler, and H. Fritzsche, Phys. Rev. Lett. **37**, 1504 (1976).
[9] C. Coulson, *Valence*, Oxford University Press, London, 1961; Mir, Moscow, 1965.
[10] R. F. Street and N. F. Mott, Phys. Rev. Lett. **35**, 1293 (1975).
[11] V. M. Arkhangorodskiĭ, A. N. Ionov, V. M. Tuchkevich, and I. S. Shlimak, JETP Lett. **51**, 67 (1990).
[12] A. M. El'yashevich, A. N. Ionov, M. M. Rivkin, and V. M. Tuchkevich, Fiz. Tverd. Tela (Leningrad) **34**, 3457 (1992) [Sov. Phys. Solid State **34**, 1850 (1992)].

Translated by M. E. Alferieff

Edited by David L. Book

Crystal structure of silver clusters formed on a Si(100)–2×1 surface

M. V. Gomoyunova, I. I. Pronin, and N. S. Faradzhev

A. F. Ioffe Physicotechnical Institute, Russian Academy of Sciences, St. Petersburg
(Submitted December 12, 1997)
Pis'ma Zh. Tekh. Fiz. **24**, 51–56 (April 12, 1998)

The crystal structure of silver clusters formed on the surface of a Si(100)–2×1 single crystal by annealing of a thin Ag film deposited on a slightly heated crystal was studied by diffraction of quasielastically scattered medium-energy electrons. Simulation of the diffraction pattern obtained at 2 keV showed that the silver islands formed on silicon have an ordered structure corresponding to bulk silver and a fixed orientation Ag(100) ∥ Si(100) and $[100]_{Ag} \parallel [100]_{Si}$ relative to the substrate. © *1998 American Institute of Physics.*
[S1063-7850(98)00804-0]

The development of the method of diffraction of quasielastically scattered electrons (QESE) of medium energy[1–3] has opened up the possibility of investigating the atomic structure of objects which do not possess long-range order. This applies in full measure to the study of the atomic structure of impurity clusters (islands) formed on the surfaces of different single crystals. Specifically, this possibility was used in Ref. 4 to study the crystal structure of silver islands formed on a Si(111)–7×7 surface. It is of interest to determine the atomic structure of silver clusters formed on Si(100)–2×1. In contrast to the Ag/Si (111) system, which has been widely investigated for many years by different surface-sensitive methods, much less attention has been devoted to the processes leading to the growth of silver films on Si(100)–2×1 and to the formation of islands on this surface. This is due to the more complicated mechanism of Ag film growth at the initial stage.[5–8] Interest in the Ag/Si(100)–2×1 system has increased in the last three or four years, but not all aspects of this system are adequately understood even now, and many of the results obtained remain contradictory.[5–11] It should be noted that the main method of investigation and the main source of information in most work performed in recent years was scanning tunneling microscopy, so that the conclusions concerning the atomic structure of silver clusters are based mainly on structural data characterizing only the top monolayer. Moreover, according to Ref. 12, the interaction of the microscope tip with the silver film can be quite strong and can distort the initial morphology of the film. For this reason, the objective of the present work was to study by a direct method, using the diffraction of medium-energy QESE, the crystal structure of Ag islands formed on Si(100)–2×1.

The measurements were performed in a secondary-electron spectromete with angular resolution, described in Ref. 13. The energy resolution of the analyzer was equal to 0.4% and the angular resolution was equal to 1°. Information on the method for obtaining diffraction patterns in the form of two-dimensional maps of the QESE intensity distribution over polar and azimuthal angles of emergence is given in Ref. 14. The surface of the silicon single crystal was cleaned by high-temperature heating in an ultrahigh vacuum. The atomic composition of the surface and the thickness of the deposited silver layer were monitored by Auger-electron spectroscopy. Silver was deposited by a sublimation method on the surface of a crystal with a temperature of about 60 °C. To form Ag clusters the sample was subjected to brief annealing up to a temperature of 500°C. The diffraction patterns were obtained at room temperature in a 5×10^{-10} Torr vacuum.

The QESE diffraction pattern obtained for Si(100)–2×1 at 2 keV is shown in Fig. 1a. It clearly demonstrates the anisotropic character of electron reflection from a Si(100) single crystal and differs sharply from the pattern which we obtained earlier[15] for Si(111). Comparison of this pattern with the stereographic projection of the Si(100) shown in Fig. 1b reveals that the symmetry of the pattern reflects the symmetry of this face. This question will be analyzed in greater detail elsewhere. Here we indicate only that the main mechanism leading to the formation of the pattern under discussion is due to the focusing of the QESE, and its principal diffraction maxima and the fringes of high intensity correspond to emergence of electrons along the closest-packed directions (⟨110⟩ and ⟨111⟩) and planes ({100}) of the silicon crystal lattice.

The diffraction pattern obtained for a silver film 25 Å thick is presented in Fig. 1c. One can see that deposition of silver on the single-crystal surface Si(100)–2×1 does not change the symmetry of the pattern, which retains a four-fold rotation axis. At the same time, a substantial redistribution of the QESE intensity is observed within the entire field of the pattern. Comparing the data from Figs. 1a and 1c shows that for Si(100) the brightest maxima are oriented in directions making an angle of 55° with the normal to the surface and lie within the Kikuchi bands making angles of 45° and 135° with the horizontal, whereas for the Ag film the most intense diffraction spots are observed for $\theta=45°$ and are located in vertical and horizontal bands of elevated intensity. The symmetry of the obtained pattern suggests that the deposited silver layer is an epitaxial Ag(100) film. A comparison of the main diffraction features of the Kikuchi pattern (see Fig. 1c)

 © 1998 American Institute of Physics

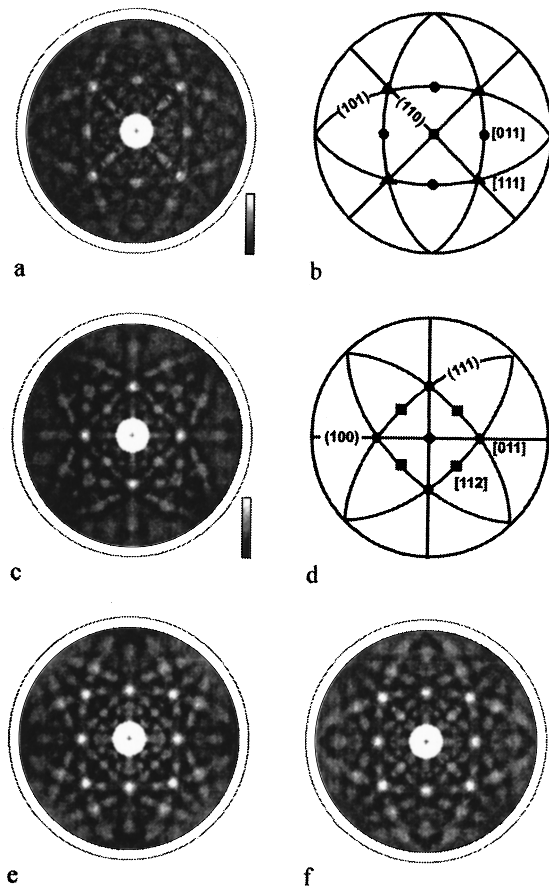

FIG. 1. a — Diffraction pattern of quasielastically scattered 2 keV electrons for Si(100)–2×1; b — stereographic projection of the Si(100) face with designation of the close-packed plane {110}; c — diffraction pattern for a 25 Å thick epitaxial silver film formed on Si(100)–2×1; d — stereographic projection of the Ag(100) face with designation of the close-packed planes {100} and {111}; e — diffraction pattern for a substrate covered with silver clusters (12% coverage); f — result of numerical simulation of the pattern in e.

with the stereographic projection of the (100) face of the fcc crystal, shown in Fig. 1d, supports this conclusion. It is clearly seen that the main maxima and bands of elevated intensity of the diffraction pattern under study are indeed observed in the closest-packed directions ⟨110⟩ and ⟨112⟩ as well as the {100} and {111} planes of the fcc crystal.

Annealing of this Ag film up to temperature $T \approx 500$ °C, where desorption of silver atoms from the surface of the sample starts, alters the diffraction pattern. Together with the persisting diffraction features characteristic of Ag(100), diffraction features characteristic of the substrate also appear. The smallness of the Auger peak of silver observed here suggests that if the signal had been due to a uniform continuous film, then the thickness of the film would correspond to a submonolayer coating. It is easy to see that in this case we would be unable to see the diffraction pattern characteristic for a bulk film of silver. It follows from these data that, just as in the case of the system Ag/Si(111),[4] silver clusters form on the surface of the Si(100) crystal and the observed diffraction pattern is a superposition of patterns from the substrate and silver islands. At the same time, whereas Ag(111) islands formed on the Si(111) surface, Ag(100) clusters with their characteristic orientation $[100]_{Ag} \parallel [100]_{Si}$ relative to the substrate are observed on Si(100).

The results of the numerical simulation of the diffraction pattern studied, performed in a manner similar to the simulation in Ref. 4 for the Ag/Si(111) system using the R_2 factor (the reliability factor describing the deviation of the computed from the measured pattern) for determining the area occupied by Ag clusters on a silicon surface, are shown in Fig. 1f. Good agreement between the experimental and computational results is found in this case as well. It follows from the results obtained that the silver clusters occupy about 12% of the substrate area.

In summary, the structure of the initial surface of the silicon crystal can strongly influence the character of the epitaxial growth of a silver film and silver clusters formed on its surface. When Ag is deposited on a slightly heated Si(100)–2×1 crystal, an epitaxial Ag(100) film with the structure of bulk silver grows on its surface. When this film is annealed up to temperatures at which partial desorption of Ag atoms occurs, Ag(100) islands form on the silicon surface, preferentially with an azimuthal orientation such that the $\langle 100 \rangle_{Ag}$ direction is parallel to the ⟨100⟩ direction of the substrate.

This work was supported by the Russian Fund for Fundamental Research, Project No. 96-02-17966.

[1] S. A. Chambers, Surf. Sci. Rep. **16**, 261 (1992).
[2] M. Erbudak, M. Hochstrasser, and E. Wetli, Mod. Phys. Lett. B **8**, 1759 (1994).
[3] M. V. Gomoyunova, I. I. Pronin, N. S. Faradzhev *et al.*, Fiz. Tverd. Tela (St. Petersburg) **36**, 2295 (1994) [Phys. Solid State **36**, 1250 (1994)].
[4] M. V. Gomoyunova, I. I. Pronin, and N. S. Faradzhev, Zh. Tekh. Fiz. **67**, 62 (1997) [Tech. Phys. **42**, 1429 (1997)].
[5] D. Winau, H. Itoh, A. K. Schmid, and T. Ichinokawa, Surf. Sci. **303**, 139 (1994).
[6] X. F. Lin, K. J. Wan, and J. Nogami, Phys. Rev. B **47**, 10947 (1993).
[7] N. Doraisuwamy, G. Jayaram, and L. D. Marks, Phys. Rev. B **51**, 10167 (1995).
[8] Y. Kimura and K. Takayanagi, Surf. Sci. **276**, 166 (1992).
[9] X. F. Lin, K. J. Wan, and J. Nogamy, Phys. Rev. B **49**, 7385 (1994).
[10] S. M. Shivaprasad, T. Abukava, H. W. Yeom, M. Nakamura, S. Susuki, S. Sato, K. Sakamoto, T. Sakamoto, and S. Kono, Surf. Sci. **344**, L1245 (1995).
[11] D. Winau, H. Itoh, A. K. Schmid, and T. Ichinokawa, J. Vac. Sci. Technol. **12**, 2082 (1994).
[12] T. Hashizume, R. J. Hamers, J. E. Demuth, K. Market, and T. Sakurai, J. Vac. Sci. Technol. A **8**, 249 (1990).
[13] I. I. Pronin, M. V. Gomoyunova, D. P. Bernatskiĭ, and S. L. Zaslavskiĭ, Prib. Tekh. Eksp. No. 1, 175 (1982).
[14] M. V. Gomoyunova, I. I. Pronin, and N. S. Faradzhev, Zh. Éksp. Teor. Fiz. **110**, 311 (1996) [JETP **83**, 1168 (1996)].
[15] I. I. Pronin, N. S. Faradzhev, and M. V. Gomoyunova, Fiz. Tverd. Tela (St. Petersburg) **39**, 752 (1997) [Phys. Solid State **39**, 666 (1997)].

Translated by M. E. Alferieff
Edited by David L. Book

Effect of laser treatment on the gas sensitivity of tin dioxide films

V. A. Loginov, S. I. Rembeza, T. V. Svistova, and D. Yu. Shcherbakov

Voronezh State Technical University

(Submitted August 13, 1997)
Pis'ma Zh. Tekh. Fiz. **24**, 57–60 (April 12, 1998)

It is shown that the sensitivity of antimony-doped polycrystalline SnO_2 films can be increased by treatment with laser pulses. © *1998 American Institute of Physics.* [S1063-7850(98)00904-5]

Tin dioxide (SnO_2) semiconductor films are finding increasing applications as the sensitive components in sensors for different gases.[1,2] The detection principle in such sensors is based on the dependence of the electrical conductivity of SnO_2 films at temperatures 250–300 °C on the composition of the gas medium. One of the main problems in fabricating sensors is obtaining SnO_2 layers with high temperature stability and reproducible properties. For this reason, high-temperature annealing is required in order to achieve the required parameters of SnO_2 films.[3] This can have a negative effect on the other structural components of a sensor. This effect can be eliminated by using pulsed laser treatment, which makes it possible to heat locally a surface layer of the materials to a high temperature within short time intervals.

In the present Letter we report the first results of investigations of the effect of laser treatment on the gas sensitivity of SnO_2 films.

The investigations were performed on samples of antimony-doped (up to 2.6%) polycrystalline SnO_2 films fabricated by the magnetron sputtering method. The magnetron sputtering of a tin target with antimony inserts was performed on glass substrates in an atmosphere consisting of 75% argon and 25% oxygen. The thickness of the films was measured in a MII-4 interference microscope and was equal to 3–5 μm. The laser treatment of the samples was performed on a Kvant-12, operating in the free pulse-generation mode. The wavelength of the radiation was equal to 1.06 μm and the pulse duration was equal to 4 ms. The radiation density E in a pulse was varied in the range 1.5–11 J/cm^2. Laser treatment was performed in air at room temperature with the light normally incident on the surface of the SnO_2 film. The surface resistance of the SnO_2 films, measured by a four-point method at 300 °C, was used as the gas-sensitive parameter. The gas sensitivity of the films before and after laser treatment was investigated with respect to acetone vapor in air.

Table I gives data on the effect of laser treatment on the gas sensitivity of SnO_2 films in acetone vapor in air with acetone concentration 0.75 mg/m^3. The gas sensitivity γ of the films can be estimated according to the relative change in the surface resistance of the films $\gamma=((R-R_0)/R_0)\cdot 100\%$, where R is the surface resistance of the film in the presence of gas and R_0 is the surface resistance of the film in air.

TABLE I. Effect of laser treatment on the gas sensitivity of SnO_2 films.

Sample No.	Laser energy density E, J/cm^2	Gas sensitivity γ, %
1	0	4.7
2	1.5	7.2
3	3	9.5
4	4.6	15.7

It follows from Table I that laser treatment increases the sensitivity of the films to acetone vapor by a factor of 1.5 for energy density 1.5 J/cm^2, a factor of 2 for 3 J/cm^2, and a factor of 3.3 for 4.6 J/cm^2. No visible changes in the state of the film occur. As the radiation energy density increases to 6 J/cm^2, partial separation of the film from the substrate is observed, and at $E=11$ J/cm^2 the film is completely vaporized.

Figure 1 shows the static sensitivity characteristics of the experimental SnO_2 films with respect to acetone vapors. These characteristics represent the dependence of the gas sensitivity on the concentration of the gas being determined.

It follows from the results obtained that laser treatment increases the sensitivity of SnO_2 films to acetone vapor over a wide range of concentrations of the gas being monitored.

The dynamic film characteristics determining the equilibration time in a system with a change of the gas medium are shown in Fig. 2. The arrows ''acetone'' and ''air'' in Fig. 2 represent the introduction and removal of acetone vapor. On the basis of the results obtained, one can see that the laser-annealed films possess better dynamical properties, i.e., their

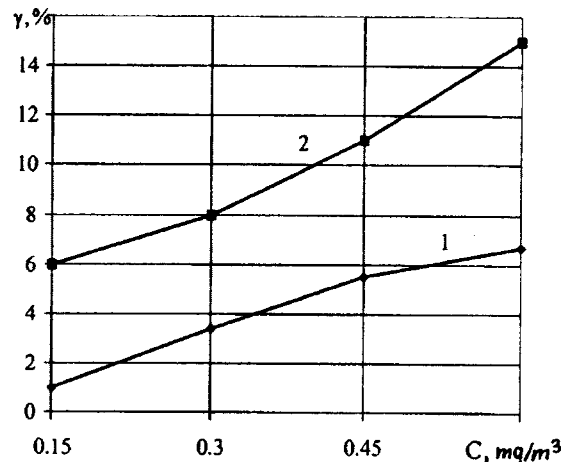

FIG. 1. Static sensitivity characteristics of SnO_2 films with respect to acetone vapors before (*1*) and after (*2*) laser annealing with $E=4.6$ J/cm^2.

 © 1998 American Institute of Physics

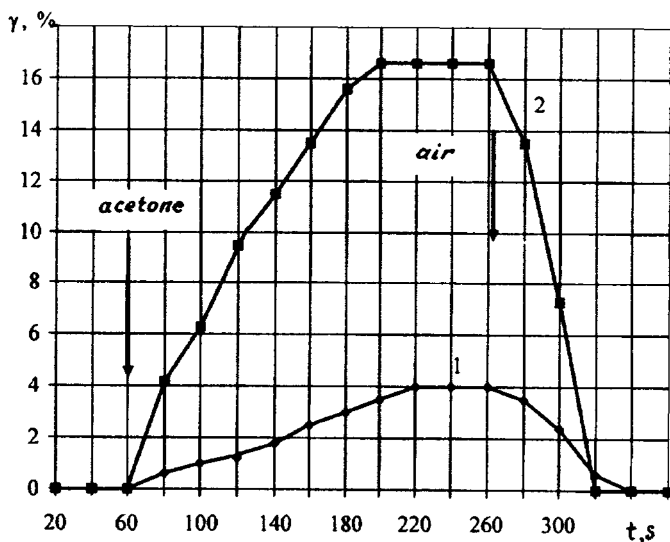

FIG. 2. Dynamic sensitivity characteristics of SnO_2 films with acetone vapor density 0.75 mg/m^3 before (*1*) and after (*2*) laser annealing with $E=4.6\ J/cm^2$.

equilibration time equals 2 min, while the equilibration time of untreated films equals 3 min.

Laser treatment can change the grain size in the film and the phase composition of the film, change the density of the built-in charge and of surface states, and so on. Additional investigations must be performed in order to determine the mechanism by which laser annealing influences the gas sensitivity of SnO_2 films. However, the first investigations show that laser treatment is a promising method for increasing gas-sensitive properties of SnO_2 films.

[1] W. Gopel amd K. D. Shchierbaum, Sens. Actuators B **26-27**, 1 (1995).
[2] A. I. Buturlin, T. A. Garbuzyan, and N. A. Golovanov, Zarubezh. élektron. tekhn. **10**(269), 3 (1983).
[3] V. S. Grinevich, V. V. Serdyuk, and V. A. Smyntyna, Zh. analit. khim. **45**, 1521 (1990).

Translated by M. E. Alferieff
Edited by David L. Book

Laser cleaning of a surface: a method for increasing analytical precision in laser mass spectrometry

P. A. Krasovskiĭ, V. N. Nevolin, V. P. Ivanov, A. N. Pivovarov, and V. I. Troyan

Moscow State Engineering-Physics Institute
(Submitted October 9, 1997)
Pis'ma Zh. Tekh. Fiz. **24**, 61–65 (April 12, 1998)

A method is proposed for increasing the precision of the analysis of the atomic composition of solid materials using the ÉMAL-2 laser energy-mass analyzer. The basic idea of the method is to clean the sample by laser desorption of adsorbed residual gases during the interval between two ionizing laser pulses. A scheme for technical implementation of the proposed method is presented. © *1998 American Institute of Physics.* [S1063-7850(98)01004-0]

One of the main problems in practical mass spectrometry is to increase the precision of the analysis. The most widely used method of investigation of the atomic composition of solid materials is based on the use of laser mass spectrometry, specifically, the ÉMAL-2 laser energy-mass spectrometric analyzer. It is known[1] that though the sensitivity is quite high (~ 0.01 ppm) the measurement precision attained with this method is not very high and equals 30%. Analysis of the possible reasons for such low precision shows that one of the main reasons is uncontrollable contamination of the sample surface by residual gases. The particle concentration on the surface as a result of adsorption of particles (in a low background pressure $p \simeq 10^{-5}$ Torr) can be comparable to the concentration of the elements of the trace impurity being analyzed. Indeed, it is easy to show that in the case of monolayer surface coverage $\theta \simeq N/N_0 \simeq 1$ (N is the number of adsorbed molecules per cm^2 and $N_0 \simeq 10^{15}$ cm^{-2} is the number of adsorption centers) the number of molecules adsorbed on an area $S \simeq 10^{-6}$ cm^2, determined by focusing a laser pulse ($d \simeq 10$ μm), is $N \simeq 10^9$. This value is comparable to the number of trace-impurity atoms at the level $< 10^{-3}$% ($N_{\text{ad}} = 10^{-5} N_\nu V = 10^9$, $N_\nu = 10^{23}$ 1/cm^2, and $V = 10^{-9}$ cm^3 is the volume of the evaporated matter).

The need to increase the analytical precision attained with the ÉMAL-2 mass spectrometer was noted in remarks by the British Service NAMAS during the accreditation at Moscow Engineering-Physics Institute of the procedure for performing analysis of trace impurities in metals and alloys with this apparatus.

We propose below a method for cleaning the surface during analysis of trace impurities that could substantially improve measurement precision.

The flux of molecules from the gas phase onto the surface[2] is

$$j = 3.51 \times 10^{22} p / \sqrt{MT} = 3.5 \times 10^{15}\ \text{cm}^{-2}\ \text{s}^{-1} \tag{1}$$

($p \simeq 10^{-5}$ Torr, $T \simeq 300$ K, $M = 30$ amu). Here it was assumed that at these temperatures the sticking coefficient of molecules on the surface is $C = 1$.[3] The time τ required to cover the surface up to coverage $\theta = 0.1$, which should be compared with the pulse repetition period T of the ionizing laser pulses, can be estimated from the relation

$$j = \frac{\theta N_0}{\tau}.$$

Using Eq. (1) we find $\tau = 10^{-1}$ s. On the other hand, the repetition period of YAG-laser pulses in the Q-switched mode ($\lambda \simeq 1.06$ μm, $\tau_n \simeq 10^{-7}$ s) is $\simeq 10^{-2}$ s. This gives the threshold power ($E = 20$ mJ) required to ionize the matrix of the sample ($p \simeq 10^9$ W/cm^2). In the free-lasing mode we have $\tau_n \simeq 10^{-4}$ s and so $p \simeq 10^6$ W/cm^2. This power is sufficient to clean the surface by laser-stimulated desorption of adsorbed residual-gas molecules.[4] On the other hand, be-

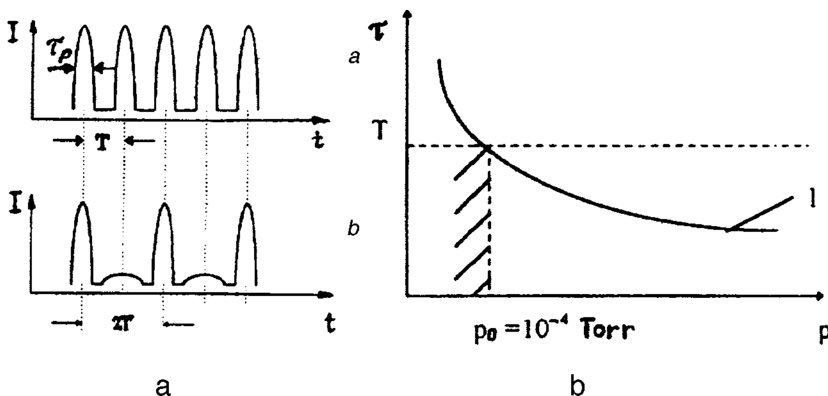

FIG. 1. a — Repetitive-pulse characteristics of the coherent radiation source: *a* — Q-switched mode (period T); *b* — Q-switched mode (period $2T$); free-lasing mode (period $2T$). b — Surface coverage time τ versus pressure p (*1*). Here T is the repetition period of the radiation pulses.

 © 1998 American Institute of Physics

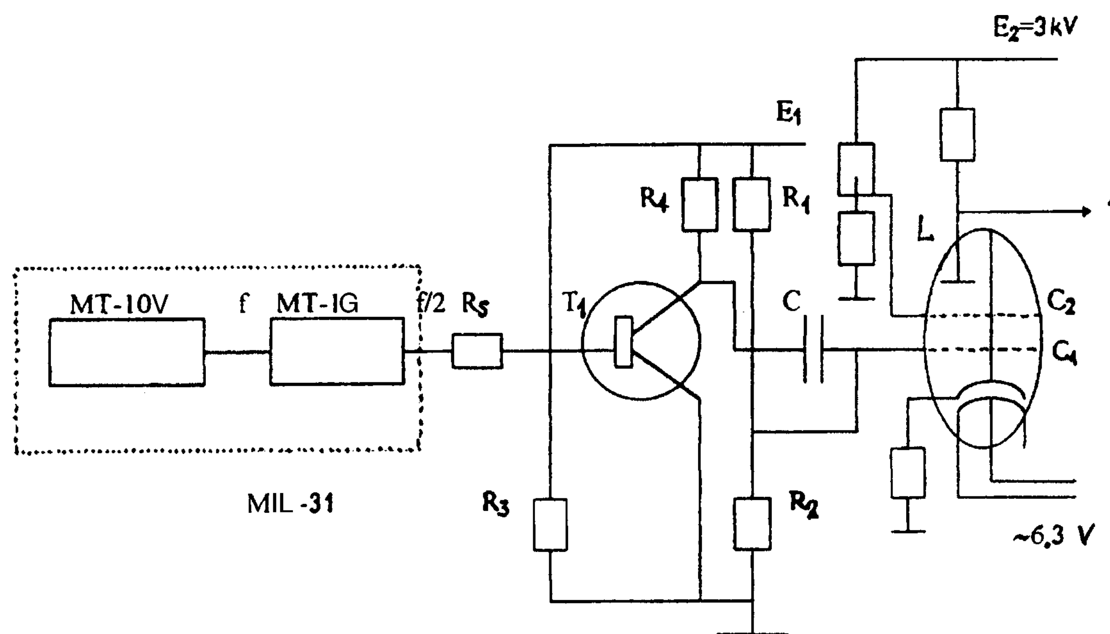

FIG. 2. Block diagram of the scheme implementing the proposed method. *1* — to power supply for the Pockels cell.

cause of the large difference between the binding energies of atoms in the crystal lattice and atoms adsorbed on the surface, this power is insufficient for evaporation and ionization of the trace impurities in the sample.

On this basis we propose the following method for increasing the sensitivity of the ÉMAL-2 analysis: A ''desorbing'' pulse (with free lasing) must follow an ''ionizing'' pulse (with Q-switching) (Fig. 1a). This idea can be implemented by switching to a free-lasing regime in each even pulse. Then if the surface coverage time satisfies $\tau \geqslant T$, by the time the laser pulse ionizing the trace-impurity particles arrives the surface will remain clean up to $\theta = 0.1$. Indeed, as the estimates presented above showed, $\tau = 10^{-1}$ s ($p \simeq 10^{-2}$ Torr) and $T = 10^{-2}$ s, i.e., $\tau/T \sim 10$, which confirms the idea of cleaning the surface during measurements of trace impurities. In accordance with Eqs. (1) and (2) the time satisfies $\tau \sim 1/p$. Figure 1b shows schematically the function $\tau/f(p)$. One can see that for $p < p_0 = 10^{-4}$ Torr ($p_0 \sim 1/T$, $T = 10^{-2}$ s) the inequality $\tau > T$ is observed. At these pressures laser cleaning of the surface of the experimental sample will be observed. This should increase the precision with which trace impurities present in the experimental sample are determined.

The following scheme for forming laser pulses in the free-lasing and Q-switched modes was proposed and implemented in order to use the this laser surface cleaning idea in a practical situation. A block diagram is presented in Fig. 2.

In the conventional scheme for powering a LTI-PCH laser the voltage pulses controlling the formation of the laser pulses with fixed duration ($\tau_p \cong 10$ ns) and repetition frequency $f = 100$ or 50 Hz in the Q-switched mode are formed with a MT-100 univibrator (1) in the MIL-31 modulator unit and then fed into the circuit powering the Pockels cell. To switch the next laser pulse into a free-lasing formation mode the signal from the MT-10v unit is fed into a MT-1G trigger unit (2) which supplements the MIL-31 modulator and decreases the pulse repetition frequency by a factor of 2 ($f/2$). The transistor switch at T_1 controls the switch cascade on the lamp L (GI-30). The resistances R_1 and R_2 are chosen so that in the initial state the lamp L is closed and therefore the voltage on the Pockels cell is $E_2 = 3$ kV (Q-switched mode). When T_1 is interrupted with frequency $f/2$ ($2T$) the positive pulse flows through the capacitance C onto the grid of the lamp C_1 and the lamp opens (free-lasing mode). In this manner the scheme for generating ''shortened'' laser pulses with frequency $f/2$ (Q-switched mode) and with pulses with frequency $f/2$ (free-lasing mode) is realized in practice. This design was tested successfully.

[1] Yu. A. Bykovskiĭ and V. N. Nevolin, *Laser Mass Spectrometry* [in Russian], Énergoatomizdat, Moscow (1985), 122 pp.
[2] D. Woodruff and T. A. Delchar, *Modern Techniques in Surface Science*, Cambridge University Press, N. Y., 1988; Mir, Moscow (1989), 568 pp.
[3] A. Zangwill, *Physics at Surfaces*, Cambridge University Press, N. Y., 1988; Mir, Moscow (1990), 535 pp.
[4] D. M. Zehner and C. W. White, Appl. Phys. Lett. **36**, 56 (1980).

Translated by M. E. Alferieff
Edited by David L. Book

Stochastic generation accompanying parametric excitation of spin waves in yttrium iron garnet films

V. E. Demidov and N. G. Kovshikov

St. Petersburg State Technical University
(Submitted October 2, 1997)
Pis'ma Zh. Tekh. Fiz. **24**, 66–72 (April 12, 1998)

We report the results of experimental investigations of chaotic self-modulation of the envelope of surface spin waves as a result of first-order spin-wave parametric instability. The experimental apparatus consisted of a microwave oscillator with a spin-wave delay line in the feedback circuit.
© *1998 American Institute of Physics.* [S1063-7850(98)01104-5]

Interest in the investigation of the behavior of nonlinear dynamical systems has been increasing in recent years. The properties of such systems are much richer than in the linear case. They lead to a number of unique phenomena. Specifically, the stochastic behavior of deterministic nonlinear systems,[1] especially systems with a large number of degrees of freedom and distributed parameters, is of interest. A ferromagnet in which parametrically coupled spin oscillations and waves exist can serve as such a system.

Stochastic self-modulation of a microwave pump signal accompanying first-order spin-wave instability has been observed in bulk ferromagnetic samples in several treatments.[2,3] This effect has also been investigated for some particular cases in thin ferromagnetic films. The case of a uniform longitudinal pumping was studied in Ref. 4. In Refs. 5 and 6 pumping was performed by direct volume spin waves. Stochastic self-modulation in the case of pumping by surface spin waves has been observed only in Ref. 7, which is devoted to a study of regular self-modulation associated with the nondegeneracy of first-order decay.[8] In this connection, our objective in the present work was to investigate experimentally stochastic self-modulation of surface spin waves in a tangentially magnetized yttrium iron garnet film when first-order spin-wave instability occurs.

It is well known that at some threshold power P_{th} surface spin waves become parametrically unstable with respect to decay into volume waves (see, for example, Ref. 9 and the threshold relations in Ref. 10). The decay efficiency is highest when the temporal and spatial synchronization conditions are satisifed:

$$n\omega_P(\mathbf{k}_P)=\omega_1(\mathbf{k}_1)+\omega_2(\mathbf{k}_2),$$
$$\mathbf{k}_P=\mathbf{k}_1+\mathbf{k}_2, \tag{1}$$

where ω_P, ω_1 and ω_2 are the frequencies of the pump wave and the parametrically excited waves, $\mathbf{k}_P$, $\mathbf{k}_1$, and $\mathbf{k}_2$ are the wave vectors of the pump wave and the parametrically excited waves, and n is the order of the parametric instability (in our case $n=1$). For first-order parametric instability to exist, the three frequencies must fall within the spin-wave spectrum. This happens only under definite conditions. These conditions are determined by the bias magnetization field, the wave number and frequency of the pump wave, and the saturation magnetization and thickness of the film. If $\mathbf{k}_P\approx 0$ holds, i.e., a pump wave is excited near the resonance frequency $\omega_\perp$ of a tangentially magnetized film, the conditions (1) will assume the form

$$\omega_P\approx\omega_\perp,$$
$$\omega_P/2\approx\omega_1(\mathbf{k}_1)\approx\omega_2(\mathbf{k}_2), \tag{2}$$
$$\mathbf{k}_1\approx-\mathbf{k}_2.$$

The conditions (2) hold if $\omega_P=\omega_\perp<2/3\omega_M$ (see, for example, Ref. 11). This is because one-half the pump frequency must fall within the spectrum of volume spin waves. For an yttrium iron garnet film with a magnetization of 1750 G, the frequency of the upper limit of the first-order instability is $\omega_{\perp\max}\approx 3.2$ Hz, which corresponds to a magnetic field $H_0\approx 565$ Oe.

To investigate the self-modulation of surface spin waves we employed an apparatus consisting of a 2–3.3 GHz microwave oscillator with nonlinear spin-wave delay line in the feedback circuit (Fig. 1). The delay line was implemented on a tangentially magnetized 15 μm thick yttrium iron garnet film with a saturation magnetization 1750 G and dissipation parameter per unit length 0.5 Oe. The surface spin waves were excited and detected with 30 μm wide microstrip transducers separated by 10 mm. To ensure single-mode generation the width of the transmission band of the delay line was artificially decreased, for which the yttrium iron garnet film was raised above the transducers to a height $d=100$ μm. In this case only long-wavelength surface waves near the beginning of the spectrum, where $kd<1$ holds, are efficiently excited.[12] The entire structure was placed in a constant magnetic field, whose intensity varied in the range 200–600 Oe, making it possible to tune the frequency of the oscillator. Two Mini-Circuits VNA-25 integrated-circuit amplifiers with 16 dB gain, connected in series, were used as the active component of the oscillator. The gain in the oscillator ring was adjusted with a variable attenuator. Thus, the microwave power P_{IN} at the entrance into the delay line, i.e., the degree of supercriticality of the regime, could be varied. The average power P_{OUT} at the exit of the delay line was essentially independent of P_{IN} and was equal to a value of the order of 42 μW with generation at 2750 MHz.

 © 1998 American Institute of Physics

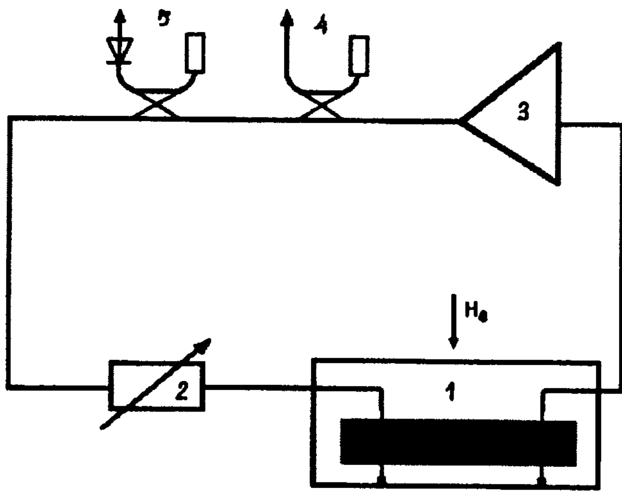

FIG. 1. Experimental apparatus: *1* — delay line, *2* — attenuator, *3* — amplifier, *4* — to spectrum analyzer, *5* — to oscillograph.

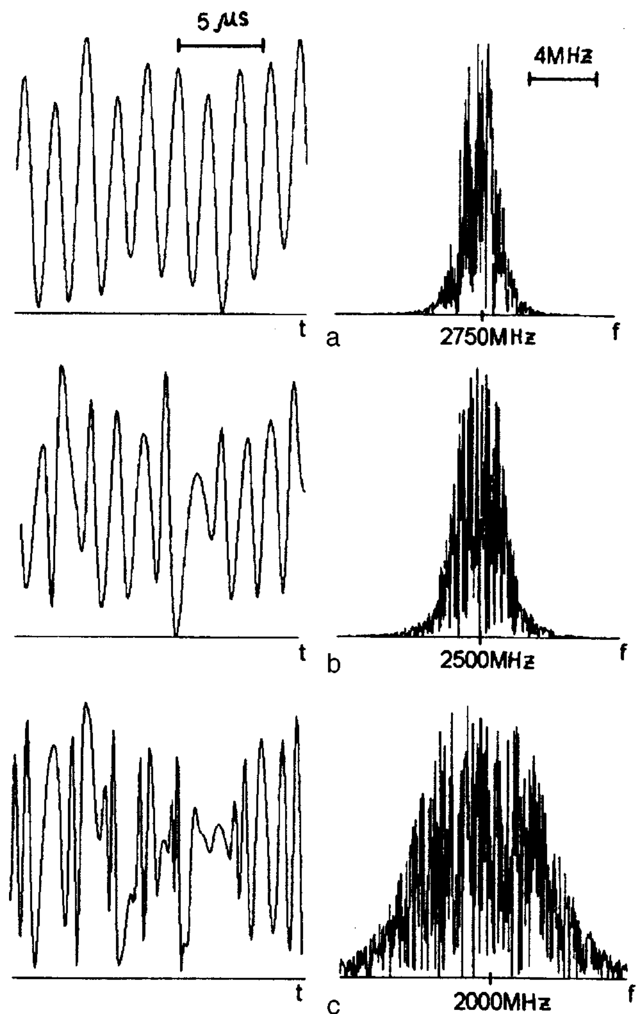

FIG. 2. Oscillograms of the envelope and the power spectra of the microwave signal for different values of the bias magnetization field.

Investigation of the envelope of the output signal gave the following qualitative results: No modulation occurs when $P_{IN}=P_{\mathrm{th}}$. Increasing P_{IN} gives rise to vibrational energy exchange between the pump wave and the parametrically excited wave. In the process, the pump wave is modulated. When the system is slightly supercritical, the modulation is virtually always periodic (the frequency ranges from tens of kilohertz to several megahertz), though the form of the modulation can vary substantially with the bias magnetization field. As supercriticality increases, the periodic oscillations of the envelope evolve into stochastic oscillations. Characteristically, the paths to chaos are different from the well-known model paths, such as transition to chaos via a series of period doubling bifurcations or via intermittency,[13,14] though their elements are observed. Moreover, it was found that the character of the chaos arising and therefore the topology and dimension of the corresponding strange attractor depend strongly on the magnitude of the constant magnetic field.

The development of chaos in weak bias magnetization fields (200–400 Oe) with increasing supercriticality occurs abruptly. The initial periodic modulation loses short-range order, and the signal spectrum broadens.

The onset of chaos via period-doubling bifurcation is observed in fields 400–500 Oe. As the power increased, additional lines corresponding to half-frequencies appeared in the signal spectrum. Further above criticality the lines broadened and merged into a single continuous spectrum.

In fields of the order of 530 Oe modulation remains strictly periodic in a wide range of supercriticality and does not transform into noise-induced modulation. If supercriticality is increased, then at some threshold modulation vanishes.

Modulation was not observed in fields above 580 Oe, where first-order decay processes are forbidden for the wave numbers employed.

Figure 2 displays oscillograms of the envelope and spectra of the generated microwave signal for supercriticalities of the order of 10 dB, corresponding to well developed stochastic behavior. The three cases correspond to three different bias magnetization fields: a) 450 Oe, b) 380 Oe, and c) 250 Oe. It is evident from the figure that as the intensity of the field decreases, the structure of the chaos becomes more and more complicated and the width of the generation spectrum increases. Conversely, as the magnetic field approaches the upper limit for the existence of first-order processes, the structure of the chaos becomes simpler. The envelope oscillations become quasiperiodic.

These results demonstrate the diversity of the stochastic effects that exist in the system studied, and they make it possible to suggest such a system as a tool for studying chaotic dynamics. The results are also of interest from the technical standpoint. They demonstrate the possibility of constructing microwave-range noise generators with a possibility of controlling the structure of the noise by varying the bias magnetization field and the magnitude of the damping in the feedback circuit.

We express our sincere gratitude to B. A. Kalinikos for a discussion of the results obtained in this work.

This work was financed by the Russian Fund for Fundamental Research (Grant 96-02-19515).

[1] M. I. Rabinovich and D. I. Trubetskov, *Introduction to the Theory of Oscillations and Waves* [in Russian], Nauka, Moscow (1992), 454 pp.
[2] A. I. Smirnov, Zh. Éksp. Teor. Fiz. **90**, 385 (1986) [Sov. Phys. JETP **63**, 222 (1986)].
[3] G. Benner and R. Kheĭn, Izv. Vyssh. Uchebn. Zaved., PND **3**, 32 (1995).
[4] G. A. Melkov and S. V. Sholom, Zh. Éksp. Teor. Fiz. **99**, 610 (1991) [Sov. Phys. JETP **72**, 341 (1991)].
[5] A. V. Kozhevnikov and Yu. A. Filimonov, Pis'ma Zh. Tekh. Fiz. **13**, 736 (1987) [Sov. Tech. Phys. Lett. **13**, 306 (1987)].
[6] G. M. Dudko and A. N. Slavin, Fiz. Tverd. Tela (Leningrad) **31**, 114 (1989) [Sov. Phys. Solid State **31**, 979 (1989)].
[7] A. M. Mednikov, Fiz. Tverd. Tela (Leningrad) **23**, 242 (1981) [Sov. Phys. Solid State **23**, 136 (1981)].
[8] A. G. Temiryazev, Fiz. Tverd. Tela (Leningrad) **29**, 313 (1987) [Sov. Phys. Solid State **29**, 179 (1987)].
[9] A. G. Gurevich and G. A. Melkov, *Magnetization Oscillations and Waves* [CRC Press, Boca Raton, FL (1996); Nauka, Moscow (1994), 464 pp.].
[10] B. A. Kalinikos, N. G. Kovshikov, and P. A. Kolodin, in *Abstracts of Reports at the 2nd All-Union School-Seminar on ''Spin-Wave Microwave Electronics''* [in Russian], Ashkhabad, 1985, pp. 77–78.
[11] B. N. Gusev, A. G. Gurevich, and A. N. Anisimov, Fiz. Tverd. Tela (Leningrad) **28**, 2969 (1986) [Sov. Phys. Solid State **28**, 1669 (1986)].
[12] V. F. Dmitriev and B. A. Kalinikos, Izv. Vyssh. Uchebn. Zaved. Fiz. **31**, 24 (1988).
[13] H. G. Schuster, *Deterministic Chaos*, VCH Publishers, 2nd edition; Mir, Moscow (1988), 240 pp.
[14] J.-P. Eckmann, Rev. Mod. Phys. **53**, 643 (1981).

Translated by M. E. Alferieff
Edited by David L. Book

Metastable states of a charged ellipsoidal drop

S. I. Shchukin and A. I. Grigor'ev

Yaroslavl' State University
(Submitted December 8, 1997)
Pis'ma Zh. Tekh. Fiz. **24**, 73–78 (April 12, 1998)

The stability of charged prolate-spheroidal drops of an ideally conducting liquid is investigated on the basis of the principle of minimum potential energy of a closed system in a state of equilibrium. It is shown that metastable states exist in a certain range of charges and spheroidal deformations. © *1998 American Institute of Physics.* [S1063-7850(98)01204-X]

A substantial number of studies concerning the stability of charged drops exist (see, for example, Ref. 1). Rayleigh established that a spherical drop of radius R with surface tension σ and charge Q becomes unstable against infinitesimal spheroidal shape perturbations if $W \equiv Q^2/4\pi R^3\sigma \geqslant 4$.[2] In Refs. 3 and 4 it was concluded that the shape of a spherical drop can bifurcate to prolate and oblate spheroids for $W \geqslant 4$, while in Ref. 4 it was noted that for finite shape perturbations the transition to a stable spheroidal shape is also possible for $W<4$. Analysis of the more general case when a drop has the shape of a triaxial ellipsoid showed that an oblate ellipsoid is not a stable shape of a drop for any values of the parameter W, since for $W<4$ an oblate ellipsoid evolves to a sphere, while for $W \geqslant 4$ it evolves to a prolate spheroid.

In the present Letter the stability of the states of a charged, ideally conducting, prolate spheroidal drop is studied from the standpoint of the minimum of the its potential energy, equal to the sum of the surface tension energy and the electrostatic energy of the intrinsic charge of the drop.

Expressing the potential energy of a charged prolate-spheroidal drop in units of the energy of a spherical drop with the same volume and charge, we obtain the following expression for the dimensionless energy U of the drop as a function of the Rayleigh parameter W and the ratio x of the semiaxes of the prolate spheroid:[5,6]

$$U=\frac{x^{1/3}}{(2+W)\sqrt{(x^2-1)}}\left[\frac{\sqrt{x^2-1}}{x}+x\arcsin\left(\frac{\sqrt{x^2-1}}{x}\right)+W\arccos h(x)\right]. \tag{1}$$

Figure 1 shows plots, calculated according to Eq. (1), of the potential energy $U=U(x)$ of a charged spheroidal drop versus the ratio of the semiaxes for small deformations of the drop and several values of the Rayleigh parameter: $W=3.5$, 3.7, 3.9, 4.1, and 4.3. As noted earlier,[2–4] for $W<4$ a small deformation of a spherical drop increases its potential energy, while for $W>4$ the deformation of a drop to a prolate spheroid decreases the potential energy of the drop, i.e., it is energetically advantageous.

However, analysis of the plots of these curves for large deformations shows that even for $W<4$ these dependences can be nonmonotonic. From Fig. 2, where curves similar to those displayed in Fig. 1 are given for large values of the ratio of the semiaxes of the spheroid, it is evident that when the Rayleigh parameter exceeds a threshold value W_1, be-

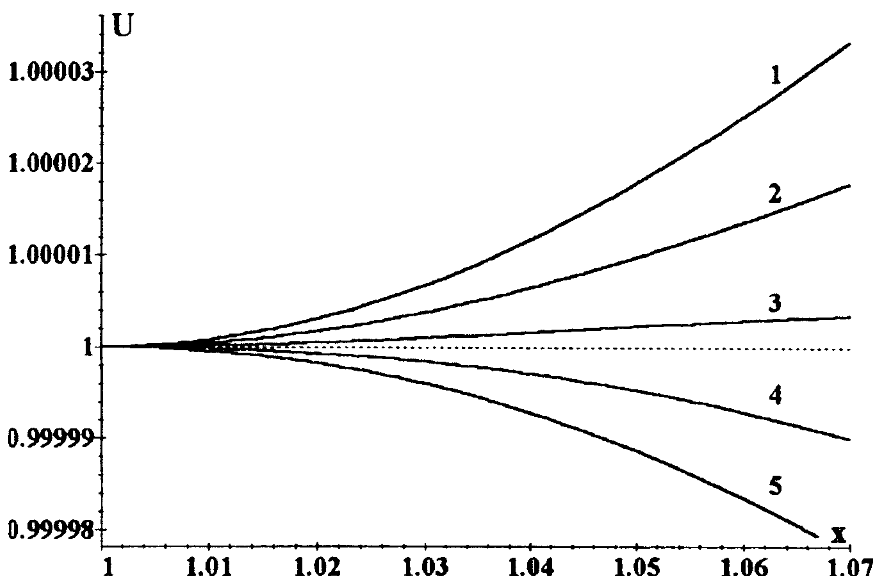

FIG. 1. Plots of the dimensionless energy U of a charged prolate-spheroidal drop versus x (the ratio of the semiaxes of a spheroid) for small deformations and Rayleigh parameters $W=3.5$, 3.7, 3.9, 4.1, and 4.3 — curves *1*, *2*, *3*, *4*, and *5*, respectively.

 © 1998 American Institute of Physics

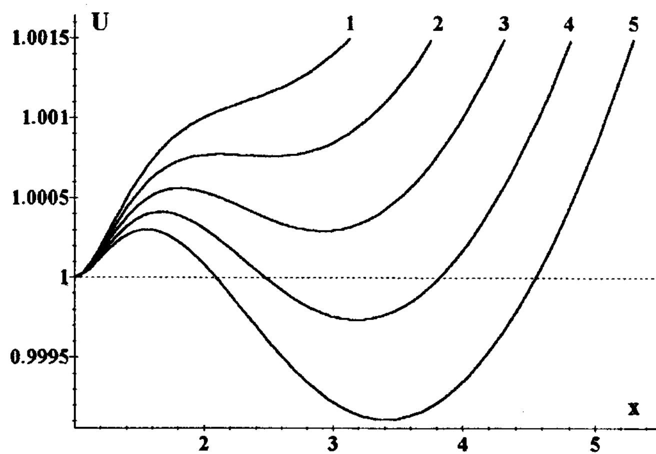

FIG. 2. Plots of the dimensionless energy U of a charged prolate-spheroidal drop versus x (the ratio of the semiaxes of a spheroid) for large deformations and Rayleigh parameters $4W=3.52$, 3.55, 3.58, 3.61, and 3.64 — curves *1*, *2*, *3*, *4*, and *5*, respectively.

sides the minimum at $x=1$ (corresponding to a spherical drop), another local minimum appears in the function $U(x)$ corresponding to a metastable state in which the drop is a prolate spheroid and its energy is greater than that of a spherical drop. As the Rayleigh parameter increases further, the local minimum corresponding to a prolate spheroid continues to deepen, and when W passes through a value W_2 it transforms into a global minimum corresponding to a stable state in which the energy of the prolate-spheroidal drop is lower than that of a spherical drop, but two minima separated by a potential barrier continue to exist. For such values of the Rayleigh parameter the spherical-drop state can be interpreted as metastable. From Fig. 2 it is also evident that as the Rayleigh parameter increases, the value of x corresponding to the position of the minimum also increases, i.e., a drop in a stable (metastable) state becomes more prolate.

Solving the equation $\partial U/\partial x=0$ for W and finding the minimum of the function obtained, we obtain the value of W for which an additional local minimum appears in the potential energy of a charged prolate-spheroidal drop with energy greater than the energy of a spherical drop:

$$W_1=3.545.$$

Solving the equations $\partial U/\partial x=0$ and $U(W,x)=1$ simultaneously, we find the value of W for which the local minimum appearing in the function $U(W,x)$ transforms into a global minimum. In the process, the energy minimum of a spherical drop remains, but the corresponding state becomes metastable

$$W_2=3.596.$$

Now the potential energy of a charged spherical drop is higher than that of a prolate-spheroidal drop, and a transition between the states is possible if the potential barrier separating them is overcome.

This is elucidated in Fig. 3, where the function $U=U(W,x)$ is represented in the form of a three-dimensional surface. The curve AB was obtained from the conditions $\partial U/\partial x=0$, $\partial^2 U/\partial x^2<0$ and passes through the points of local maxima of the function $U(W,x)$. The curve BC was obtained from the conditions $\partial U/\partial x=0$, $\partial^2 U/\partial x^2>0$ and passes through points of local minima of the function $U(W,x)$. The curve DBE represents the function $U(W_1,x)$ and is tangent to the curve ABC. The curve FGH is determined by the function $U(W_2,x)$. The point G of intersection of the curve FGH and the curve BC corresponds to $U=1$ and separates the region of metastable states (BG) from the region of stable states (CG) of a charged prolate-spheroidal drop. The projections of the curves DBE, FGH, and AC on the $W-x$ planes separate the plane into four regions:

For $W<3.545$ the function $U(W,x)$ possesses a single minimum corresponding to a stable spherical drop;

For $3.545<W<3.596$ the function $U(W,x)$ possesses two minima, one corresponding to a stable spherical drop and the other to a metastable prolate-spheroidal drop;

For $3.596<W<4$ the function possesses two minima, one corresponding to a metastable spherical drop and the other to a stable prolate-spheroidal drop;

For $W\geqslant 4$ the function $U(W,x)$ possesses a single minimum corresponding to a stable prolate-spheroidal drop.

Conclusions. For Rayleigh parameters in the range $3.545<W<3.596$ there exists a metastable state of a charged

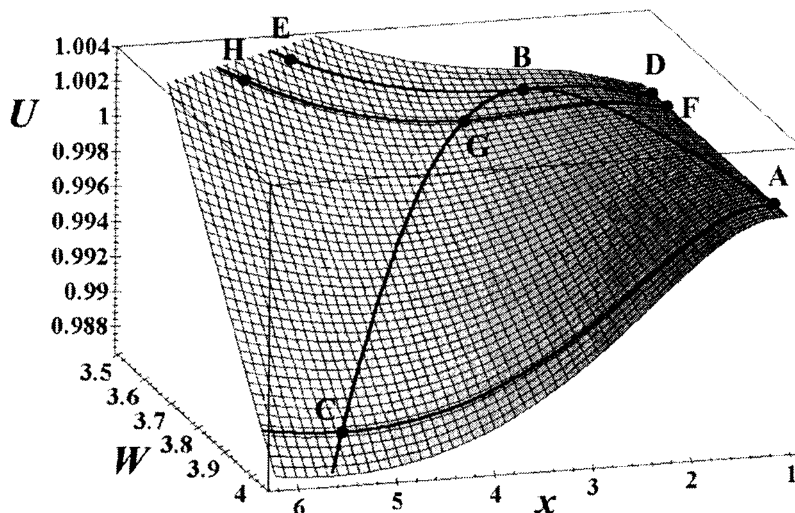

FIG. 3. Plot of the energy $U(W,x)$ of a charged prolate-spheroidal drop versus the Rayleigh parameter W and the ratio x of the semiaxes of the spheroid. The curve ABC marks the extremal values of the energy of the drop: The curve AB corresponds to local maxima and the curve BC corresponds to local minima. The curve DBE marks the values of the energy of the drop for which the Rayleigh parameter $W=W_1$. The curve FGH marks the values of the energy of the drop for which the Rayleigh parameter $W=W_2$. The curve AC corresponds to $W=4$.

prolate-spheroidal drop. The energy of a drop in this state is higher than that of a spherical drop. For $3.596 < W < 4$ a prolate-spheroidal drop has the minimum energy and, though once again there are two minima, the energy of a spherical drop is lower than that of a spheroidal drop. A spherical drop can undergo the transition to spheroidal only by overcoming a potential barrier separating the two minima. As the Rayleigh parameter W increases, the eccentricity of the equilibrium shape of the drop increases. For $W \geqslant 4$ there exists only one minimum, corresponding to a spheroidal drop.

[1] A. I. Grigor'ev and S. O. Shiryaeva, Izv. Ross. Akad. Nauk, Mekh. Zhidkosti i Gaza, No. 3, 3 (1994).
[2] Rayleigh, Philos. Mag. **14**, 184 (1882).
[3] O. A. Bassaran and L. E. Scriven, Phys. Fluids A **1**, 795 (1989).
[4] G. Ailam and I. Gallily, Phys. Fluids **5**, 575 (1962).
[5] L. D. Landau and E. M. Lifshitz, *Fluid Mechanics*, Pergamon Press, N. Y. [Russian original, Nauka, Moscow (1988), 733 pp.].
[6] L. D. Landau and E. M. Lifshitz, *Electrodynamics of Continuous Media*, Pergamon Press, N. Y. [Russian original, Nauka, Moscow (1982), 620 pp.].

Translated by M. E. Alferieff
Edited by David L. Book

Dynamical configurational excitations and the polarization of dielectrics under a load

Yu. A. Khon

Institute of the Physics of the Strength of Materials and Materials Science, Siberian Branch of the Russian Academy of Sciences, Tomsk

(Submitted November 20, 1997)
Pis'ma Zh. Tekh. Fiz. **24**, 79–82 (April 12, 1998)

The polarization of dielectrics, which do not exhibit electrostriction, under a mechanical load is due to dynamical configurational excitations in the loaded crystal. Among these configurations, a dynamical order parameter is identified. It is determined by solving a nonlinear reaction-diffusion equation. The comparatively short buildup time of charge under a load is due to the formation and propagation of a wave of switching. © *1998 American Institute of Physics.* [S1063-7850(98)01304-4]

In natural marble, which does not exhibit electrostriction, an electric field arises under the action of a mechanical load below the yield point.[1] The charge increases up to its maximum value within a time t_σ of several seconds.[1] This is two orders of magnitude shorter than the time t_E under the action of an electric field alone. A charge with the opposite sign arises as the load is removed. The relaxation time of the charge is the same in all cases and close to t_E. Hence it follows that the charge relaxation mechanisms are identical, while the mechanisms leading to the appearance of the charge are different.

The characteristic energies under mechanical loading $\sim 10^{-4}\,G$, where G is the shear modulus, are at most 10^{-8} eV/atom. These values cannot lead to changes of any significance in the thermodynamic parameters, for example, temperature or pressure. In addition, there is no need to attribute the mechanoelectrical effects to phase transformations.

The qualitative changes in the properties of a material are always due to the appearance of new degrees of freedom and the collective excitations associated with them. A comparatively low excitation energy signifies that only low-energy dynamical excitations, arising in the sample under the action of external forces, need be considered. The need to introduce such excitations was pointed out in Ref. 2. In Ref. 3 they were termed dynamical configurational excitations (DCEs). On the basis of such excitations the kinetics of structural relaxation of amorphous alloys has been studied[3] and anomalies of the galvanomagnetic properties of amorphous alloys at low temperatures have been explained.[4] We shall employ DCEs to explain the observed mechanoelectric phenomena.

We consider first a sample which is not subjected to a load and has an arbitrary density of defects (point defects, interfaces, and so on). We specify its structure by the numbers N_j of clusters which possess a short-range order α_j. The quantities N_j and α_j vary continuously as a result of the vibrations of the atoms. Averaging over a time interval that is much longer than the period of the oscillations of the atoms gives a set $\{N_j\}_0$ and $\{\alpha_j\}_0$ corresponding to the initial state.

For an elastically distorted crystal lattice there is a different set $\{N_j\}$ and $\{\alpha_j\}$. This set depends on the time and differs from the initial set, i.e., short-range order in a deformed crystal is of a dynamical character. The transition from one type of dynamical short-range order to another can be interpreted as the appearance of DCEs in the system.[3] These excitations correspond to nonequilibrium states, they depend on the conditions of loading, and they determine the kinetics of the process. When the load is removed, the DCEs vanish but the structural nonuniformities due to them remain. The crystal is in a different metastable state with short-range order different from the initial order.

Of the variety of DCEs arising in a deformed crystal, only some of those with short-range order of the type $\{\alpha_j\}$ lead to polarization of the sample. Their relative fraction η among the total number of DCEs is always less than 1. The quantity $\eta<1$ is an order parameter.

The polarization vector is given by $P=P(\eta)$ and can be expanded in powers of η. The zeroth term in the expansion must equal zero, since $P=0$ for $\eta=0$. The free energy f is determined by the components of the elastic deformation tensor and the polarization vector.[5] The free energy is minimized for each value of the order parameter. But, in contrast to Ref. 5, an equation for the order parameter cannot be obtained by minimizing f.

We shall find this equation from the following considerations. In the balance equation $\partial\eta/\partial t=F(\{k_i\},\eta)-\operatorname{div}\mathbf{j}$ we expand the source function F in a power series in η.

Terminating the expansion at the third-order term and taking $j=-D\Delta\eta$, we obtain

$$\partial\eta/\partial t=k_1\eta+k_2\eta^2-k_3\eta^3+D\Delta\eta. \tag{1}$$

Here k_i are parameters dependent on the temperature and stresses and D is the diffusion coefficient. This equation is known from Refs. 6 and 7. Its solutions are well known.[6–9]

For $a<-b^2/4$ ($a=k_1/k_3$, $b=k_2/k_3$) the system has a single stable stationary solution $\eta=0$. It corresponds to the initial state of the sample with zero polarization. In the parameter range $-b^2/4<a<0$ there exist three stationary solutions: stable $\eta_1=0$, unstable $\eta_2<\eta_3$, and stable $\eta_3=b/2+(b^2/4+a)^{1/2}$. The solution η_3 is absolutely stable for $a>-2b^2/9$, while η_1 is absolutely stable for $a<-2b^2/9$. At the

point $a=-2b^2/9$ both solutions exhibit identical stability. For $a \geqslant 0$ there exist two stationary solutions: unstable $\eta_1=0$ and stable η_3. At the point $a=0$ we have $\eta_1=\eta_2=0$.

The transition from an unstable into a stable state for $-2b^2/9<a<0$ occurs via the formation of a wave of switching $\eta=\eta(x-vt)$. The steady-state velocity v of the wave front[8,9]

$$v=(2Dk_3)^{1/2}(\eta_1+\eta_3-2\eta_2). \qquad (2)$$

At the point $a=-2b^2/9$ we have $v=0$.

In an electric field $t_E \sim L^2/D$, where L is the characteristic size of a polarization nonuniformity in the sample. For $t_E \sim 10^3$ s and $D \sim 10^{-13}$ cm^2/s we obtain $L \sim 10^{-5}$ cm. The time satifies $t_\sigma \sim L/v$. For the same value of L and $t_\sigma \sim 1$ s we find $v \sim 10^{-5}$ cm/s. This value is close to the velocity of a traveling front at the initial stage of plastic deformation.[10] The specific value of v is determined by the parameter k_3, which characterizes the rate of the reactions leading to a change in the initial structure of the crystal.

In summary, a cooperative displacement of atoms in the regime where a wave of switching forms can result in comparatively short charge buildup times under a load. It also follows from the solutions presented that the mechanoelectric effect can be observed only under loads above a critical value. The experimental confirmation of the threshold character of the polarization of a dielectric under a load will prove the correctness of the model proposed for the phenomenon.

[1] V. S. Kuksenko and Kh. V. Makhmudov, Pis'ma Zh. Tekh. Fiz. **23**(3), 89 (1997) [Tech. Phys. Lett. **23**, 126 (1997)].

[2] V. E. Egorushkin, V. E. Panin, E. V. Savushksin, and Yu. A. Khon, Izv. Vyssh. Uchebn. Zaved. Fiz. **30**, 9 (1987).

[3] V. E. Egorushkin and N. V. Mel'nikov, Zh. Éksp. Teor. Fiz. **103**, 189 (1993) [JETP **76**, 103 (1993)].

[4] V. E. Egorushkin and N. V. Mel'nikov, Zh. Éksp. Teor. Fiz. **103**, 555 (1993) [JETP **76**, 280 (1993)].

[5] R. Blinc and B. Žekš, *Soft Modes in Ferroelectrics and Antiferroelectrics*, North-Holland, Amsterdam, 1974; Mir, Moscow, 1975.

[6] A. N. Kolmogorov, I. G. Petrovskiĭ, and N. S. Piskunov, Byul. Mosk. Gos. Universiteta, Matematika i mekhanika **1**, 1 (1937).

[7] R. Fischer, Ann. of Eugenics **7**, 355 (1937).

[8] V. A. Vasil'ev, Yu. M. Romanovskiĭ, and V. G. Yakhno, *Autowave Processes in Kinetic Systems*, Moscow, 1987; Dordrecht, Boston, 1986.

[9] M. V. Ognev, S. V. Petrovskiĭ, and V. M. Prostokishin, Zh. Tekh. Fiz. **65**, 1 (1995) [Tech. Phys. **40**, 521 (1995)].

[10] L. B. Zuev and V. I. Danilov, Fiz. Tverd. Tela (St. Petersburg) **39**, 1399 (1997) [Phys. Solid State **39**, 1241 (1997)].

Translated by M. E. Alferieff

Edited by David L. Book

Modulation of capillary oscillations of a charged drop of low-viscosity liquid by its elastic oscillations

S. O. Shiryaeva and O. A. Grigor'ev

Yaroslavl' State University

(Submitted September 19, 1997)
Pis'ma Zh. Tekh. Fiz. **24**, 83–87 (April 12, 1998)

A second-order linear differential equation describing the temporal evolution of the amplitudes of capillary waves in a drop of low-viscosity liquid with elastic properties is given with a complex coefficient multiplying the first derivative. It is shown that the capillary oscillations of the drop are modulated by its oscillations associated with the relaxation of the viscosity of the liquid. © *1998 American Institute of Physics.* [S1063-7850(98)01404-9]

Capillary and elastic oscillations of a spherical drop of a viscous liquid are of interest for a very wide range of problems of technical physics, geophysics,[1] nuclear physics,[2] and cosmogony.[3] The general laws governing small-scale wave phenomena in a viscoelastic liquid have been investigated in Ref. 4. However, some specific questions concerning this problem, for example, the interaction of capillary and elastic waves, have still not been studied. In this connection, we shall analyze this problem for the case of a low-viscosity liquid, where it is possible to write out the equation of temporal evolution of the amplitudes of waves on the free surface of the liquid.

1. Let us examine a spherical drop of radius R of a viscous incompressible liquid with density ρ and kinematic viscosity ν. Infinitesimal-amplitude capillary waves due to the thermal motion of the molecules of the liquid are present on the surface of the drop. Let the liquid be a dielectric with permittivity ε, while the charge Q of the drop is distributed uniformly over its volume.

The equations of electrodynamics with electrostatic potential Φ, generated by the charge Q distributed in the liquid, have the following form in a spherical coordinate system with origin at the center of the drop:[5]

$$\frac{d\mathbf{U}}{dt}\equiv\frac{\partial\mathbf{U}}{\partial t}+(\mathbf{U}\cdot\boldsymbol{\nabla})\mathbf{U}=-\frac{1}{\rho}\nabla P^{\text{in}}+\nu\cdot\Delta\mathbf{U},\qquad \operatorname{div}\cdot\mathbf{U}=0,$$

$$\Delta\Phi^{\text{in}}=-\frac{3Q}{4\pi\varepsilon R^3};\qquad \Delta\Phi^{\text{ex}}=0,$$

$r=R+\xi$:

$$\frac{dF}{dt}\equiv\frac{\partial F}{\partial t}+\mathbf{U}\cdot\boldsymbol{\nabla}F=0,$$

$$F(\mathbf{r},t)\equiv r-R-\xi(\theta,\phi,t)=0.$$

$$\boldsymbol{\tau}\cdot(\mathbf{n}\cdot\boldsymbol{\nabla})\mathbf{U}+\mathbf{n}\cdot(\boldsymbol{\tau}\cdot\boldsymbol{\nabla})\mathbf{U}=0,$$

$$-(P^{\text{in}}-P^{\text{ex}})-2\rho\nu\mathbf{n}\cdot(\mathbf{n}\cdot\boldsymbol{\nabla})\mathbf{U}+P_\sigma-P_{\mathbf{E}}=0,$$

$$\Phi^{\text{in}}=\Phi^{\text{ex}};\qquad \varepsilon\frac{\partial\Phi^{\text{in}}}{\partial n}=\frac{\partial\Phi^{\text{ex}}}{\partial n},$$

$r=0$:

$$\Phi^{\text{in}}=0;$$

$r\to\infty$:

$$\Phi^{\text{ex}}=0.$$

$$P_\sigma(\xi)=\frac{2\sigma}{R}-\frac{\sigma}{R^2}(2+L)\xi(\theta,\phi,t);$$

$$L\equiv\frac{1}{\sin\theta}\frac{\partial}{\partial\theta}\left(\sin\theta\frac{\partial}{\partial\theta}\right)+\frac{1}{\sin^2\theta}\frac{\partial^2}{\partial\phi^2};$$

$$P_{\mathbf{E}}=-\frac{3Q}{4\pi R^3}\Phi^{\text{in}}+\frac{(\varepsilon-1)}{\varepsilon}\frac{(E_n^{\text{ex}})^2}{8\pi}+(\varepsilon-1)\frac{(E_\tau^{\text{ex}})^2}{8\pi}.$$

In these expressions the function $\xi(\theta,\phi,t)$ describes the perturbation of the equilibrium spherical surface of the drop; P^{ex} is the pressure exerted by the external medium on the surface of the drop; $P^{\text{in}}(\mathbf{r},t)$ is the pressure inside the liquid; $\mathbf{U}(\mathbf{r},t)$ is the velocity field of the liquid; P_σ is the Laplace pressure beneath the distorted spherical surface of the drop; $\Phi^{\text{in}}(\mathbf{r},t)$ is the potential of the electric field inside the liquid; and, E_n^{ex} and E_τ^{ex} are the normal and tangential components of the electric field generated outside the drop by the intrinsic charge of the drop.

If we solve the problem by the method described in detail in Refs. 5 and 6, it is easy to show that in the indicated dimensionless variables the equations describing the temporal evolution of the amplitudes X_n of capillary oscillations obtained by solving the problem in the low-viscosity approximation take the form

$$\frac{d^2X_n}{dt^2}+2\alpha_n\frac{dX_n}{dt}+\omega_n^2X_n=0;\tag{1}$$

$$\omega_n^2=\frac{\sigma}{\rho R^3}\left[n(n-1)(n+2)-n(n-1)\frac{(\varepsilon-1)^2n+5\varepsilon+1}{\varepsilon(\varepsilon n+n+1)}W\right];$$

 © 1998 American Institute of Physics

$$W=\frac{Q^2}{4\pi\sigma R^3};\quad \alpha_n=\frac{\nu}{R^2}(n-1)(2n+1).$$

Here W is the Rayleigh parameter, characterizing the stability of the drop with respect to its intrinsic charge.[1]

2. We now take into account the fact that over short time intervals the liquid possesses the property of elasticity.[7] In analytical calculations on the basis of the continuous-medium model the viscoelastic properties of a liquid can be described by introducing a complex kinematic viscosity by means of Maxwell's formula[7,8]

$$\nu=\nu_0(1-i\omega\tau)^{-1}, \tag{2}$$

where ν_0 is the kinematic viscosity at zero frequency, ω is the frequency, τ is the characteristic relaxation time of elastic stresses in the liquid ($\tau\sim 10^{-5}$ s)[9], and $i=\sqrt{-1}$.

Substituting the expression (2) into Eq. (1), we obtain an ordinary differential equation with a complex coefficient multiplying the first derivative:

$$\frac{d^2X_n}{dt^2}+2(\beta_n+i\gamma_n)\frac{dX_n}{dt}+\omega_n^2X_n=0; \tag{3}$$

$$\beta_n=\frac{\nu_0}{R^2}\,\frac{(n-1)\times(2n+1)}{(1+\omega^2\tau^2)};\quad \gamma_n\equiv\frac{\nu_0}{R^2}\,\frac{\omega\tau(n-1)(2n+1)}{(1+\omega^2\tau^2)}.$$

The solution of Eq. (3) to first order in the small viscosity can be written in the form

$$X=X_0\exp(-\beta_n t)\cos(\gamma_n t)\cos(\omega_n t+\delta), \tag{4}$$

where X_0 and δ are integration constants (corrections to the frequency ω_n of capillary oscillations as a result of viscous damping appear only in the approximation quadratic in the viscosity). It is evident from Eq. (4) that two kinds of damped oscillations are realized simultaneously in the drop: capillary oscillations with frequency ω_n and elastic oscillations with frequency γ_n.

The condition that the viscosity of the oscillating drop be small implies that

$$\beta_n/\omega_n\ll 1,\quad \gamma_n/\omega_n\ll 1. \tag{5}$$

Taking account of the conditions (5), one can see from the Eq. (4) that the elastic oscillations of the drop modulate its capillary oscillations. It is easy to see from the expression for ω_n in Eqs. (1) that as the drop charge increases (the parameter W increases), the conditions (5) on the viscosity of the liquid become more stringent.

It is interesting to note that γ_n as a function of $\omega\tau$ has a maximum at $\omega\tau=1$ and vanishes at $\omega\tau=0$ and $\omega\tau\to\infty$.

3. In investigations of the parametric oscillations and the stability of a drop of a viscoelastic liquid with respect to the time-dependent intrinsic or reduced charge, the equations describing the time dependence of the amplitudes of different modes of capillary oscillations are the Mathieu–Hill equations.[1,10,11] In this case, for a low-viscosity drop no change occurs to first order in the viscosity, either in the range of frequencies at which different types of capillary motions of the liquid are realized or in the critical conditions under which parametric instability appears is observed. A correction in the critical conditions for such an instability, due to the elastic properties of the liquid, appears only in third order in the small viscosity.

[1] A. I. Grigor'ev and S. O. Shiryaeva, Izv. Ross. Akad. Nauk, Mekh. Zhidkosti i Gaza, No. 3, 3 (1994).

[2] S. I. Bastrukov and I. V. Molodtsova, Dokl. Ross. Akad. Nauk **350**, 321 (1996).

[3] S. I. Bastrukov, Phys. Rev. E **53**, 1917 (1996).

[4] S. O. Shiryaeva, O. A. Grigor'eva, M. I. Munichev, and A. I. Grigor'ev, Zh. Tekh. Fiz. **66**, 47 (1996) [Tech. Phys. **41**, 997 (1996)].

[5] S. O. Shiryaeva, A. É. Lazaryants, A. I. Grigor'eva *et al.*, Preprint No. 27, Institute of Mechanics, Russian Academy of Sciences, Yaroslavl', 1994, 128 pp.

[6] S. O. Shiryaeva and A. É. Lazaryants, Zh. Vychisl. Mat. Mat. Fiz. **31**, 929 (1992).

[7] Ya. I. Frenkel', *Kinetic Theory of Liquids*, Clarendon Press, Oxford, 1946 [Russian original, Nauka, Leningrad, 1945], 592 pp.

[8] Yu. A. Bykovskiĭ, É. A. Manykin, P. P. Poluéktov *et al.*, Zh. Tekh. Fiz. **46**, 2211 (1976) [Sov. Phys. Tech. Phys. **21**, 1302 (1976)].

[9] B. B. Badmaev, Ch. S. Laĭdabon, B. V. Deryagin, and U. V. Bazaron, Dokl. Akad. Nauk SSSR **322**, 307 (1992).

[10] A. É. Lazaryants and A. I. Grigor'ev, Zh. Tekh. Fiz. **60**, 33 (1990) [Sov. Phys. Tech. Phys. **35**, 1019 (1990)].

[11] S. O. Shiryaeva and A. I. Grigor'ev, Zh. Tekh. Fiz. **62**, 49 (1990) [Sov. Phys. Tech. Phys. **37**, 1071 (1992)].

Translated by M. E. Alferieff
Edited by David L. Book

Holographic memory based on the angular speckle-selectivity of volume holograms

V. B. Markov

Institute of Applied Optics, Ukrainian National Academy of Sciences, Kiev
Center for Studies in Physics, Bogotá, Columbia

(Submitted November 17, 1997)
Pis'ma Zh. Tekh. Fiz. **24**, 88–93 (April 12, 1998)

The possibility of information storage using the angular speckle-selectivity of volume holograms is analyzed. It is demonstrated that such holograms can be used to construct high-capacity memory elements. © *1998 American Institute of Physics.* [S1063-7850(98)01504-3]

1. The selective properties of volume holograms (VHs) have been repeatedly discussed in connection with the possibility of producing high-capacity memory systems based on them.[1–3] It has been shown[4] that the maximum information density N in VHs ($N \sim \lambda^3 \approx 10^{12}$ bits/cm^3) is determined by the wavelength λ of the radiation. It has been proposed that the angular or spectral selectivity of VHs be used as the main mechanism enabling multiple writing.[5–7]

One drawback of the information storage methods based on the dispersion properties of holograms is the selective character of the angular and spectral selectivity. In this connection, successive writing of holograms is done predominantly in the dispersion plane of the grating. Moreover, the oscillatory ($\sin x/x$) dependence of the intensity of the diffracted signal $I_D(\delta\theta, \delta\lambda)$ in the case of detuning from the Bragg conditions results in degradation of the signal-to-noise ratio.[8,9]

In the present Letter the possibility of information storage based on the use of the properties of the angular selectivity of volume holograms recorded with a reference speckle-wave (SWVHs) is analyzed.

2. Let us consider a VH formed by a plane wave $S_0(r) = s\exp(-i\boldsymbol{\sigma}\mathbf{r})$ and a speckle wave $R_0(r)$. It is assumed that reconstruction is performed by the speckle wave, whose spatial structure is identical to that of the write wave $R_0(r)$, while the reconstruction angle θ_{reg} differs from the write angle: $\theta_{\text{reg}} = \theta_{\text{rec}} \pm \delta\theta_A$ ($\delta\theta_A \ll \theta_{\text{rec}}$), where θ_{rec} corresponds to the convergence angle of the beams at the write stage. In this case, the normalized intensity $I_{ND}(\delta\theta_A)$ of the diffracted beam is given by the expression[10]

$$I_{\text{ND}}(\delta\theta_{\text{SP}}) = \frac{I_D(\delta\theta_A)}{I_{D_{\max}}} = \left(\frac{4d}{k_0}\right)^4 \frac{1}{(DLT\delta\theta_A)^2} \left| \int_0^{T\delta\theta_A} \frac{1}{v^2} \times \exp\left[\frac{ik_0}{d} v^2\right] J_1\left(\frac{k_0 D}{2d} v\right) J_1\left(\frac{k_0 L}{2d} v\right) dv \right|^2, \tag{1}$$

where $\nu = \delta\theta_A z$, $d\nu = \delta\theta_A dz$, $I_{D_{\max}}$ is the intensity of the diffracted beam with $\delta\theta_A = 0$, T is the thickness of the hologram, d is the diffuser–hologram distance, D and L are, respectively, the diameters of the illuminated part of the diffuser and hologram, $|\mathbf{k}_0| = 2\pi/\lambda$ is the wave vector of the read speckle-beam, and $J_1(x)$ is a Bessel function of the first kind.

In the expression (1) terms of the form $J_1(k_0 D_H \nu/2d)$ and $J_1(k_0 L \nu/2d)$ describe the displacement between the read field and the structure recorded in the volume of the hologram with $\delta\theta_A \neq 0$. Figure 1 shows the dependence $I_{\text{ND}}(\delta\theta_A)$ obtained from Eq. (1) as well as the dependence $I_{\text{GR}}(\delta\theta_A)$ calculated in accordance with Ref. 5 for plane-wave holograms. As follows from the data presented, the selectivity $\Delta\theta_{\text{SP}}$ of a SWVH (determined as $\delta\theta_A$ at $0.5 I_{\text{ND}}$) is related to the average size of a speckle ($\langle\sigma_\perp\rangle = 1.22\lambda L/d$) and under identical write conditions can be "stronger" than the selectivity of the cross-grating $\Delta\theta_{\text{GR}}$. Moreover, comparing the dependences $I_{\text{ND}}(\delta\theta_A)$ and $I_{\text{GR}}(\delta\theta_A)$ shows that the SWVH selectivity is monotonic, unlike the oscillatory dependence $I_{\text{GR}}(\delta\theta_A)$ for a cross grating.

3. Holograms with a reference speckle wave were recorded, using the radiation from a single-frequency laser with $\lambda = 530$ nm, in an asymmetric geometry ($\theta_R = 0°$ and $\theta_S = 15°$, cross grating period $\Lambda \approx 2.0$ μm). $LiNbO_3$:Fe (0.02 wt.%) crystals with thickness $T = 1.5$ mm were used as the recording medium.

To measure the angular selectivity of such holograms, the speckle wave was used to reconstruct them. Changing the value of the angle $\theta_{\text{reg}} \neq \theta_{\text{rec}}$ decreased the value of I_{ND}. The experimental dependences $I_{\text{ND}}(\delta\theta_A)$ with the hologram rotated in the dispersion plane and in a plane perpendicular to the dispersion plane are shown in Fig. 1. As follows from the data presented, an important feature of the SWVH is that the angular speckle selectivity $\Delta\theta_{\text{SP}}$ does not depend on the direction of displacement. This substantially distinguishes it from plane-wave holograms.[5] Moreover, the dependences presented confirm that it is possible to record a hologram whose angular selectivity is higher than the selectivity of the cross grating recorded under similar conditions.

4. The angular selectivity mechanism of a SWVH described above permits multiple writing of information and construction of a memory element based on this mechanism. In the experimental implementation of such an element, successive writing was done by changing the angle of incidence θ_{rec} of the speckle wave. The angular detuning $\delta\theta_A \leq 8'$ was chosen from the condition $\delta\theta_A \gg \Delta\theta_{\text{SP}} \approx 1'$, which ensures

 © 1998 American Institute of Physics

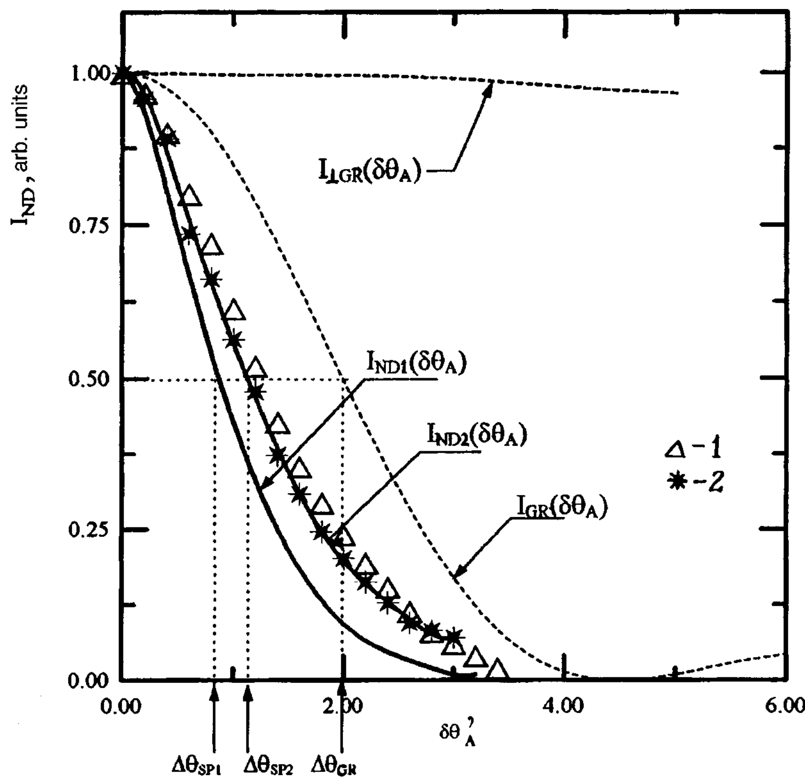

FIG. 1. Normalized intensity I_{ND} of the diffracted beam as a function of the displacement angle $\delta\theta_A$ for several values of the average speckle size ($I_{\mathrm{ND1}}-\sigma_\perp=5.0$ μm; $I_{\mathrm{ND2}}-\sigma_\perp=8.0$ μm) and the angular selectivity of the plane-wave grating in the dispersion plane I_{GR} and in a direction perpendicular to it $I_{\perp\mathrm{GR}}$. Experimental dependences of the angular speckle-selectivity for $\sigma_\perp\approx 8.0$ μm: 1 — Rotation in the dispersion plane of the grating; 2 — rotation in a perpendicular plane.

substantial suppression of the intensity of the total signal ($I_{D\Sigma}\leqslant 10^{-2}I_{D_{\max}}$) formed as a result of the diffraction of the reconstructing wave by the other holograms.

Figure 2 shows the spatial-angular structure of the diffraction maxima that are formed when an element of the holographic memory is reconstructed on the basis of the angular-selectivity mechanism. To each maximum I_{Di} there corresponds to a reconstruction angle $\delta\theta_{Ai}$, variation of which leads to successive reading of the signal wave. One can see from Fig. 2 that the contour of the angular selectivity $\Delta\theta_{\mathrm{SP}}$ remains constant and its value does not depend on the read direction.

To analyze the information write density obtained by the mechanism of angular speckle-selectivity, we note the axisymmetric character of the dependence $I_{\mathrm{ND}}(\delta\theta_A)$ in the plane of the recording medium. This is due to the statistical homogeneity of the intensity distribution in the structure of the reference beam in this plane. The number N of holograms successively recorded in the volume of the crystal can be estimated as

$$N=\frac{4\pi\psi}{(\delta\theta_A)^2}, \tag{2}$$

where ψ is the range of angles where writing is possible ($0<\psi<90°$). Taking account of the data presented above for $\Delta\theta_{\mathrm{SP}}$ (Fig. 1), we estimate the number of holograms from

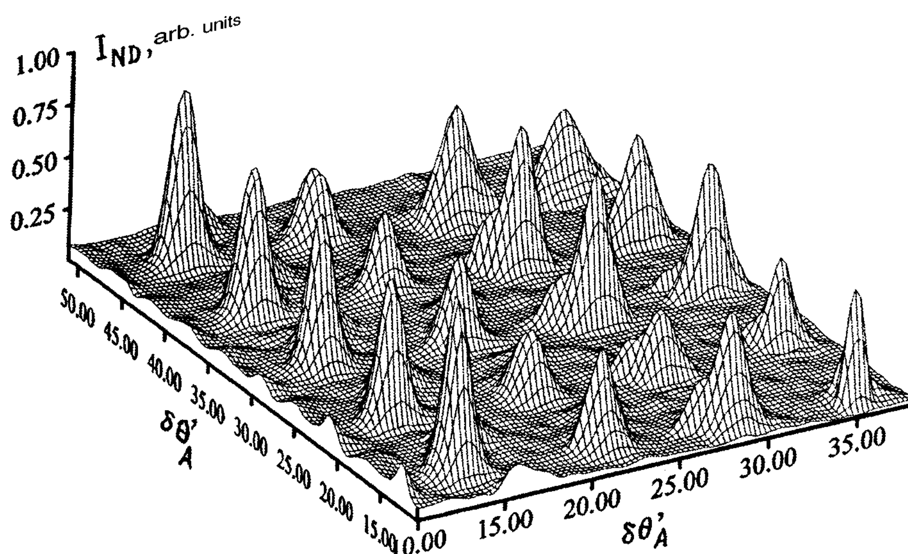

FIG. 2. ''Memory element'' formed as a result of successive sampling of a hologram recorded with a reference speckle wave with angular displacement in two orthogonal directions.

Eq. (2) as $N \approx 10^7$, which is $2\pi/(\delta\theta_A)$ times larger than the corresponding value obtained by writing with plane waves.[3,11]

5. By analogy to Refs. 1, 3, and 9, the signal-to-noise ratio of a holographic memory element based on speckle-angular selectivity can be calculated as

$$SNR = \frac{I_{qD}}{\sum_{m \neq q}^{N} I_{mD} + I_{PC}}, \tag{3}$$

where I_{qD} and I_{mD} are the measured values of the useful signal and the noise. The noise is due to diffraction of the read wave by the *m*th hologram. The term I_{PC} represents the noise determined by the characteristics of the recording medium.

Under the conditions of formation of a speckle wave when the diffuser is illuminated by a beam with a Gaussian intensity distribution (to calculate the expression (1)) and neglecting the noise I_{PC} due to the medium, the expression (3) can be put into the form

$$SNR = \frac{I_{qD}}{\sum_{m \neq q}^{N} \exp[(m\,\delta\theta_A - \Delta\theta_{SP})^2]}. \tag{4}$$

The value of the SNR calculated from Eq. (4), taking account of the $\delta\theta_{SP}$ data (Figs. 1 and 2), is $\sim 10^{-3}$ with 10^4 holograms recorded.

6. In conclusion, we note that in the present Letter the characteristic features of the angular selectivity of volume holograms of a speckle structure were analyzed and it was demonstrated that high-capacity memory elements can be constructed on the basis of such holograms.

I am grateful to the Columbian Institute for the Development of Science and Technology ''COLCIENCIAS'' for partial support of the work as part of Project No. 28-05-401-93.

[1] A. L. Mikaélyan, *Optical Methods in Informatics* [in Russian], Nauka, Moscow, 1990.
[2] D. Bradly and D. Psaltis, Opt. Quantum Electron. **25**, 597 (1993).
[3] J. Hong, I. McMichel, T. Chang, W. Christian, and E. Paek, Opt. Eng. **34**, 2193 (1995).
[4] P. J. Van Heerden, Appl. Opt. **2**, 393 (1963).
[5] H. Kogelnik, Bell Syst. Tech. J. **48**, 2909 (1969).
[6] D. Bradly and D. Psaltis, Opt. Soc. Am. A **9**, 1167 (1992).
[7] F. Mok, Opt. Lett. **18**, 915 (1993).
[8] H. Lee, Opt. Lett. **13**, 874 (1988).
[9] K. Curtis, C. Gu, and D. Psaltis, Opt. Lett. **18**, 1001 (1993).
[10] V. B. Markov, J. Imaging Sci. Technol. **41**, 70 (1997).
[11] K. Rastani, Appl. Opt. **32**, 3772 (1993).

Translated by M. E. Alferieff
Edited by David L. Book

Twinning of bismuth single crystals bombarded by boron ions

V. S. Savenko, V. V. Uglov, O. M. Ostrikov, and A. P. Khodoskin

Mozyr' State Pedagogical Institute;
Belarus State University, Minsk
(Submitted August 27, 1997)
Pis'ma Zh. Tekh. Fiz. **24**, 1–9 (April 26, 1998)

Twinning of ion-bombarded single crystals has been investigated for the first time. It has been established that bombardment of bismuth single crystals with boron ions stimulates mobility of twinning dislocations and quenches their sources. This result is explained using the dislocation model of a wedge-shaped twin. © *1998 American Institute of Physics.*
[S1063-7850(98)01604-8]

INTRODUCTION

Studies of twinning in metals are potentially useful from the scientific viewpoint as well as for practical applications of structural materials whose plastic deformation takes place by twinning.[1–5] At present, many researchers are focusing their attention on analyses of dislocation mechanisms responsible for changes in the physical properties of crystals.[6–9] This is because for the vast majority of materials, plastic properties are achieved by the evolution of sets of dislocations. However, in some materials such as alpha iron, silicon iron, zinc, and so on, plastic deformation takes place by means of a twinning process. Thus, there is no justification for inadequate studies of this type of plastic deformation in metals because this narrows down the range of materials used in production and engineering since their physical properties cannot be predicted.

Here we study the twinning process in bismuth single crystals bombarded with boron ions. This is the first time such an investigation has been carried out and the results suggest that such studies are advisable because ion cluster doping provides a new method of controlling the twinning process and various physical properties of structural materials.

CHOICE OF MATERIAL AND EXPERIMENTAL METHOD

Bismuth was chosen for the investigations because when its (111) cleavage plane is deformed by a concentrated load, a plastic deformation process is established comparatively easily by twinning in three directions (Schmidt factor 0.48). For this reason, bismuth is widely used in this type of research.[1,2]

Boron ion bombardment was used because boron does not dissolve in bismuth[10] so that the influence of chemical compounds formed as a result of interaction between implanted impurities and the bombarded material can be excluded from the analysis.

Bismuth single crystals measuring $50\times10\times5$ mm were grown by the Bridgman method. Samples measuring $10\times5\times4$ mm were cut from the crystal along the (111) cleavage plane.

The freshly cleaved (111) surface of the bismuth single crystal was bombarded with 30 keV boron ions at a dose of 10^{17} ions/cm^2. The treated surface was then deformed by a concentrated load, for which we used the diamond pyramid of a standard PMT-3 microhardness meter. The load on the indenter was varied between 5×10^2 and 30×10^2 N. As a result of the deformation an ensemble of wedge-shaped twins appeared around the impression made by the diamond indenter for which we measured the length L and the width at the mouth (h).

EXPERIMENTAL RESULTS

Six or seven wedge-shaped twins of the type $\{101\}\langle001\rangle$ are usually formed around the impression made by the indenter on the (111) surface of the bismuth single crystal. Figure 1 shows various twins formed near the impression made by the concentrated load.

The results of our investigations indicated that the number of twins formed as a result of the indentation of bismuth single crystals does not depend on the load on the indenter P (Fig. 2). However, the average number of twins N is strongly influenced by the energy action on the crystal. In our case, this action involved the boron ion bombardment of the crystal. It can be seen from Fig. 2 that for samples bombarded with boron ions the average number of twins around the impression made by the indenter is two less than that for the nonbombarded samples, i.e., the processes involved in the generation of twinning dislocations are slowed.

The maximum length of a twin prong (L_m), i.e., the length of the largest twin in an ensemble of twins formed around the impression made by the indenter, increases linearly as the load on the indenter P increases (Fig. 3). For the irradiated samples the length of the twins was greater than that for the unirradiated samples for all loads on the indenter (between 5×10^2 and 30×10^2 N). In this case, we can talk of the stimulation of twinning dislocations running along the interface between the twin and the parent crystal.

QUALITATIVE ANALYSIS OF THE RESULTS

Figure 4 shows a twin formed by a set of twinning dislocations. The plane ADEK corresponds to the (111) cleav-

 © 1998 American Institute of Physics

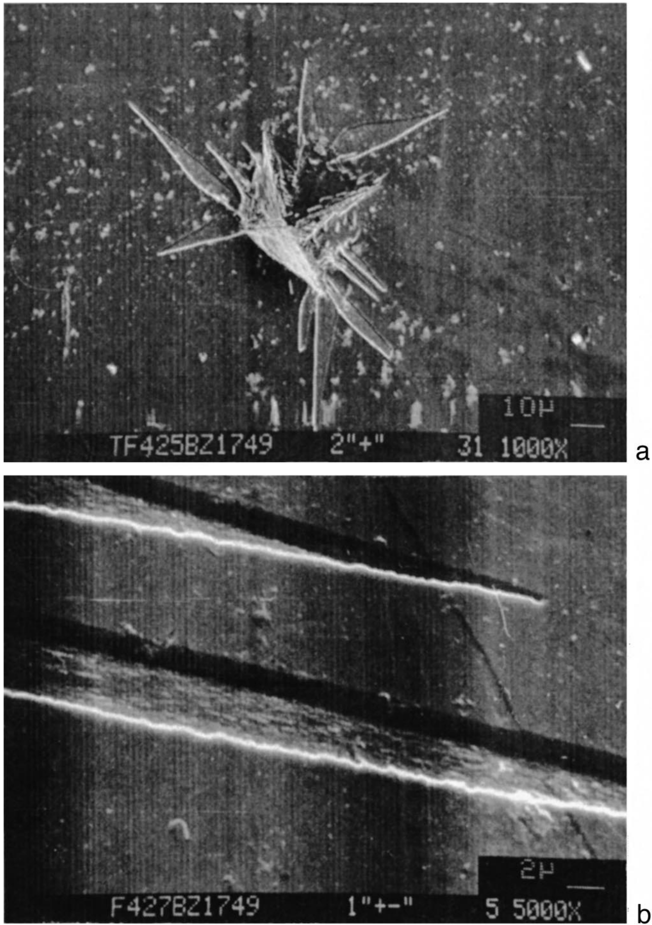

FIG. 1. Twinning of a bismuth single crystal: a—typical pattern of wedge-shaped twins formed near the impression made by an indenter on the (111) plane of a bismuth single crystal; b—magnified image of various twins.

age plane of the bismuth single crystal while the plane ABCD is a transversal passing across the line of action of the force **P** perpendicular to the (111) plane. We shall assume that L is the length of a twin in the (111) plane which is

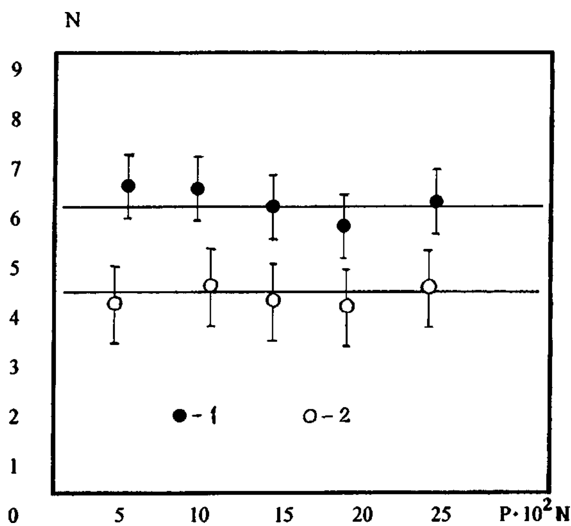

FIG. 2. Average number of twins (N) versus load on indenter (P): *1*—unirradiated crystal and *2*—bismuth single crystal bombarded by boron ions.

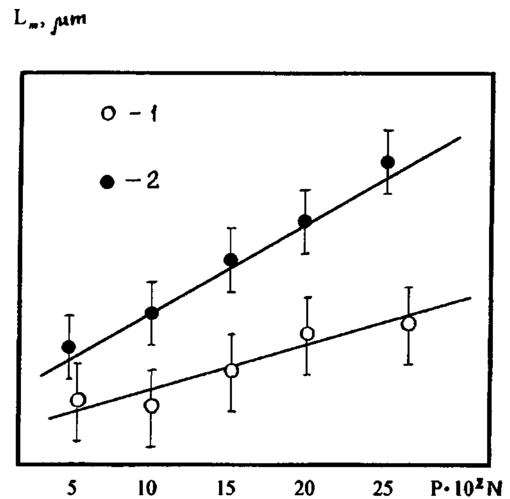

FIG. 3. Maximum length of twin (L_m) versus load on indenter (P): *1*—unirradiated crystal and *2*—bismuth single crystal bombarded by boron ions.

equal to the length of the segment MG (Fig. 4) and L_1 is the distance between the crystal surface and the leading dislocation which penetrates deep into the crystal and is equal to the length of the segment GN. We take the axes of the Cartesian coordinate system as shown in Fig. 4.

At point N the Burgers vector **b** is perpendicular to the line of the leading dislocation whereas at point M it is parallel to this line. As a result from point N to point M the leading dislocation changes smoothly from an edge to a screw dislocation. A similar situation is found for the other twinning dislocations.

The distribution of an implanted impurity in the crystal obeys Pearson's law.[11] The Pearson distribution is an extremum function so that to a rough approximation we can assume that the ions implanted in the material are located at the

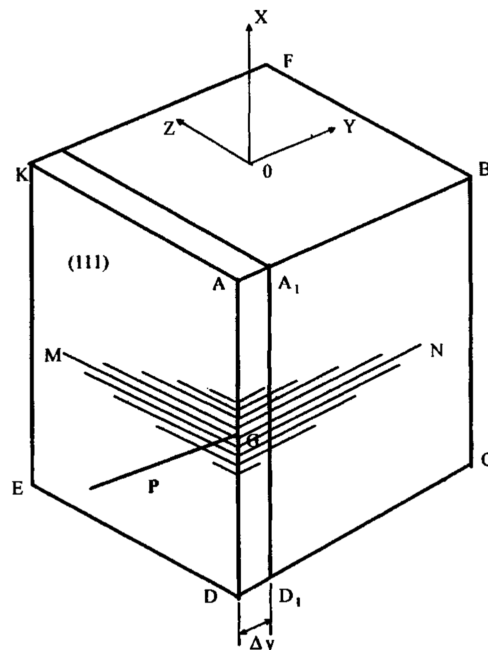

FIG. 4. Representation of twin as set of dislocations.

depth of their maximum concentration in an infinitely thin layer. In Fig. 4 the distance between the crystal surface and this layer is denoted by Δy.

This representation allows us to assume that an implanted impurity in the layer Δy creates stresses distributed uniformly over the plane running parallel to the crystal surface at the distance Δy, which are compensated by surface tension forces on the (111) plane. This means that the calculations of the stress fields in the surface layer can be reduced to the well-known Prandtl problem,[12,13] whereby the components of the deformation tensor for this layer are given by

$$\begin{cases} \sigma_{xx}=-p-k(x/h-2\sqrt{1-(y/h)^2}), \\ \sigma_{yy}=-p-k(x/h), \\ \tau_{xy}=k(y/h), \end{cases} \tag{1}$$

where σ_{xx} and σ_{yy} are the normal stresses and τ_{xy} is the cleavage stress,[14] $h=\Delta y$ is the layer width, k is the material constant, and p is an arbitrary constant.

The stresses created in the crystal by the concentrated load $\mathbf{P}$ acting perpendicular to the crystal surface ($\mathbf{P}\perp(111)$) are determined using the formula[14]

$$\sigma_{rr}=-\frac{2P}{\pi r}, \tag{2}$$

where σ_{rr} is the radial component of the tensor of the stresses created by the force $\mathbf{P}$ applied to a point on the surface of an elastic medium, P is the modulus of this force, and r is the distance between the point of application of the force and some point in the medium.

Along the X axis the edge component of the twinning dislocation is exposed to a climbing force F_x (Ref. 15) which helps the dislocations to overcome obstacles in the form of crystal lattice defects, including those formed as a result of irradiation, as they propagate. The ratio of this force to the length of the dislocation line L is given by

$$F_x/L=b\sigma_{yy}, \tag{3}$$

where b is the modulus of the Burgers vector and σ_{yy} are the normal stresses created in the crystal as a result of ion implantation (see relation (1)).

Along the Z axis the screw component of the twinning dislocation is exposed to the force F_z whose magnitude is determined from

$$F_z/L=b\tau_{xy}, \tag{4}$$

where τ_{xy} are the cleavage stresses determined from relation (1).

The action of these forces on the twinning dislocations increases the length of the wedge-shaped twins.

It should be noted that the length of the twin prong is increased not only by the action of these additional forces on the moving dislocations but also as a result of an increase in the initial velocities of the twinning dislocations caused by an increase in the initial stresses produced by the enhanced stressed state in the surface layer of the material in which the sources of twinning dislocations are situated.

Clearly, for impurities insoluble in the implanted material matrix, an increase in radius and irradiation dose will be accompanied by an increase in the force acting on the twinning dislocations from the implanted layer.

The decrease in the number of twins formed near the impression made by the indenter in an irradiated crystal can be attributed to a reduction in the number of sources of twinning dislocations caused by irradiation-induced changes in the elastic characteristics of the surface layer in which the sources of twinning dislocations are situated.

CONCLUSIONS

As a result of these investigations of the kinetics of twinning in bismuth single crystals bombarded by 30 keV borons ions with a dose of 10^{12} ions/cm^2, it has been established that:

1) an implanted impurity stimulates the mobility of twinning dislocations;

2) the length of the wedge-shaped twins is increased by means of additional forces acting on the screw and edge components of the twinning dislocations and also as a result of an increase in their initial velocities produced by the stressed state of the surface layer in which the sources of twinning dislocations are situated;

3) changes in the elastic characteristics of the surface layer are responsible for the quenching of sources of twinning dislocations as a result of ion bombardment of the crystals.

[1] V. S. Savenko and M. S. Tsedrik, Izv. AN BSSR Ser. Fiz.-Mat. Nauk No. 1, 105 (1980).

[2] V. S. Savenko, V. I. Spitsyn, and O. A. Troitskiĭ, Dokl. Akad. Nauk SSSR **283**, 1181 (1985) [Sov. Phys. Dokl. **30**, 716 (1985)].

[3] M. E. Bosin, F. F. Lavrent'ev, V. V. Nikiforenko, and O. P. Salita, Fiz. Tverd. Tela (St. Petersburg) **37**, 3130 (1995) [Phys. Solid State **37**, 1725 (1995)].

[4] M. E. Bosin, F. F. Lavrent'ev, V. V. Nikiforenko, and O. P. Salita, Fiz. Tverd. Tela (St. Petersburg) **38**, 3619 (1996) [Phys. Solid State **38**, 1972 (1996)].

[5] M. E. Bosin, F. F. Lavrent'ev, V. V. Nikiforenko, and O. P. Salita, Fiz. Tverd. Tela (St. Petersburg) **38**, 3625 (1996) [Phys. Solid State **38**, 1976 (1996)].

[6] V. S. Savenko, O. A. Troitskiĭ, N. P. Lipskiĭ, Yu. V. Baranov, and A. I. Pinchuk, Izv. Akad. Nauk Belarus Ser. Fiz.-Tekh. Nauk. No. 1, 14 (1994).

[7] A. M. Roshchupkin and I. L. Bataronov, Izv. Vyssh. Uchebn. Zaved. Fiz. No. 3, 57 (1996).

[8] M. A. Aliev, Kh. O. Alieva, and V. V. Seleznev, Fiz. Tverd. Tela (St. Petersburg) **37**, 3732 (1995) [Phys. Solid State **37**, 2057 (1995)].

[9] V. V. Sviridov, Fiz. Tverd. Tela (St. Petersburg) **37**, 3097 (1995) [Phys. Solid State **37**, 1707 (1995)].

[10] M. Hansen and K. Anderko, *Constitution of Binary Alloys*, Vol. 1, 2nd. ed. (McGraw-Hill, New York, 1958; Metallurgizdat, Moscow, 1962).

[11] F. F. Komarov, A. P. Novikov, and A. F. Burenkov, *Ion Implantation* [in Russian], Minsk (1994).

[12] L. M. Kachanov, *Principles of Plasticity Theory* [in Russian], Moscow (1969).

[13] V. V. Sokolovskiĭ, *Plasticity Theory* [in Russian], Moscow (1969).

[14] L. D. Landau and E. M. Lifshits, *Theory of Elasticity*, 3rd English ed. (Pergamon Press, Oxford, 1986) [Russ. original, Vol. 8, later ed., Nauka, Moscow, 1987].

[15] J. P. Hirth and J. Lothe, *Theory of Dislocations* (McGraw-Hill, New York, 1967; Atomizdat, Moscow, 1972).

Translated by R. M. Durham

Fabrication of InAs quantum dots on silicon

G. É. Cirlin, V. N. Petrov, V. G. Dubrovskiĭ, S. A. Masalov, A. O. Golubok, N. I. Komyak, N. N. Ledentsov, Zh. I. Alferov, and D. Bimberg

Institute for Analytical Instrumentation, Russian Academy of Sciences, St. Petersburg;
A. F. Ioffe Physicotechnical Institute, Russian Academy of Sciences, St. Petersburg;
Technical University, Berlin, Germany

(Submitted December 19, 1997)
Pis'ma Zh. Tekh. Fiz. **24**, 10–15 (April 26, 1998)

Reflection high-energy electron diffraction and scanning tunneling microscopy have been used to demonstrate for the first time that InAs quantum dots may be fabricated directly on Si(100) by molecular beam epitaxy. It is shown that heteroepitaxial growth in an InAs/Si system takes place by the Stranski–Krastanow mechanism and the surface morphology depends strongly on the substrate temperature. © *1998 American Institute of Physics.* [S1063-7850(98)01704-2]

Silicon is now the most important material for microelectronics. Properties such as its high thermal conductivity, mechanical strength, the availability of large-diameter dislocation-free substrates, and the presence of a stable oxide on the surface make this material irreplaceable for most applications. However, silicon has not found practical applications in optoelectronic devices (lasers, light-emitting diodes, and so on).

This circumstance arises because silicon has an indirect band structure and radiative recombination cannot take place without interaction with an additional particle (such as a phonon). This situation is typical of all indirect-gap semiconductors (such as AlAs and GaP). It is known that for III–V compounds the incorporation of thin quantum-well layers, quantum dots, or quantum wires of a direct-gap material (GaAs, InAs) in an indirect-gap matrix (AlAs) radically improves the radiative recombination efficiency and therefore makes it possible to fabricate lasers and light-emitting diodes.

By analogy with III–V compounds, it may be postulated that the incorporation of quantum dots of a narrow-gap, direct-gap semiconductor (such as InAs) in a silicon matrix can also produce efficient light-emitting devices.[1] A characteristic feature of an InAs–Si system is the large mismatch of the lattice parameters (9%) which makes it impossible to obtain thick dislocation-free layers. Thin layers ($\leqslant 1$ ML) cannot lead to localization of electrons in the direct InAs minimum because of size quantization effects. The lower level for the electrons will be the indirect Si minimum. However, it is known that under certain conditions, in a system with a large lattice mismatch it is possible to obtain elastically strained, coherent three-dimensional crystallites in the nanometer range. In this case, the electron wave function can be effectively localized in the InAs quantum dot if the volume of the quantum dot is fairly large (the lateral dimension of the quantum dot should not be less than 100 Å).

Here we report the fabrication of these InAs quantum dots on an Si surface by molecular beam epitaxy.

Growth experiments were carried out on Si(100) substrates using an ÉP 1203 molecular beam epitaxy system. Samples which had undergone chemical treatment as described in Ref. 2, were fixed to a standard molybdenum holder using indium. The oxide removal and growth processes were monitored using an improved system for recording and processing reflection high-energy electron diffraction (RHEED) patterns.[3] The oxide layer was removed by heating the substrate holder in the growth chamber to 870 °C and holding for 15 min after which the typical surface reconstruction (2×1) for Si(100) was observed. The sample temperature was then reduced and the indium and arsenic shutters were opened simultaneously. The indium flux was precalibrated using the oscillations of the RHEED specular reflection and corresponded to 0.1 ML/s for InAs during growth of an InGaAs solid solution on GaAs with a $\sim 15\%$ molar fraction of indium. After an InAs layer of a specific thickness had been deposited, the growth process was terminated and the sample was cooled rapidly to room temperature. The surface morphology of the samples was examined ex situ using a scanning tunneling microscope (STM). Multiply reproducible, stable STM images were obtained for different sections of the samples. For long-term STM measurements the samples were placed in vacuum oil to protect the surface from oxidation in air.

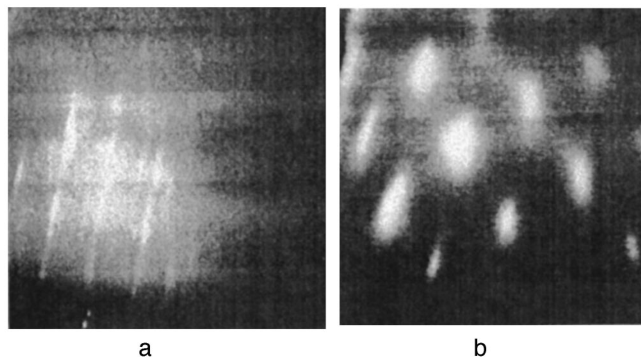

FIG. 1. RHEED patterns obtained at 20 kV in the [011] direction: (a) at $T_s = 470$ °C after deposition of 60 ML InAs and (b) at $T_s = 250$ °C after deposition of 6 ML InAs.

 © 1998 American Institute of Physics

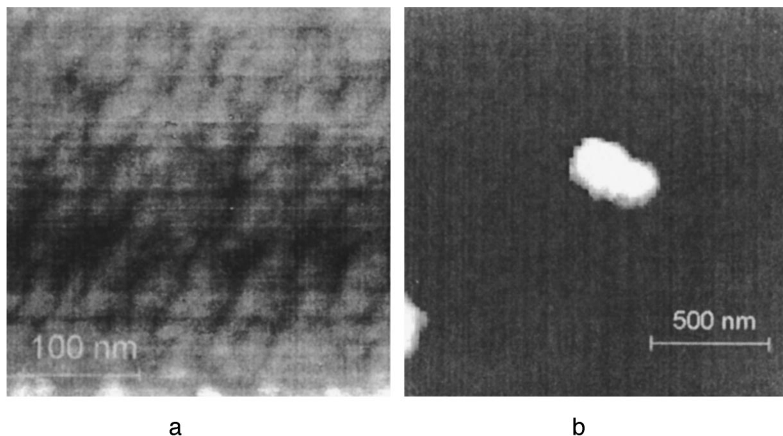

FIG. 2. Scanning tunneling microscope images of InAs/Si surface (a, b) at $T_s = 470$ °C after deposition of 60 ML InAs and (b) at $T_s = 250$ °C after deposition of 6 ML InAs.

A characteristic feature of these quantum-well InAs structures on the Si surface is the strong dependence of the growth mechanism on the substrate temperature. Observations of the RHEED dynamics show that for growth at a fairly high substrate temperature ($T_s = 470$ °C) the diffraction patterns conserve their linear structure up to a thickness of 60 ML and the surface reconstruction changes from (2×1) to (3×1) (Fig. 1a, RHEED diffraction pattern after deposition of 60 ML). When InAs is deposited at a lower substrate temperature (250 °C), the linear RHEED pattern is converted to a diffraction pattern characteristic of three-dimensional growth (point reflections) even for a thickness of ~ 3 ML and becomes purely bulk after the deposition of 5.5 ML (Fig. 1b, RHEED diffraction pattern after deposition of 6 ML).

Figures 2a, 2b, and 3 show STM images of the InAs/Si surfaces corresponding to these RHEED patterns for high- and low-temperature deposition. During growth at high T_s, the layer modulation reveals two types of morphological characteristics: a corrugated structure ~ 3 nm high with a characteristic period of ~ 25 nm and density $\sim 10^{10}$ cm^{-2}, shown in Fig. 2a, and crystal clusters ~ 400 nm in diameter and ~ 130 nm high with a period of $\sim 5\times10^7$ cm^{-2}, shown in Fig. 2b. A different situation is observed when the sample temperature is reduced to 250 °C. At this temperature a spatially uniform block of quantum dots is formed (Fig. 3). An analysis of cross sections of the STM images reveals that the characteristic lateral dimension of the islands is ~ 12 nm, the height is ~ 4 nm, and the density $\sim 5\times10^{11}$ cm^{-2}.

The difference in the surface morphology observed at different sample temperatures may be attributed first to changes in the surface free energy of the system and thus to a transition from the formation of coherent three-dimensional islands in the nanometer range to mesoscopic three-dimensional clusters[4] at the surface of the corrugated wetting layer. A second factor is that the sticking probabilities of InAs on the Si(100) surface differ at different temperatures. From our point of view, the first explanation is more accurate which is confirmed by the almost equal volume of indium arsenide adsorbed on the silicon surface and the total quantity of deposited InAs.

This analysis suggests that in an InAs/Si system the growth process obeys a Stranski-Krastanow mechanism with a two-dimensional pseudomorphic wetting layer formed initially. Then, at lower deposition temperatures, after a certain critical thickness has been reached (estimated by us as 3 ML at $T_s = 250$ °C), the elastically strained layer undergoes a morphological transformation to give a block of three-dimensional quantum dots. At higher T_s after a corrugated wetting layer has formed, the excess InAs collects into widely spaced mesoscopic clusters as a result of Lifshitz–Slezov coalescence.[5] The RHEED pattern remains linear because of the low cluster density (the coherence length of the electrons along the surface is of the order of a few angstrom).

These results indicate that InAs quantum dots may be formed on Si with dimensions satisfying the conditions for localization of the electron wave function in the direct InAs minimum. It has been shown that heteroepitaxial growth in an InAs/Si system takes place by the Stranski–Krastanow mechanism and the surface morphology depends strongly on the substrate temperature.

To conclude, the authors thank N. K. Polyakov, V. N. Demidov, and N. P. Korneev for assistance with the growth experiments and analysis of the results.

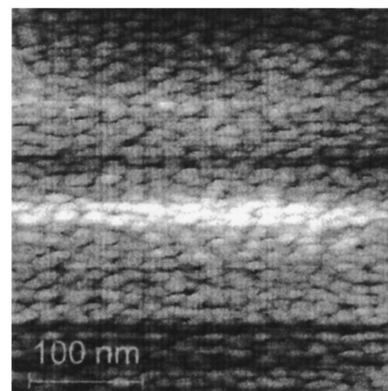

FIG. 3.

This work was partially supported by INTAS (Grant No. 96-0242) and by the Scientific Program ''Physics of Solid-State Nanostructures.''

[1] N. N. Ledentsov, in *Proceedings of the 23rd International Conference on Physics of Semiconductors*, Berlin, 1996, Vol. 1, edited by M. Scheffler and R. Zimmermann (World Scientific, Singapore, 1996), p. 19.
[2] A. Ishisaka and Y. Shiraki, J. Electrochem. Soc. **133**, 666 (1986).
[3] G. M. Gur'yanov, V. N. Demidov, N. P. Korneeva, V. N. Petrov, Yu. B. Samsonenko, and G. É. Tsyrlin, Zh. Tekh. Fiz. **67**(8) 111 (1997) [Tech. Phys. **67**, 956 (1997)].
[4] V. A. Shchukin, N. N. Ledentsov, P. S. Kop'ev, and D. Bimberg, Phys. Rev. Lett. **75**, 2968 (1995).
[5] S. A. Kukushkin, and A. V. Osipov, Prog. Surf. Sci. **51**, 1 (1996).

Translated by R. M. Durham

Operating temperature of single-electron transistors

I. I. Abramov, I. A. Goncharenko, and E. G. Novik

Belarus State University of Informatics and Radioelectronics, Minsk
(Submitted November 25, 1997)
Pis'ma Zh. Tekh. Fiz. **24**, 16–19 (April 26, 1998)

A modified approach is described to estimate the operating temperature of single-electron transistors which gives calculations in satisfactory agreement with the experimental data.
© *1998 American Institute of Physics.* [S1063-7850(98)01804-7]

Structures based on the single-electron tunneling effect have formed the subject of intensive theoretical and experimental research.[1] A promising device of this type is the single-electron transistor. One of the main tasks involved in its development is to estimate the operating temperature, since this depends strongly on the dimensions of the structure.

We are familiar with an approach[2] in which the operating temperature can be estimated as a function of the physical geometry and dimensions of the structure. This approach uses two different models of the device: the first assumes a planar configuration and the second a spherical configuration. The capacitances of the tunnel junctions are thus calculated using well-known relations for planar and spherical capacitors. The conductance of the junctions is determined using the Simmons model[3] for the simplest case of rectangular potential barriers. Thus, simplified models are used in Ref. 2 which lead to errors in estimates of the operating temperature of a single-electron transistor.

In addition, various parameters are introduced (we shall call these ''indeterminacy parameters'') whose numerical values are selected fairly arbitrarily. These shortcomings are clearly the main reason for the pessimistic estimates of the operating temperature of a single-electron transistor.[2] In comparison, the experimental data appear far more promising.[4–6]

Here we attempt to eliminate these shortcomings in estimates of the operating temperature of a single-electron transistor. To this end we used more accurate models to calculate the capacitance and conductance of the tunnel junctions. We briefly describe these modifications.

Calculations of the capacitance C of the junctions were made taking into account the potential distribution not only in the dielectric layer but also at the metal electrodes[7]

$$C=\left(\frac{s}{\varepsilon_d A}+\frac{2.3L}{\varepsilon_m A}\right)^{-1}, \tag{1}$$

where ε_d and ε_m are the permittivity of the dielectric and the electrode material, respectively, s is the thickness of the dielectric, L is the characteristic depth of penetration of the electric field in the metal, and A is the area of the tunnel junction.

The conductance of the junctions was calculated using a hyperbolic approximation of the potential barrier[3] which more accurately describes the real situation, i.e.:

$$\phi(x)=\phi_s-1.15\times\frac{\lambda s^2}{x(s-x)};\quad \lambda=\frac{e^2\ln 2}{8\pi\varepsilon_d s}, \tag{2}$$

where ϕ_s and x are the barrier parameters and e is the electron charge.

The third modification[2] is as follows. Instead of fixed numerical values of the ''indeterminacy parameters,'' we investigated the range of possible variation of these parameters. Two such parameters are used in Ref. 2.

The parameter ξ determines the effective conductance of the tunnel junctions:

$$G=\frac{4e^2}{\xi h}, \tag{3}$$

where h is Planck's constant. For this we investigated the following range of variation $\xi\in[4;10]$. The lower limit (minimum ξ) is selected on the basis of the constraint imposed on the resistance of the tunnel junction, that it should exceed the quantum resistance $he^{-2}\approx 25.8$ kΩ (Ref. 8). The upper limit (maximum ξ) $\xi=10$ is based on data given in Ref. 9.

The second ''indeterminacy parameter'' η is used to calculate the operating temperature of the single-electron transistor:

$$T_{op}=\frac{T_0}{\eta}, \tag{4}$$

where T_0 is the temperature above which thermal fluctuations suppress the single-electron tunneling effect calculated as in Ref. 2. Similar indeterminacies arise in the definition of η and thus we investigated the same range: $\eta\in[4;10]$.

Within the limits of Ref. 2 and using these modifications, we calculated the maximum operating temperature of a single-electron transistor as a function of the radius r_0 of the conducting ''island'' of the transistor (Fig. 1) using the NANODEV program package for modeling nanoelectronic devices.[10] The calculations were made using a spherical model of the device, Curve *1* gives the calculations made according to Ref. 2 in which both parameters are 10. Curve *2* was calculated using the modifications introduced for $\xi=10$ and $\eta=4$. It can be seen that the second curve shows

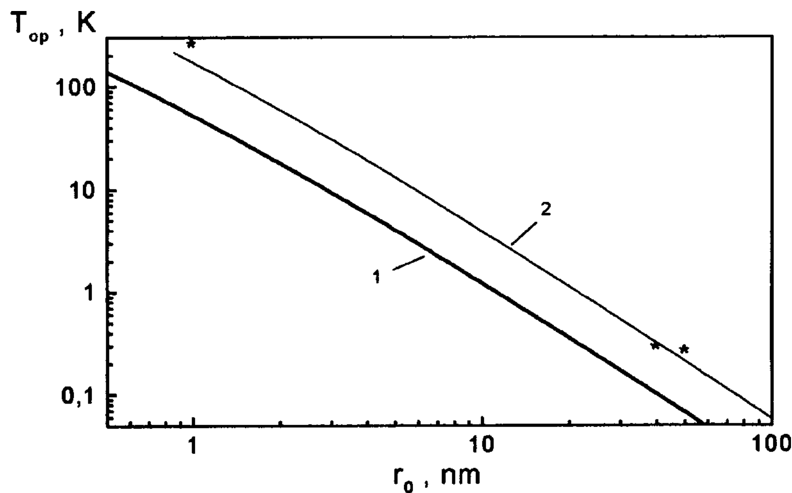

FIG. 1. Operating temperature versus radius of conducting island: *1*—results of calculations as in Ref. 2, *2*—results of calculations using modified approach; *—experimental data.

reasonable agreement with the experimental data.[4–6] Note that curve *2* gives the best agreement with the experiment from the ranges of ξ and η values studied.

To sum up, the modifications introduced in the well-known estimate of the operating temperature of a single-electron transistor can give satisfactory agreement with the experiment for the following different values of the ''indeterminacy parameters'' $\xi=10$, $\eta=4$.

This work was partially financed by the Republican Inter-University Program for Fundamental Research in the Natural Sciences ''Physical Principles of the Fabrication, Diagnostics, Functioning, and Application of Low-Dimension Elements and Systems,'' Grant No. 04.04.

[1] *Single Charge Tunneling: Coulomb Blockade Phenomena in Nanostructures*, edited by H. Grabert and M. Devoret, NATO ASI Ser. B: Physics. Vol. 294 (Plenum Press, New York, 1992).
[2] M. I. Lutwyche and Y. Wada, J. Appl. Phys. **75**, 3654 (1994).
[3] J. G. Simmons, J. Appl. Phys. **34**, 1793 (1963).
[4] E. S. Soldatov, V. V. Khanin *et al.*, JETP Lett. **64**, 556 (1996).
[5] M. Götz, K. Blüthner, W. Krech *et al.*, J. Appl. Phys. **78**, 5499 (1995).
[6] D. Ali and H. Ahmed, Appl. Phys. Lett. **64**, 2119 (1994).
[7] H. Y. Ku and F. G. Ullman, J. Appl. Phys. **35**, 265 (1964).
[8] D. V. Averin and K. K. Likharev, J. Low Temp. Phys. **62**, 345 (1986).
[9] T. A. Fulton and G. J. Dolan, Phys. Rev. Lett. **59**, 109 (1987).
[10] E. G. Novik, I. V. Sheremet, S. S. Ivashkevich, and I. I. Abramov, *Physics, Chemistry, and Application of Nanostructures* (World Scientific, Singapore, 1997) pp. 317–321.

Translated by R. M. Durham

"Ecological" transformer-type plasmatron

É. B. Kulumbaev and V. M. Lelevkin

Kyrgyz-Russian (Slavonic) University, Bishkek

(Submitted November 25, 1997)
Pis'ma Zh. Tekh. Fiz. **24**, 20–24 (April 26, 1998)

A mathematical model of a transformer-type induction toroidal discharge is used to determine the gas flow pattern in the cross section of a circular torus. A method of pumping and heating the injected cold gas transverse to the circular axis is proposed. It is concluded that an "ecological" transformer-type plasmatron may be produced. © *1998 American Institute of Physics.* [S1063-7850(98)01904-1]

An "ecological" plasmatron to reprocess harmful gases at high temperature should provide a convenient gas intake, intensive heating, and dissociation of the gas into its constituent components, followed by efficient quenching of these dissociation products. Pumping of the gas through the high-temperature region of the gas discharge imposes the most difficult constraint on the structure.

A method of exciting a low-frequency discharge has been implemented in a device called a transformer plasmatron,[1] where an electrodeless plasma is sustained by the Joule heat evolved from closed induction currents which form a secondary winding coupled to the primary winding by a magnetic circuit. Studies[2–5] have shown that transformer-type induction discharges have various advantages in different fields of plasma application: these include the production of a spectrally pure plasma, an almost unlimited life, and the advantage of a simple supply source compared with sources of electrodeless discharges in rf and microwave devices.[1] It has been established experimentally[5] that at pressures up to 0.2–0.3 atm, the discharge burns stably and fills almost the entire cross section of the discharge chamber. With increasing pressure, radial oscillations appear and longitudinal vortex pumping of the gas is used to stabilize the discharge.

Here, a mathematical model of a transformer-type induction toroidal discharge is used to determine the gas flow pattern under the action of electromagnetic and gravitational forces in a circular torus without forced azimuthal blowing of the gas. The gasdynamic flow structure obtained in the cross section of the circular torus showed that an ecological plasmatron may be developed using this type of discharge.

We consider an induction discharge in a circular torus encompassing a magnetic circuit with a harmonic magnetic flux (Fig. 1). The plasma state of the gas is sustained by the release of Joule heat from circular induction currents. The characteristics of the transformer discharge are described using a two-temperature magnetogasdynamic approximation of the plasma based on the Navier-Stokes equation, the equations of continuity and energy for the electron gas and the heavy particle gas, quasi-steady-state Maxwell equations, the quasineutrality condition, Ohm's law, and Dalton's law. A solution is obtained using a finite-difference method. The convergence and uniqueness of the solution is confirmed by a numerical simulation using different meshes.

By way of example, we calculate the characteristics of a transformer-type toroidal induction discharge in argon at a pressure of 7 kPa, current of 200 A, and electromagnetic field frequency of 10 kHz using experimental data from Ref. 5. The discharge burns in a circular toroidal chamber with an axial perimeter of 230 cm and a cross-sectional radius of 3.65 cm.

The results are plotted in Fig. 2. It can be seen that the plasma is thermally nonequilibrium over the entire cross section of the discharge chamber. The maxima of the electron and heavy particle temperatures (8220 K and 5230 K, respectively) are shifted toward the center of curvature of the torus axis (Fig. 2a). The calculated secondary voltage of 140 V agrees with the experimental value of 148 V (Ref. 5). In the discharge chamber two toroidal vortices form under the action of the Ampere and Archimedes forces (Fig. 2a). The direction of plasma flow in the central region depends on the ratio between the acting forces. At a discharge current of 200 A electromagnetic forces predominate and at the center of the torus the plasma flows away from the center of curvature of the torus at a maximum velocity of ~ 12 cm/s. At a pressure of 7 kPa the gasdynamic characteristics have a negligible influence on the thermal and electromagnetic parameters of the discharge.

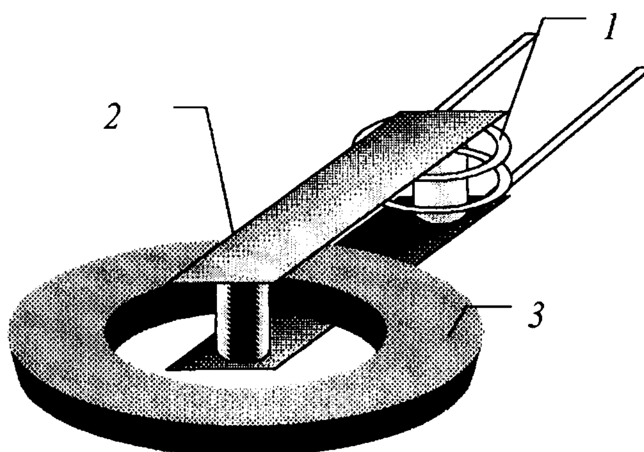

FIG. 1. Schematic of transformer plasmatron: *1*—primary winding, *2*—magnetic circuit, and *3*—discharge chamber.

 © 1998 American Institute of Physics

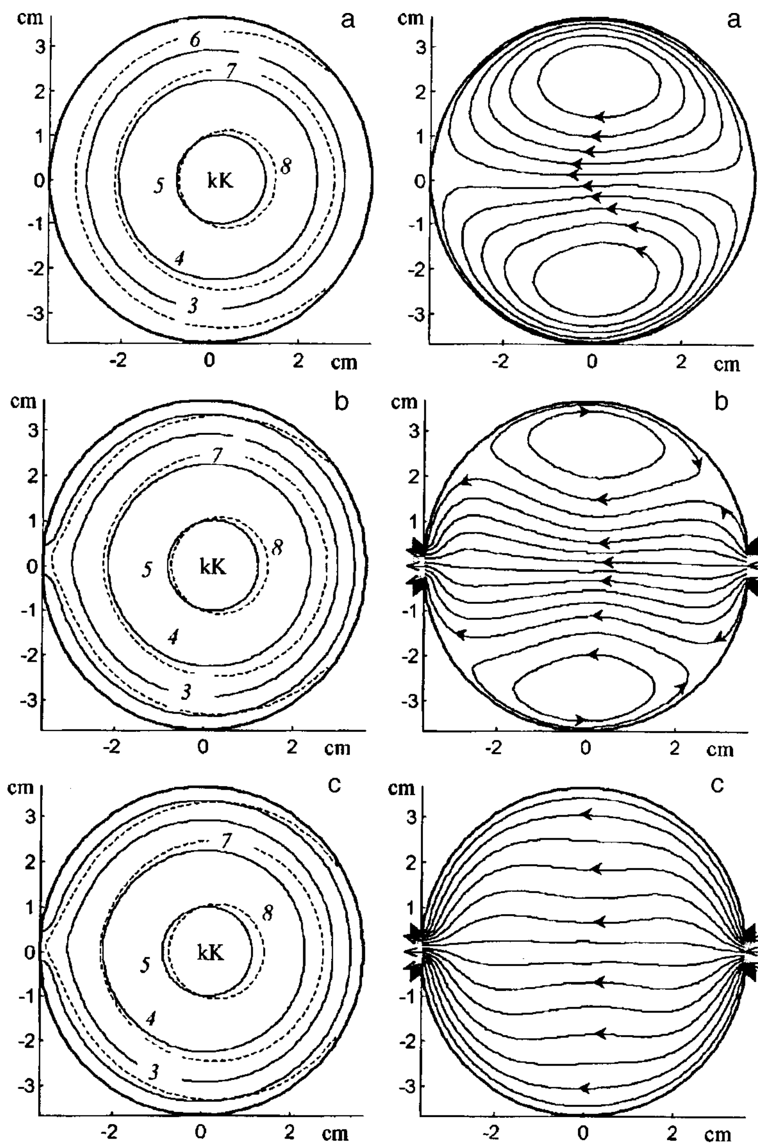

FIG. 2. Temperature fields of electrons (dashed lines) and heavy particles (solid lines) and gas flow lines (vectors) in a toroidal discharge at a pressure of 7 kPa and current of 200 A as a function of the rate of radial blowing of the cold gas: 0 (a), 1 (b), and 10 (c) cm/s.

This flow pattern suggests a method of pumping the gas through the discharge transverse to the torus axis. To achieve this, the gas must be admitted and extracted through diametrically opposed annular slits or systems of apertures in the wall of the toroidal chamber. To determine the gasdynamic structure of a discharge with transverse pumping, calculations were made as a function of the rate of radial blowing of the gas through an annular slit 7.5 mm high (variant 1—1 cm/s and variant 2—10 cm/s). It can be seen (Fig. 2b) that in the first case, the vortex nature of the flow in the torus is conserved. The expansion caused by heating of the cold injected gas reduces the area of the toroidal vortices which impede the tangential flow of the injected gas over the walls of the chamber and ensures that all the gas flows through the high-temperature region. When the gas blowing rate is increased ten times (Fig. 2c), a vortex flow structure does not form. In both cases, the thermal and electromagnetic parameters of the discharge were almost the same.

These results have shown that for conditions of transverse gas pumping exist for which all the injected gas flows through the high-temperature region of the discharge. This indicates that it is possible to develop an ecological transformer-type plasmatron. By selecting the external parameters and optimizing the operating conditions of the plasmatron, toxic chemical compounds can be dissociated by intense heating in the discharge region and the gas can be quenched after being extracted from the apertures in the torus to produce ecologically pure gases.

[1] S. V. Dresvin, A. A. Bobrov, V. M. Lelevkin *et al.*, *Rf and Microwave Plasmatrons* [in Russian], Nauka, Novosibirsk (1992).
[2] H. U. Eckert, AIAA J. **9**, 1456 (1971).
[3] N. N. Rykalin, I. D. Kulagin, A. V. Nikolaev *et al.*, Fiz. Khim. Obrab. Mater. **No. 4**, 155 (1977).
[4] V. M. Gol'dfarb, A. V. Donskoĭ, S. V. Dresvin *et al.*, Teplofiz. Vys. Temp. **17**, 698 (1979).
[5] V. A. Kogan and I. M. Ulanov, Teplofiz. Vys. Temp. **31**, 105 (1993).

Translated by R. M. Durham

Dichroic optically bistable cavity-free system

O. S. Bondarenko and V. A. Trofimov

M. V. Lomonosov State University, Moscow
(Submitted November 18, 1997)
Pis'ma Zh. Tekh. Fiz. **24**, 25–32 (April 26, 1998)

A description is given of a possible method for the practical observation of optical bistability of a cavity-free system. © *1998 American Institute of Physics.* [S1063-7850(98)02004-7]

Optical bistability has attracted the interest of many researchers over the years because of the possibility of using this effect to construct optical memory elements, information processing and storage systems, and also optical computers.[1–3] Even greater interest was shown in this effect because of the imminent prospect of developing optical Winchester disks.[4] However, the search for new methods of recording information, improving the switching speed of optically bistable systems, and reducing the energy consumption per switching event remains as topical as ever. In this context, the authors of Refs. 5–7 investigated how the temperature dependence of the free carrier relaxation time of the semiconductor influences the establishment of absorption optical bistability. In addition to the observed complex propagation dynamics of the switching waves (the establishment of different space-time structures and loss of stability of initially stable states of the system), these investigations revealed that bistability may achieved as a result of a nonlinear dependence of the free carrier relaxation time on temperature (not only the lattice temperature but possibly also the electron temperature) without using nonlinear absorption. This poses the problem of observing this effect in practice from the characteristics of optical radiation transmitted by a nonlinear medium. A possible method of observing this effect is described here.

This method essentially involves laser beams at different

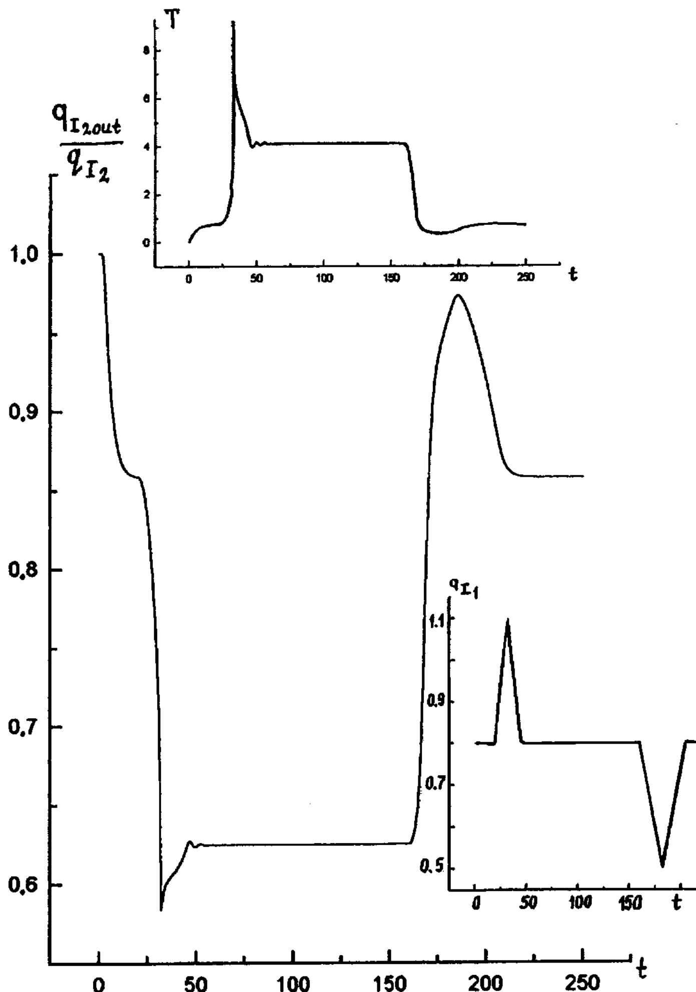

FIG. 1. Dynamics of switching of an optically bistable system to the upper (positive pulse) and lower (negative pulse) states for an illuminating signal $q_{I_1}=0.8$.

 © 1998 American Institute of Physics

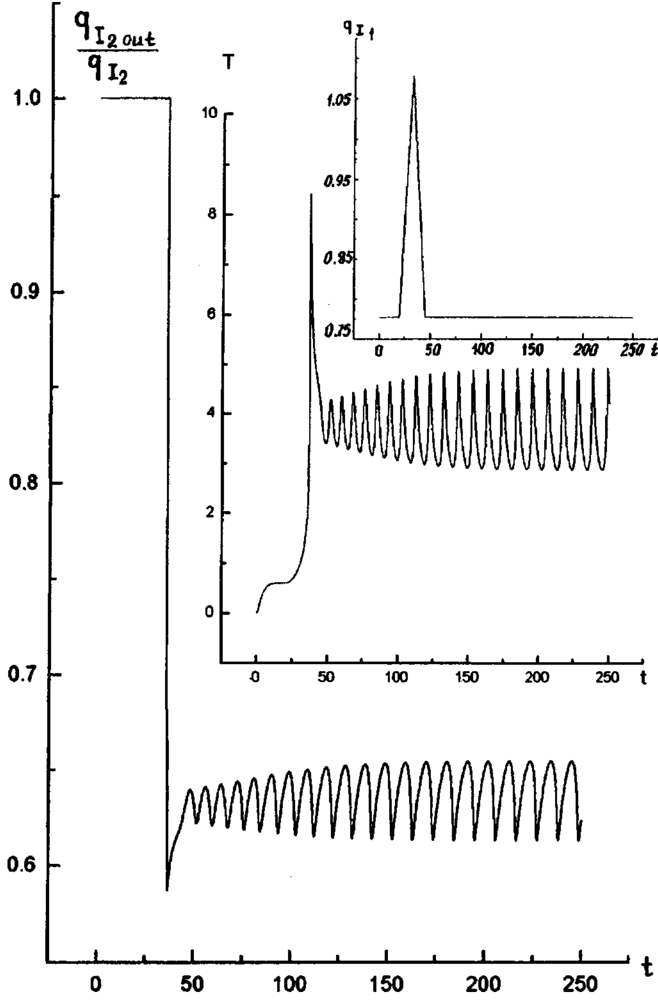

FIG. 2. Recording of temperature self-oscillations from the output radiation of the probe signal for $q_{I_1}=0.777$ during switching of an optically bistable system to the upper state.

frequencies acting on a semiconductor: one beam (the main beam) is used to maintain the system near the switching state. A second (probe) beam is used to record the switching of the optically bistable system from one state to another which may be caused by physical factors: by nonlinear absorption, refraction, or polarization reversal. Here we shall assume that this switching is the result of a nonlinear change in the absorption of the medium. Thus, the frequency of the probe beam lies near the absorption edge. The main does not undergo nonlinear absorption, i.e., its frequency exceeds the corresponding transition energy. In this case, the interaction between the optical radiation and the semiconductor is described by the following system of dimensionless equations using the point model widely used for qualitative analyses of operation in an optically bistable system:[1–3]

$$\frac{\partial n}{\partial t}=q_{I_1}+q_{I_2}\delta(n,T)-n\left(\frac{1}{\tau_r(T)}+\frac{1}{\tau_D}\right),$$

$$\frac{\partial T}{\partial t}=q\frac{n}{\tau_r(T)}-T, \tag{1}$$

with the boundary and initial conditions

$$n|_{t=0}=\tilde{n}_0,\quad T|_{t=0}=\tilde{T}_0. \tag{2}$$

In Eqs. (1) and (2) q_{I_1} and q_{I_2} characterize the intensities of the main and probe pulses, respectively, n is the change in the concentration of free carriers relative to its equilibrium value at the initial temperature, T is the change in the temperature of the semiconductor relative to the ambient temperature, t is the time normalized to the characteristic heat transfer time, $\tau_r(T)$ is the nonradiative recombination time, the time τ_D allows for the transverse diffusion of free charges and radiative recombination, q is the heat released as a result of nonradiative recombination, and $\delta(n,T)$ is the nonlinear dependence of the energy absorption coefficient of the signal beam. This dependence and the free carrier relaxation time were approximated by the functions

$$\delta(n,T)=\begin{Bmatrix}0, & T<T_S\\ \exp(-1/(T-T_S+T_0)), & T\geqslant T_S\end{Bmatrix},$$

$$\tau_r(T)=\tau_{rm}\exp(-T/\beta), \tag{3}$$

where τ_{rm} depends on the initial temperature of the semiconductor and β characterizes the rate of change in the relaxation time with increasing temperature (this parameter is subsequently taken to be 1). Note that different dependences $\tau_r(T)$ and values of the parameter β did not fundamentally alter the results. In addition, T_0 is the temperature of the ambient medium and T_S is a parameter which allows for the detuning of the probe beam frequency from the absorption edge. For convenience of comparing the results with the case of absorption optical bistability, the temperature is normalized to the band gap which is expressed in the same units. It is known[3] that absorption optical bistability is achieved if the value of the parameter T_0 is less than 0.25 (for $T_S=0$).

For the first beam, a triangular signal is applied against a background of constant illumination $q_{I_{10}}$

$$q_{I_1}=q_{I_{10}}+q_S\begin{Bmatrix}(t_c-t)/(t_c-t_f), & t_f<t<t_c,\\ (t-t_c)/(t_b-t_c), & t_c<t<t_b\end{Bmatrix}, \tag{4}$$

which transfers the system to the upper ($q_S>0$) or lower ($q_S<0$) state. In Eq. (4) t_f, t_c, and t_b are the pulse switching time, its peak, and its end, respectively. Bistability is recorded from the change in the output intensity of the probe pulse

$$q_{I_{2out}}=q_{I_2}\exp(-\delta_{02}\delta(n,T)), \tag{5}$$

where the dimensionless coefficient δ_{02} allows for the optical absorption over the length of the medium.

We examine the laws described below for the following set of parameters:

$$\tau_D=2.0,\ \tau_{rm}=20,\ q=5,\ \delta_{02}=0.6,$$

$$q_{I_2}=0.2,\ \tilde{n}=\tilde{T}=0,\ T_S=T_0=2,$$

$$q_S=\pm 0.3,\ t_f=20,\ t_b=45,\ t_{c\uparrow}=22.5,\ t_{c\downarrow}=182.5, \tag{6}$$

where $t_{c\uparrow}$ and $t_{c\downarrow}$ are the times corresponding to the centers of the pulses which transfer the system from the lower to the upper state and vice versa. The intensity of the main signal $q_{I_{10}}$ was selected from the condition that either a stable or an

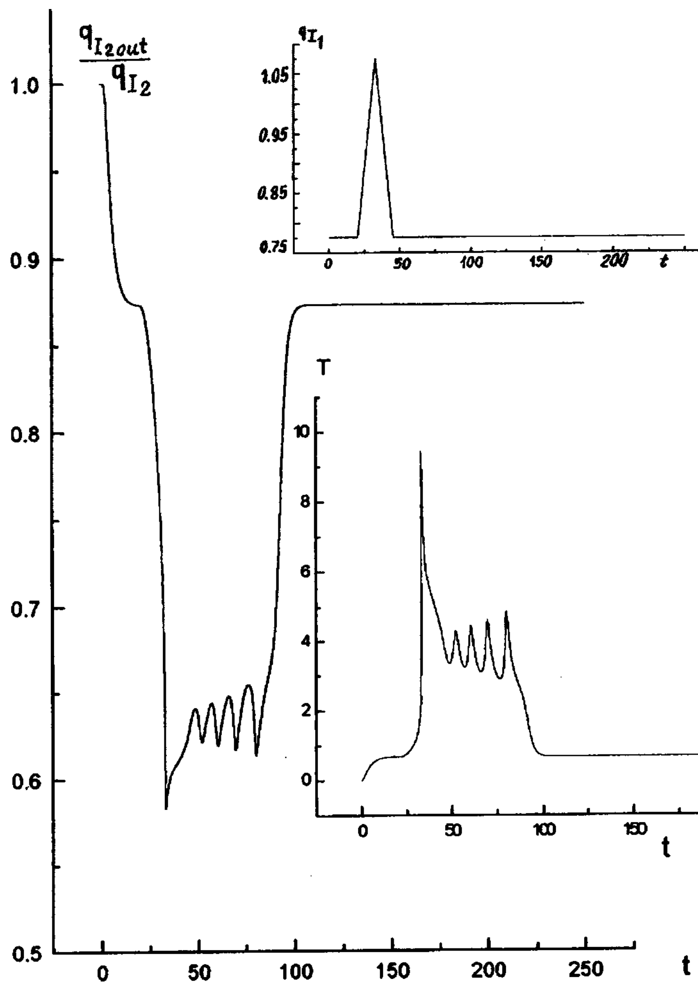

FIG. 3. Self-switching of an optically bistable system from the upper to the lower state as a result of instability of the upper state for $q_{I_1}=0.776$.

unstable upper state of the bistable system is achieved. The results which illustrate three behavior modes of an optically bistable system are plotted in Figs. 1–3, which give the dynamics of variation of the output intensity of the signal pulse relative to its value on entry to the nonlinear medium, the evolution of the temperature of the medium, and the shape of the main pulse. The figures are plotted for different intensities of the illuminating pulse on which the stability of the upper state of the optically bistable system depends. Note that switching of the system from one state to the other (Fig. 1) takes place even for $T_0=4$ and higher values. In order to observe contrast switching from the output radiation of the probe beam, it is desirable to select its frequency such that at this temperature the optical frequency would be far from the absorption edge (this is described by the parameter T_S).

When the temperature falls within the range where oscillations develop after the system has been switched to the upper state (Fig. 2), the optical probe pulse will undergo oscillations whose amplitude, other conditions being equal, is determined by the frequency detuning from the fundamental absorption edge.

If the amplitude of the illuminating beam is such that after the system has been switched from the lower to the upper state (Fig. 3), it falls within the instability range (the amplitude of the oscillations increases), with time the amplitude of the temperature oscillations may reach a level sufficient for self-switching of the system from the upper to the lower state. In this case, after a transient oscillatory regime, the output intensity of the probe beam reaches a level corresponding to the lower steady-state temperature of the medium.

To sum up, the previously observed bistability based on the nonlinear temperature dependence of the free carrier relaxation time, and also the instability of the upper state of an optically bistable system may be effectively achieved by the action of two light beams of different frequency. Similar laws will also be obtained for the nonlinear dependence of the relaxation time on the electron temperature and the nonlinear dependence of the excited-state relaxation time on the vibrational temperature of the molecules.

This work was partially financed by the Russian Fund for Fundamental Research (Grant No. 95-02-04448).

[1] H. M. Gibbs, *Optical Bistability: Controlling Light with Light* (Academic Press, Orlando, 1985; Mir, Moscow, 1988, 518 pp.).
[2] *Optical Computing, Digital and Symbolic*, edited by R. Arrathoon (Dekker, New York, 1989; Mir, Moscow, 1993, 441 pp.).
[3] N. N. Rozanov, *Optical Bistability and Hysteresis in Distributed Nonlinear Systems* [in Russian], Nauka, Moscow (1997), 334 pp.
[4] Proceedings of the International Conference on *Optical Information, Science and Technology, OIST-9,* Moscow, 1997.

[5] Yu. N. Karamzin, S. V. Polyakov, V. A. Trofimov, Pis'ma Zh. Tekh. Fiz. **18**(24), 38 (1992) [Sov. Tech. Phys. Lett. **18**, 809 (1992)].
[6] V. A. Trofimov and O. C. Bondarenko, Abstracts of Papers presented at NLMI-9. St. Petersburg, 1996, p. 108.
[7] O. S. Bondarenko, V. A. Trofimov *et al.*, BRAS Phys. **59**, Suppl. Phys. Vibrat. No. 1, 21 (1995).

Translated by R. M. Durham

Numerical simulation of laminar flow round a cylinder with passive and active vortex cells

P. A. Baranov, S. A. Isaev, Yu. S. Prigorodov, and A. G. Sudakov

Academy of Civil Aviation, St. Petersburg
(Submitted November 12, 1997)
Pis'ma Zh. Tekh. Fiz. **24**, 33–41 (April 26, 1998)

Effects involving a reduction in the drag coefficient of a cylinder with passive and active vortex cells of different geometry are analyzed by solving the Navier-Stokes equations by a factorized finite-volume method using the concept of decomposition of the calculation region and using multilevel meshes. © *1998 American Institute of Physics.* [S1063-7850(98)02104-1]

The search for rational methods of controlling the flow round blunt objects designed to give future aircraft an aerodynamic appearance has stimulated research into the synthesis of well-known combinations of inblowing and extraction with the formation of organized vortex wall flows using vortex cells. In principle, the use of active (with supply or removal of fluid) and passive vortex cells can produce smooth continuous flow around an object and substantially improve its characteristics.

For some time the control of flow round blunt objects using inblowing and extraction of the flow has been an attractive problem in aerohydrodynamics. Well-known methods include controlling the boundary layer on a wing by extraction of the flow, reducing the base drag of objects by gas inblowing, and blowing out jets ahead of an object to reduce its drag coefficient. However, it is sometimes difficult to estimate the efficiency of these devices because of the complexity of allowing for the energy dissipated in the inblowing/extraction process. However, the use of passive (without energy consumption) methods of controlling flow using protuberances, and permeable and impermeable barriers can also substantially improve their aerodynamic characteristics by organizing large-scale vortex structures around these objects. In particular, the creation of vortex cells or traps of extremely intense vortices in front of objects can reduce the profile drag of a blunt object by one or two orders of magnitude.[1]

It is advisable to combine these methods of influencing the flow round objects and to undertake a complex optimization of the flow control process based on the criterion of minimizing the drag of the objects. It should be noted that this fundamental problem is highly topical in terms of content and procedure and the results will be useful to verify prospective aircraft designs.

Here numerical simulation methods are used for the first time to formulate and solve a conjugate problem involving the influence of trapped large-scale vortex structures on the laminar flow of a stream of incompressible viscous fluid and on the aerodynamic drag of an object having a classical geometry—a circular cylinder—in the presence of passive and active vortex cells of different shape and occupying different positions relative to the center of the cylinder. The vortex cells under study are elliptical with a central body of the same geometry. This approach can be used to construct an algorithm based on a finite-volume method of solving the Navier-Stokes equations using the well-known concept of decomposition of the calculation region by generating multilevel overlapping oblique-angled meshes of the same type (O-type) in selected subregions of widely differing scale. The system of initial equations is written in divergent form for the increments of the dependent variables: the contravariant components of velocity and pressure. This approach is similar to that used in Ref. 2 and gives a more accurate representation of the flows across the faces of the calculation cells.

The proposed calculation model is based on the concept of splitting into physical processes, used in the SIMPLEC pressure correction procedure. Characteristic features of this iteration algorithm include the determination of preliminary velocity components for the ''frozen'' pressure fields at the ''predictor'' step, and subsequent correction of the pressure based on solving the equation of continuity with velocity field corrections. The computation process is constructed so that one predictor step covers several iteration steps in the pressure calculation block. We use a method of global iterations over subregions, followed by interpolation of the dependent variables in the zones of overlap of the subregions.

A centered template with the dependent variables positioned at the center of the calculation cell is selected to simplify the calculation algorithm and reduce the number of computational steps. In this approach the pressure field is monotonized using the Rkhi-Chou method. A highly stable calculation procedure is achieved by using unilateral counterflow differences to discretize the convective terms on the implicit side of the equations for increments of the unknown variables, by damping nonphysical oscillations by introducing artificial diffusion on the implicit side of the equations, and by using pseudotime stabilizing terms. The Stones version (SIP) of a method of incomplete factorization to solve systems of nonlinear algebraic equations also enhances the computation efficiency of the calculation algorithm. The accuracy of the procedure is made acceptable by discretizing the explicit side of the equations using a second-order approximation scheme and in particular, the convective terms

 © 1998 American Institute of Physics

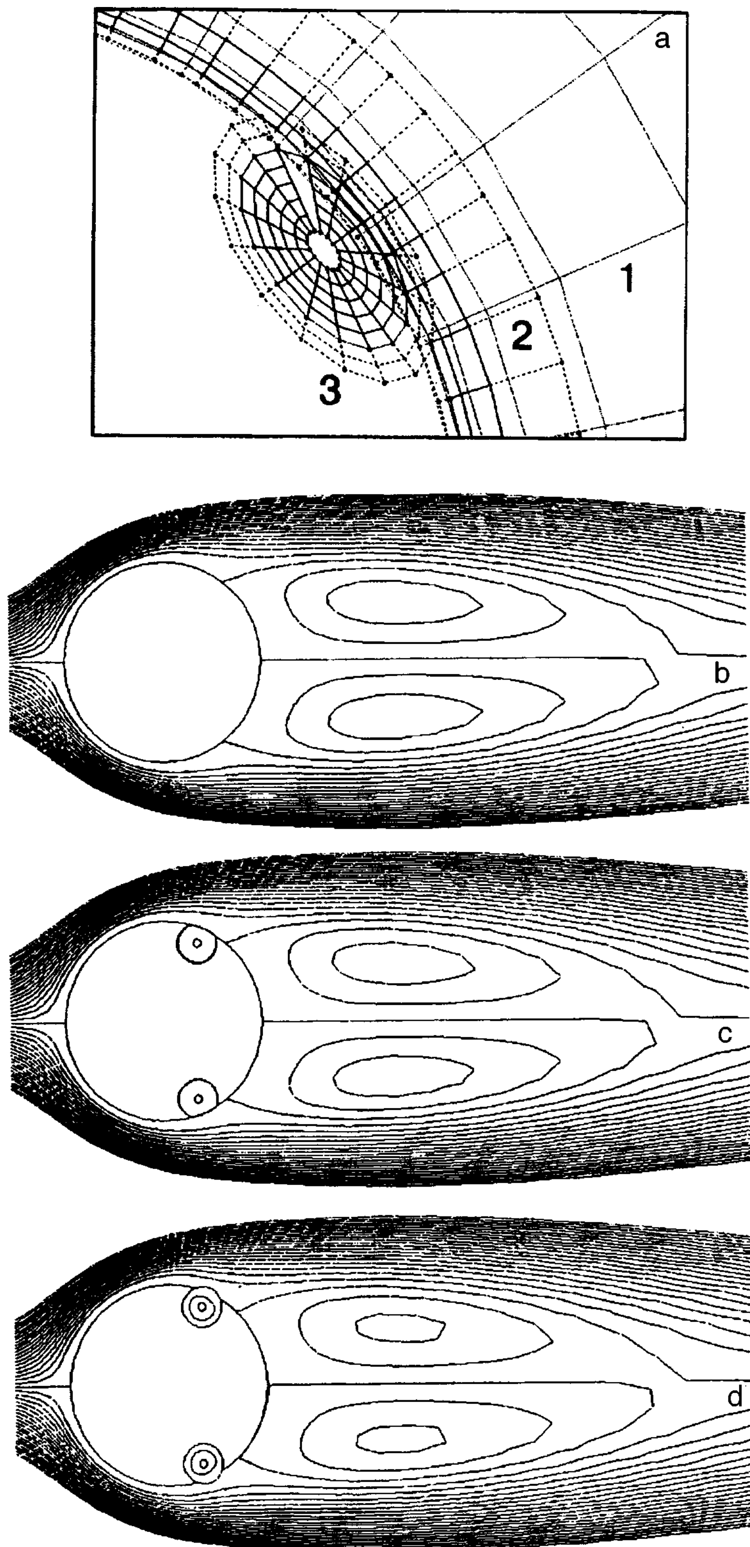

FIG. 1. Fragment of a composite mesh (a) consisting of a two-level (1, 2) mesh around the cylinder and a mesh in the vortex cell (3), flow pattern around a cylinder without a cell (b), with a passive circular cell (c) of diameter 0.2 with a circular central body of diameter 0.04, shifted by 0.2 from the center of the cylinder, and with an active cell of the same geometry (d) with a tangential velocity component of 0.3 defined on the surface of the cavity. The flow lines are plotted with a step of 0.0007 between −0.015 and 0.015.

in the equations using the Leonard quadratic counterflow scheme (QUICK). This methodology can minimize the influence of ''numerical'' diffusion effects which are particularly significant for calculations of detached flows. Details of the calculation procedure are given in Ref. 1.

To achieve a more accurate resolution of different-scale structural elements in solutions of this problem of laminar flow around a cylinder with vortex cells for a low Reynolds number Re=40, it is best to separate a wall region whose thickness is approximately 0.1 of the cylinder diameter (taken as the characteristic dimension) and an outer annular zone, whose outer boundary is positioned some distance (of the order of 50–100) from the object. By introducing several annular zones (Fig. 1a) or equivalent, the construction of multilevel meshes can speed up the convergence of the solution by reducing the required number of calculation cells.

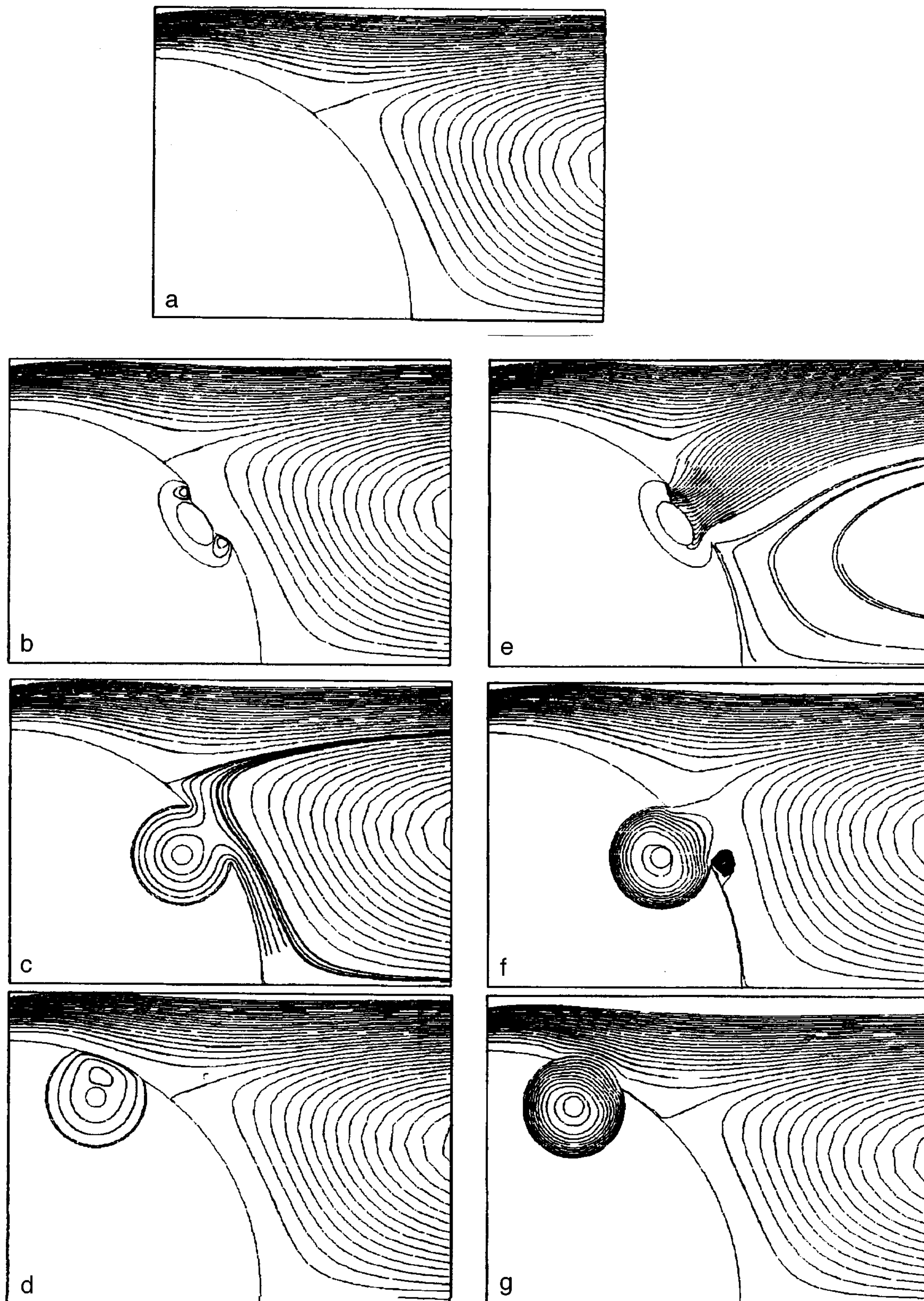

FIG. 2. Fragments of flow round a smooth cylinder (a), a cylinder with passive elliptical (b) and circular (c) cells shifted relative to the center of the cylinder by 0.4, and a circular cell (d) shifted relative to the center of the cylinder by 0.2, and a cylinder with active cells comprising an elliptical cell (e) with normal and tangential blowing rates of 0.1 defined at the surface of the central body, and circular cells (f, g) with a tangential velocity of 0.3 defined on the surface of the cavity. The flow lines are plotted with a step of 0.0001 between -0.002 and 0.002.

We can put forward a constraint on the relative position of the zones: the region of overlap of neighboring zones should include of the order of 3–4 cells of each zone so that the entire region of overlap contains of the order of 6–8 calculation cells. If this constraint is not satisfied and the number of cells is less than this, the process of information transfer between the zones is impaired. If the number of cells in the overlap region is too great, an unjustified overexpenditure of

TABLE I. Comparative analysis of drag coefficients and their components for a cylinder with vortex cells of different shape and configuration for Re=40.

		Passive cells			Active cells		
	Cylinder without cells point	Elliptical beyond separation point	Circular beyond separation point	Circular before separation point	Elliptical beyond separation point	Circular beyond separation point	Circular before separation point
C_v	1.5284	1.5288	1.5279	1.5234	1.3600	1.4775	1.4332
C_{vp}	0.9869	0.9858	0.9851	0.9994	0.4454	0.8442	0.7775
C_{vf}	0.5415	0.5430	0.5428	0.5241	0.9145	0.6333	0.6558
C_{vc}	–	1.3947	1.3946	1.4221	1.4507	1.4153	1.4451
C_{vpc}	–	0.8498	0.8497	0.8945	0.9047	0.8540	0.8877
C_{vfc}	–	0.5448	0.5449	0.5277	0.5460	0.5613	0.5574
C_{vcs}	–	0.0684	0.0670	0.0543	−0.7560	0.0074	−0.0378
C_{vpcs}	–	0.0685	0.0679	0.0549	−0.8295	−0.0201	−0.0751
C_{vfcs}	–	−0.0001	−0.0009	−0.0005	0.0735	0.0275	0.0373
C_{vcb}	–	−0.0014	−0.0003	−0.0037	0.7103	0.0232	0.0318
C_{vpb}	–	−0.0005	−0.0001	−0.0024	0.5995	0.0146	0.0199
C_{vfcb}	–	−0.0008	−0.0001	−0.0013	0.1108	0.0086	0.0117

The subscripts ''v'', ''vp'', and ''vf'' denote the drag coefficient, the pressure drag, and the friction drag for a cylinder with vortex cells, ''c'', ''cs'', and ''cb'' indicate the contributions made to the corresponding drag coefficients by the cylinder, the surface of the vortex cell, and the central body, respectively.

calculation resources is incurred. In this study the number of mesh points in the outer zone is 120×80 and in the wall zone 200×11. The step at the wall is 0.002.

Within the vortex cells the mesh is constructed uniformly over the arc and radius (21 in each direction for these calculations). The number of points at the edge of the cavity is fixed. The total number of points in the direction of the circumference is then calculated from the condition that the angular step is the same. The longitudinal dimension of a vortex cell is taken to be 0.2. The maximum size of the central body for an elliptical cell (semiaxis ratio 2:1) is 0.1. For circular vortex cells the central body has a diameter of 0.04. In all cases, the cells are positioned inside the cylinder recessed to a depth of 15% of the transverse dimension of the cell. Two cell configurations are considered—before and after the separation point of the flow round a smooth cylinder (Fig. 2). The cells are made active by defining the normal and tangential flow velocity at the surfaces of the cavity and the central body. In this study an elliptical cell is made active by inblowing at the central body (the inblowing intensity is defined as 0.1 for both velocity components). Circular cells are made active by defining a tangential flow velocity of 0.3 at the surface of the cavity (twisting of the vortex in the direction of the external flow).

The results plotted in Figs. 1 and 2 and in Table I show that for the selected Reynolds number, passive vortex cells of different sizes and configurations cannot have any significant influence on the flow pattern around a circular cylinder (almost no flow takes place in these cells). Making the cells active by inblowing from the central body leads to the formation of a jet stream from the elliptical cell, redistributes the local loads on the cylinder, and generally reduces the integrated drag. In our view, the conversion of the flow in a circular cell to active is more interesting because of the intensification of the vortex and the transfer of momentum to the external flow. In this case, the position of the vortex cell relative to the separation point has a significant influence on the flow pattern around the cylinder and on the drag coefficient. Placing a circular cell in a zone of higher-intensity flow (Fig. 2g) can reduce the drag of the cylinder to a greater extent.

This work was supported financially by the Russian Fund for Fundamental Research under Projects Nos. 96-01-01290 and 96-01-00298.

[1] I. A. Belov, S. A. Isaev, and V. A. Korobkov, *Problems and Methods of Calculating Detached Flows of an Incompressible Fluid* [in Russian], Sudostroenie, Leningrad (1989), 256 pp.

[2] Yu. E. Karyakin, V. E. Karyakin, and O. G. Martynenko, Preprint No. 1 [in Russian], Institute of Heat and Mass Transfer, Belarus Academy of Sciences, Minsk (1991), 44 pp.

Translated by R. M. Durham

Domain instability in an ensemble of dislocations during plastic deformation of crystals

G. F. Sarafanov

Nizhniĭ Novgorod State Pedagogical University
(Submitted September 2, 1997)
Pis'ma Zh. Tekh. Fiz. **24**, 42–48 (April 26, 1998)

An analysis is made of the nonlinear dynamics of perturbations of the dislocation density and elastic field using a proposed evolution model which takes into account the negative velocity sensitivity of the deforming stresses. As a result of the evolution of domain instability, it is observed that periodic and isolated solutions (solitons) exist for the initial variables.
© *1998 American Institute of Physics.* [S1063-7850(98)02204-6]

In spite of the success achieved in the experimental study of strained solids,[1,2] many of the effects accompanying the plastic deformation process have not yet been explained theoretically. This particularly applies to the plastic flow instability of a crystal.[3–5] Beginning with the studies made by Cottrell,[6] the mechanism for this effect is usually attributed to a nonlinear N-shaped dependence of the stopping force of dislocations on their velocity, caused by the formation of impurity atmospheres (Cottrell, Snoek, and so on) at dislocations.[7–9] It is also possible to have a situation where, in a certain range of stresses, the average velocity of the dislocations does not exhibit an N-shaped dependence on the flow stress σ. In certain cases in solid solutions with plastic deformation of a crystal, moving dislocations can create conditions of stimulated nonlinear diffusion of impurity atoms, which result in efficient interaction and clustering of the impurity atoms. This situation is observed for $\sigma>\sigma_c=[Gn_0T/\rho_0 d^2]^{1/2}$ (Ref. 10) where G is the shear modulus, T is the temperature, n_0 and d are the concentration and characteristic size of the dissolved atoms, and ρ_0 is the average dislocation density. This behavior leads to abrupt hardening of the crystal and reduces the average dislocation velocity V. A further increase in load restores the monotonic behavior of the curve $V(\sigma)$ (Fig. 1). The region $\sigma_c<\sigma<\sigma_m$ characterizes the negative velocity sensitivity of the deforming stresses and is caused by a change in the crystal hardening mechanism.

In view of the possibility of obtaining this type of dependence $V(\sigma)$, we consider a problem associated with abrupt plastic deformation in crystal alloys.

To be specific, we consider a crystal oriented for single glide, which is deformed under active loading. We shall assume that edge dislocations characterized by the densities $\rho_+(x,t)$ and $\rho_-(x,t)$ participate in the evolution of a dislocation ensemble. These dislocations propagate toward each other in parallel glide planes in the x direction at velocities $V_+=V(\sigma)$ and $V_-=-V(\sigma)$, to form a glide band of width L.

With allowance for dislocation generation and annihilation processes, the system of evolution equations for the scalar density $\rho_\pm(x,t)$ is written in the form[5,11]

$$\frac{\partial\rho_\pm}{\partial t}+\frac{\partial}{\partial x}(V_\pm\rho_\pm)=A-\kappa\rho_+\rho_- . \tag{1}$$

Here A is a source of Frank–Read dislocations and κ is the annihilation coefficient.

Under active loading when the average rate of plastic deformation $\dot{\varepsilon}_0$ is kept constant, Eq. (1) must be supplemented by the Gilman-Johnson equation[12]

$$\frac{\partial\sigma}{\partial t}=\frac{KL}{S\zeta}(\dot{\varepsilon}_p-bV_+\rho_+ +bV_-\rho_-), \tag{2}$$

where $\dot{\varepsilon}_p=\eta L_0\dot{\varepsilon}_0/L$ is the rate of plastic deformation in the glide band, K is the rigidity of the ''sample-tester'' system, L_0 and S are the height and cross-sectional area of the sample, η and ζ are geometric factors of the order of unity.

In terms of the variables $\rho=\rho_+ + \rho_-$ and $I=\rho_+ - \rho_-$, which characterize the total and excess dislocation density, the system (1) and (2) has the form

$$\frac{\partial I}{\partial t}+\frac{\partial}{\partial x}(V\rho)=0, \tag{3}$$

$$\frac{\partial\rho}{\partial t}+\frac{\partial}{\partial x}(VI)=2A-\frac{\kappa}{2}(\rho^2-I^2), \tag{4}$$

$$\frac{\partial\sigma}{\partial t}=G^*(\dot{\varepsilon}_p-bV\rho). \tag{5}$$

The fact that the right-hand side of Eq. (3) is zero reflects the fact that the Burgers vector is conserved for different dislocation reactions and multiplication.[5,11] Equations (3) and (5) can be integrated to give

$$\frac{\partial\sigma}{\partial x}=G^*b(I-I_c), \tag{6}$$

where $G^*=KL/S\zeta$ is the effective modulus of elasticity and I_c is the integration constant which has the meaning of the excess dislocation density of the substructure formed by the time the material is deformed (to be specific, we shall assume $I_c=\rho_c^+ - \rho_c^- >0$).

We investigate the stability of the steady state

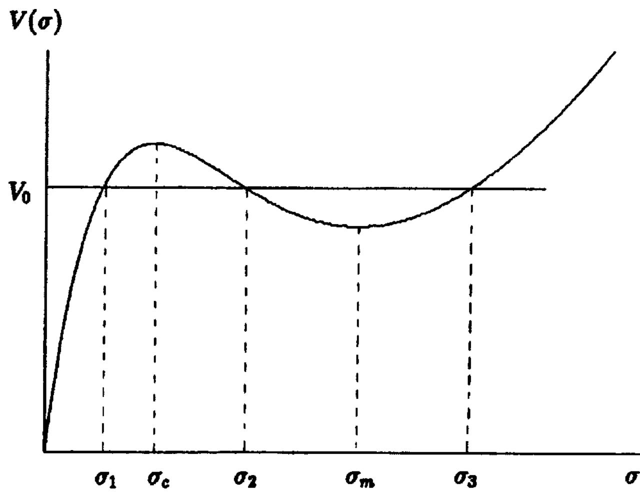

FIG. 1.

$$I=I_c, \quad \rho=\rho_c\sqrt{1+I_c^2/\rho_c^2}=\rho_0,$$

$$V=V_0(\sigma_0)=\eta L_0\dot{\varepsilon}_0/b\rho_0 L \tag{7}$$

of the system (4)–(6). Here we have $\rho_c=2(A/\kappa)^{1/2}$ and $V_0(\sigma_0)$ is triply degenerate since the line $V=V_0$ is assumed to intersect the curve $V(\sigma)$ at three points ($\sigma_0=\{\sigma_1,\sigma_2,\sigma_3\}$) (Fig. 1).

For perturbations of the type $\sim\exp(-i\omega t+ikx)$ the dispersion equation has the form

$$\omega^2+i\omega\frac{1-\alpha}{\tau}-V_0^2k^2-ik\frac{\beta V_0(1+\alpha)}{\tau}+\frac{\alpha}{\tau^2}=0, \tag{8}$$

where $\tau=1/\kappa\rho_0$ is the characteristic interdislocation interaction time, $\alpha=-G^*b\tau\rho_0V'_\sigma(\sigma_0)$ is a dimensionless parameter which characterizes the velocity sensitivity of the deforming stresses, and $\beta=I_c/\rho_0=(1+\rho_c^2/I_c^2)^{-1/2}<1$.

It follows from Eq. (8) that instability ($\mathrm{Im}\,\omega>0$) may be achieved when the velocity sensitivity of the flow stress is negative ($V'_\sigma<0$, $\alpha>0$). We examine in greater detail the case $0<\alpha\ll 1$, which corresponds to the establishment of instability in the range of deforming stresses $\sigma\sim\sigma_c$. In this case, an analysis of the dispersion equation (8) shows that the evolution of the system for $t>\tau$ is determined by the branch

$$\omega_1\simeq\beta V_0k+i\alpha/\tau-iV_0^2\tau k^2, \tag{9}$$

whose type characterizes the so-called Gunn domain instability[13] which is well-known in semiconductor physics. In accordance with expression (9), long-wavelength perturbations propagating to the right with the phase velocity $c_0=\beta V_0<V_0$ increase slowly with the growth rate $\mathrm{Im}\,\omega_1=\alpha/\tau>0$.

Nonlinear solutions of the system (4)–(6) will be sought in a class of self-similar solutions assuming that σ, I, and ρ depend on the traveling coordinate $\xi=x-ct$. Eliminating $I(\xi)$ and $\rho(\xi)$ from these equations, in the approximation under study ($\alpha\ll 1$) we obtain a single second-order nonlinear equation for $\sigma(\xi)$

$$\tau(V_0^2-c^2)\frac{\partial^2\sigma}{\partial\xi^2}+(c_0-c)\frac{\partial\sigma}{\partial\xi}-\frac{V_0}{2G^*b\rho_0}\left(\frac{\partial\sigma}{\partial\xi}\right)^2$$
$$+G^*[\dot{\varepsilon}_p-b\rho_0V(\sigma)]=0. \tag{10}$$

Equation (10) describes a steady-state traveling wave. This has the same form as the equation for a concentrated nonlinear oscillator with damping $\sigma=c_0-c$. Thus, the steady-state solutions of interest to us exist for $c=c_0<V_0$. An analysis of the solutions is best made on the phase plane of the variables σ and σ'_ξ. In the case $\delta=0$ of interest to us, Eq. (10) has three fixed points $(\sigma_1,0)$, $(\sigma_2,0)$, and $(\sigma_3,0)$ on the phase plane (σ,σ'_ξ). The state $(\sigma_2,0)$ is the center and the singular points $(\sigma_1,0)$ and $(\sigma_3,0)$ are the saddles

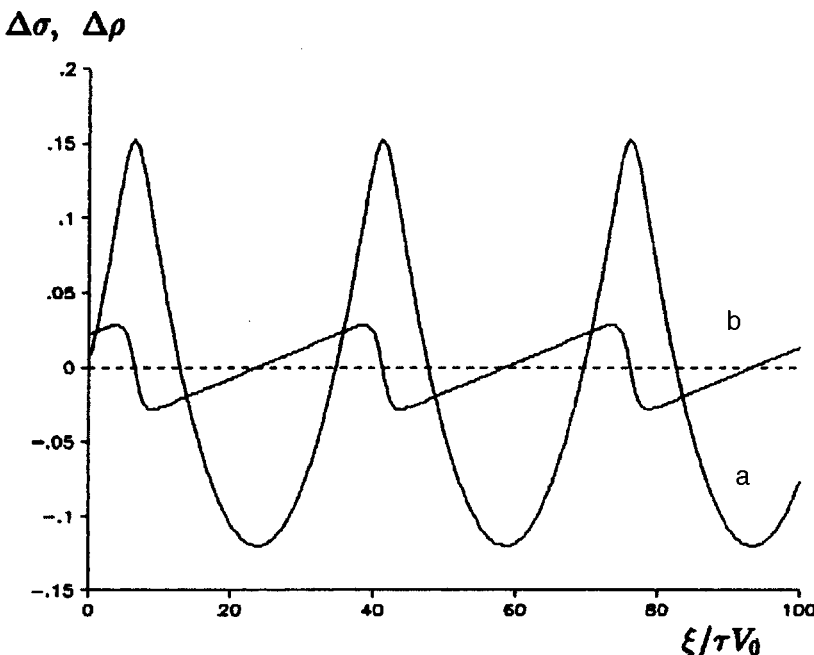

FIG. 2. Normalized periodic pulses of elastic field $\Delta\sigma=(\sigma-\sigma_2)/G^*$ (a) and excess dislocation density $\Delta\rho=(I-I_c)/\dot{\varepsilon}_p\tau\rho_0$ (b) as a numerical solution of Eq. (10) for given values of the parameters ($\dot{\varepsilon}_p>\dot{\varepsilon}_{pc}$): $\alpha=0.1$, $\beta=0.1$, $\dot{\varepsilon}_p\tau=0.02$, $V_c/V_0=0.5$, $\sigma_2/G^*=1$, and $(\sigma_2-\sigma_1)/G^*=0.2$. The calculations were made using the approximation $V=V_c+V'_\sigma(\sigma-\sigma_2)+V'''_\sigma(\sigma-\sigma_2)^3$, where $V'''_\sigma=-6V'_\sigma(\sigma_2-\sigma_1)^{-2}$. The pulses propagate at the velocity $c=\beta V_0$.

through each of which two trajectories pass (separatrixes). Depending on the value of $\dot{\varepsilon}_p$, it is possible to have three separatrix solutions in the form of closed trajectories. For a certain critical value $\dot{\varepsilon}_p=\dot{\varepsilon}_{pc}$ there is a trajectory connecting the singular points $(\sigma_1,0)$ and $(\sigma_3,0)$. This trajectory corresponds to an isolated wave of the broad soliton type. For $\dot{\varepsilon}_p>\dot{\varepsilon}_{pc}$ the source and sink of the closed trajectory is the state $(\sigma_1,0)$ and for $\dot{\varepsilon}<\dot{\varepsilon}_{pc}$ it is $(\sigma_3,0)$. The corresponding soliton solutions are responsible for the evolution (using the terminology of Ref. 13) of domains of strong $(\dot{\varepsilon}_p>\dot{\varepsilon}_{pc})$ and weak $(\dot{\varepsilon}_p<\dot{\varepsilon}_{pc})$ elastic field. On the phase plane there is also a continuum of closed trajectories around the singular point $(\sigma_2,0)$ which are responsible for the propagation of periodically repeating pulses of the field σ and the dislocation charge $bI\sim\sigma'_\xi$ (Fig. 2).

To sum up, the domain instability caused by a change in the crystal hardening mechanism leads to a pulsed plastic flow regime. The flow instability is usually accompanied by localization of glide.[3,4] In our model the width of the localized glide band is determined by the given parameters ($L=\eta L_0\dot{\varepsilon}_0/b\rho_0V_0$). However, it should be borne in mind that the glide bands are two-dimensional formations and thus a strict description of the growth dynamics and profile of a localized glide band should be made using a systematic two-dimensional formulation of the problem. Such a description is outside the scope of the present paper and will be published separately.

This work was supported by the Russian Fund for Fundamental Research (Grant No. 96-02-18185).

[1] B. I. Smirnov, *Dislocation Structure and Hardening of Crystals*, Nauka, Leningrad (1981), 275 pp.
[2] V. I. Trefilov, V. F. Moiseev, É. P. Pechkovskiĭ *et al.*, *Strain Hardening and Fracture of Polycrystalline Materials* [in Russian], Naukova Dumka, Kiev (1987), 245 pp.
[3] A. Luft, Prog. Mater. Sci. **35**, 97 (1991).
[4] B. I. Smirnov and V. I. Nikolaev, Fiz. Tverd. Tela (St. Petersburg) **35**, 1881 (1993) [Phys. Solid State **35**, 939 (1993)].
[5] G. A. Malygin, Fiz. Tverd. Tela (St. Petersburg) **37**(1), 3 (1995) [Phys. Solid State **37**, 1 (1995)].
[6] A. H. Cottrell, *Dislocations and Plastic Flow in Crystals* (Clarendon Press, Oxford, 1953; Metallurgizdat, Moscow, 1958, 267 pp.).
[7] P. Penning, Acta Metall. **20**, 1169 (1972).
[8] L. P. Kubin, Mater. Sci. Technol. **6**, 137 (1993).
[9] S. N. Nagornykh and G. F. Sarafanov, Izv. Akad. Nauk Ser. Metall. **3**, 199 (1993).
[10] B. I. Khudik, Metallofizika **10**(5), 41 (1988).
[11] I. L. Maksimov and G. F. Sarafanov, JETP Lett. **61**, 411 (1995).
[12] D. Hall, *Introduction to Dislocations* [Russ. transl.], Atomizdat, Moscow (1968), 280 pp.
[13] Dzh. Gann, Usp. Fiz. Nauk **89**, 147 (1966).

Translated by R. M. Durham

Determination of electron transport coefficients in argon from ignition curves of rf and combined low-pressure discharges

V. A. Lisovskiĭ

Kharkov State University

(Submitted August 26, 1996; resubmitted November 3, 1997)
Pis'ma Zh. Tekh. Fiz. **24**, 49–55 (April 26, 1998)

Ignition curves of rf and combined (rf+static electric field) low-pressure discharges are used to determine the electron drift velocity $V_{\rm dr}$ in the range $E/p \approx 70-2000$ V/(cm·Torr) and the ratio of the longitudinal diffusion coefficient to the electron mobility D_L/μ_e in the range $E/p \approx 1-2000$ V/(cm·Torr). © *1998 American Institute of Physics.* [S1063-7850(98)02304-0]

Two of the main parameters which describe the motion of electrons in a gas under the influence of an electric field are the electron drift velocity $V_{\rm dr}$ and the ratio of the diffusion coefficient to the electron mobility D_e/μ_e. The measured values of D_e/μ_e are directly related to the average energy of the random electron motion in the steady-state regime while the drift velocity $V_{\rm dr}$ characterizes the electrical conductivity of a weakly ionized gas.

Various methods of measuring $V_{\rm dr}$ and D_e/μ_e have now been developed (such as the time-of-flight method and a method of recording the optical radiation pulse of a moving electron cloud). A detailed description of these methods and their results are given in Refs. 1 and 2. These methods can be used to determine $V_{\rm dr}$ in the range $E/p \leqslant 200-300$ V/(cm·Torr). At higher values of E/p, a discharge burns between the electrodes of the experimental system and in many cases, measurements are difficult.

Whereas in the other methods noted above, the ignition of a discharge is regarded as an undesirable phenomenon, the method of determining the electron transport coefficients proposed here is, in contrast, based on studying the breakdown of the gas.

In the present study measurements were made of the ignition curves of rf and longitudinal combined (dc and rf voltages are applied to the same electrodes) discharges in argon in the pressure range $p = 10^{-2}-20$ Torr, rf field frequency $f = 13.56$ MHz, rf voltage $U_{\rm rf} \leqslant 10^3$ V, and dc voltage between the electrodes $U_{\rm dc} \leqslant 600$ V. The distance between the stainless steel electrodes 100 mm in diameter was varied over the range $L = 6-29$ mm. The method of measuring the ignition curves of an rf discharge was described in detail in Refs. 3–6.

The electron drift velocity $V_{\rm dr}$ was determined from the position of the turning point of the rf discharge ignition curve (Fig. 1a). Electron motion in a uniform rf field is considered. The single-particle approximation is used, i.e., the motion of an electron cloud will be described as the motion of some ''average'' electron without specifying in detail the electron energy distribution function. The use of the single-particle approximation in this case can be justified by the following arguments. First, from the experimental results and theoretical calculations made by other authors[7–17] (Fig. 2a) it can be seen that in the range $E/p \sim 1-500$ V/(cm·Torr) the electron drift velocity is $V_{\rm dr} \sim E/p$. This implies that over a wide range of E/p in the presence of inelastic electron collisions with argon atoms (excitation, ionization), the effective electron-atom collision frequency ν_{en} depends weakly on E/p and the average electron energy $\bar{\varepsilon}$ is almost constant in this range of E/p (Refs. 10 and 16). Second, under our experimental conditions, the energy relaxation time τ is always considerably greater than the reciprocal cyclic frequency of the rf field ($\tau\omega \sim 10-15$) so that an electron distribution is formed with a certain average energy $\bar{\varepsilon}$ weakly modulated by the applied rf field. Thus, for the electron drift velocity in an rf field we can write

$$v_{\rm dr}(t) = \frac{eE_{\rm rf}}{m\nu_{en}}\cos(\omega t), \qquad (1)$$

where e and m are the electron charge and mass, $E_{\rm rf}$ is the amplitude of the rf field, and $\omega = 2\pi f$. The peak value of the electron drift velocity $V_{\rm dr} = eE_{\rm rf}/(m\nu_{en})$ is the maximum instantaneous electron velocity corresponding to the highest value (amplitude) of the rf field. The amplitude of the electron displacement in the rf field is $A = eE_{\rm rf}/(m\nu_{en}\omega) = V_{\rm dr}/\omega$. However, at the turning point the amplitude of the electron displacement is $A = L/2$ (Ref. 3). Thus, for the electron drift velocity we have

$$V_{\rm dr} = L\pi f; \qquad (2)$$

for fixed frequencies f of the rf field and the interelectrode gap L at the turning point $V_{\rm dr}$ is constant and does not depend on the type of gas. The coordinates of the turning point (the pressure p_t and rf voltage U_t) can be used to calculate the ratio E/p which corresponds to this electron drift velocity. In strong electric fields ($E/p > 1000$ V/(cm·Torr)) the electron drift velocity is $V_{\rm dr} \sim (E/p)^{1/2}$. In this case, however, the relation $A = V_{\rm dr}/\omega$ is valid so that formula (2) must be used. The electron drift velocities thus determined (Fig. 2a) show satisfactory agreement with the experimental results[7–12] and also with the theoretical results[10,13–17] of other authors.

 © 1998 American Institute of Physics

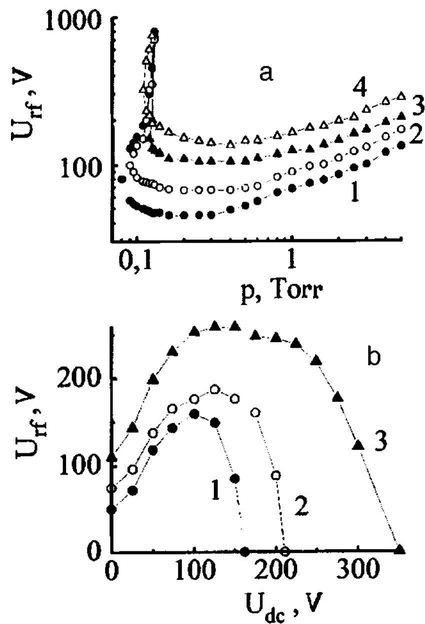

FIG. 1. a—rf breakdown voltage versus argon pressure for dc voltages: *1*—$U_{dc}=0$, *2*—25 V, *3*—50 V, *4*—100 V; b—rf breakdown voltage versus dc voltage at argon pressures: *1*—$p=0.2$ Torr, *2*—1 Torr, *3*—3 Torr; $L=23$ mm.

In Eq. (1) it was assumed that $\nu_{en}\gg\omega$. In our case, this assumption is quite justified since, even for $L=29$ mm, the relation $\nu_{en}\approx 7\omega$ is satisfied at the turning point of the ignition curve.

A method of determining the ratio of the longitudinal diffusion coefficient to the electron mobility D_L/μ_e is now considered. We take the equation for gas breakdown in a uniform rf field[18]

$$\exp\left(\frac{B_0p}{2E_0}\right)=A_1pL\left(1-\frac{E_0/B_0p}{C_2L/\Lambda}\right) \tag{3}$$

and the equation for gas breakdown in rf and weak dc electric fields[5,6]

$$\exp\left(\frac{B_0p}{2E_1}\right)=A_1pL\left(1-\frac{E_1/B_0P}{C_2L/\Lambda}\right)\times\left\{1+\left(\frac{E_{dc}L_{rf1}}{2\pi D_e/\mu_e}\right)^2\right\}^{-1/2}. \tag{4}$$

We divide Eq. (4) by Eq. (3) to obtain an expression for D_e/μ_e:

$$\frac{D_e}{\mu_e}=\frac{E_{dc}L_{rf1}}{2\pi}\left\{\left(\frac{L_{rf1}}{L_{rf0}}\right)^2\exp\left(B_0p\,\frac{E_1-E_0}{E_0E_1}\right)-1\right\}^{-1/2}, \tag{5}$$

where

$$L_{rf0,1}=L\left\{1-\frac{E_{0,1}/B_0p}{C_2L/\Lambda}\right\}, \tag{6}$$

E_0 and E_1 are the effective breakdown rf fields without and with an external dc field E_{dc}, A_1, B_0, and C_2 are the molecular constants,[6] and Λ is the vacuum wavelength of the rf field. In Eq. (4) D_e/μ_e appears in the term which allows for the contribution of the dc field E_{dc} to the rf breakdown of the gas. Thus, Eq. (5) yields the required dependence $D_e/\mu_e=\varphi(E_{dc},p)$. A similar method was used in Ref. 19 to determine D_e/μ_e from the ignition curves of a microwave discharge with an applied weak dc field. It is known[9,14,20] that an electron cloud moving in a gas in the presence of an electric field E is scattered relative to the center of mass with the diffusion coefficient D_L parallel to the direction of E, which in general differs from the transverse diffusion coefficient D_e. Since it was assumed in the derivation of Eqs. (3) and (4) that breakdown takes place in a uniform electric field between infinitely large planar electrodes and transverse electron diffusion can be neglected, the electrons only diffuse toward the electrodes (in the direction of the electric field). Thus, Eq. (5) gives D_L/μ_e rather than D_e/μ_e, where D_L is the coefficient of longitudinal electron diffusion. Thus, to calculate D_L/μ_e the ignition curves of a combined rf discharge with $L\leq 23$ mm were used, i.e., the gap between the electrodes was considerably smaller than the electrode diameter. In addition, we note that Eq. (4) was derived for the case of a weak dc field which makes no contribution to the ionization of the gas. Thus, first we only analyzed the ascending section of the curve $U_{rf1}=\psi(U_{dc})$ (Fig. 1b). Second, the pressure range corresponding to the section of the rf ignition curve between the minimum and the point of inflection was selected to calculate the ratio D_L/μ_e (in Fig. 1a this pressure range lies in the region $0.2\leq p\leq 1$ Torr). This condition is imposed because Eq. (3) best describes the ignition curve of an rf discharge specifically in this pressure range and in consequence, the measurement error for D_L/μ_e is

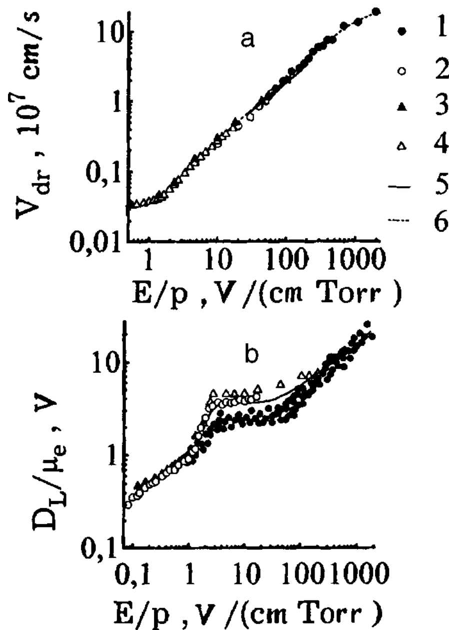

FIG. 2. a—Electron drift velocity versus E/p: *1*—our results, *2*—experimental data from Ref. 7, *3*—experimental data from Ref. 10, *4*—experimental data from Ref. 12, *5*—calculations from Ref. 15, *6*—calculations from Ref. 10, b—ratio of longitudinal diffusion coefficient to electron mobility versus E/p: *1*—our results, *2*—experimental data from Ref. 12, *3*—experimental data from Ref. 9, *4*—experimental data from Ref. 10, and *5*—calculations from Ref. 10.

lowest for this method. Figure 2b gives our values of D_L/μ_e which agree satisfactorily with the results of Refs. 9, 10, 12, and 15.

To sum up, the electron drift velocity V_{dr} and the ratio of the longitudinal diffusion coefficient to the electron mobility D_L/μ_e have been determined from the experimental ignition curves of rf and longitudinal combined low-pressure discharges. The results presented here show satisfactory agreement with the experimental and theoretical results of other authors.

[1] L. G. H. Huxley and R. W. Crompton, *The Diffusion and Drift of Electrons in Gases* (Wiley, New York, 1974; Mir, Moscow, 1977), 672 pp.
[2] G. Reger, *Electron Avalanches and Breakdown in Gases* [Russ. transl.], Mir, Moscow (1968), 392 pp.
[3] S. M. Levitskiĭ, Zh. Tekh. Fiz. **27**, 970 (1957) [Sov. Phys. Tech. Phys. **2**, 887 (1957)].
[4] N. Yu. Kropotov, Yu. A. Kachanov, A. G. Reuka, V. A. Lisovskiĭ, V. D. Egorenkov, and V. I. Farenik, Pis'ma Zh. Tekh. Fiz. **14**, 359 (1988) [Sov. Tech. Phys. Lett. **14**, 159 (1988)].
[5] V. A. Lisovskiĭ and V. D. Egorenkov, Pis'ma Zh. Tekh. Fiz. **18**(17), 66 (1992) Tech. Phys. Lett. **18**, 573 (1992)].
[6] V. A. Lisovsky and V. D. Yegorenkov, J. Phys. D **27**, 2340 (1994).
[7] G. Jager and W. Otto, Z. Phys. **169**, 517 (1962).
[8] J. Brambring, Z. Phys. **179**, 539 (1964).
[9] E. B. Wagner, F. J. Davis, and G. S. Hurst, J. Chem. Phys. **47**, 3138 (1967).
[10] H. N. Kucukarpaci and J. Lucas, J. Phys. D **14**, 2001 (1981).
[11] S. A. J. Al-Amin and J. Lucas, J. Phys. D **20**, 1590 (1987).
[12] Y. Nakamura and M. Kurachi, J. Phys. D **21**, 718 (1988).
[13] A. G. Engelhardt and A. V. Phelps, Phys. Rev. A **133**, 375 (1964).
[14] J. J. Lowke and J. H. Parker, Phys. Rev. **181**, 302 (1969).
[15] Y. Sakai, H. Tagashira, and S. Sakamodo, J. Phys. D **10**, 1035 (1977).
[16] V. Puech and L. Torchin, J. Phys. D **19**, 2304 (1986).
[17] K. Maeda and T. Makabe, Physica Scripta **T53**, 61 (1994).
[18] T. Kihara, Rev. Mod. Phys. **24**, 45 (1952).
[19] L. J. Varnerin and S. C. Brown, Phys. Rev. **79**, 946 (1950).
[20] H. R. Skullerud, J. Phys. B **2**, 696 (1969).

Translated by R. M. Durham

Quantum oscillations of the differential resistance of superconductor–two-dimensional electron gas contacts

V. N. Gubankov, M. P. Lisitskiĭ, and S. S. Shmelev

Institute of Radio Engineering and Electronics, Russian Academy of Sciences, Moscow

(Submitted July 29, 1997)
Pis'ma Zh. Tekh. Fiz. **24**, 56–61 (April 26, 1998)

Oscillations of the differential resistance of a superconductor–two-dimensional electron gas contact were observed at low temperatures. These oscillations reflect the quantum nature of the electric charge transport perpendicular to the two-dimensional electron gas. © *1998 American Institute of Physics.* [S1063-7850(98)02404-5]

Studies of the properties of superconductor–two-dimensional electron gas (SC–2DEG) contacts are of interest mainly from the point of view of analyzing electric charge transport processes from one macroscopic quantum system to another which differs qualitatively from the first. Moreover, specific transport characteristics may be associated with specific features of the contact region, especially if its dimensions are smaller than the characteristic spatial scales of the contact systems (the coherence length and the electron mean free path). So far, in the vast majority of the studies of SC–2DEG structures (see for example, Refs. 1 and 2), charge transport has been observed along a channel containing a two-dimensional electron gas with a superconducting switch. Here we attempt to use a direct SC–2DEG contact where the transport current propagates perpendicular to the plane of the two-dimensional electron gas. We observed some characteristic features of the behavior of the differential resistance of the contact which are attributed to the structure of the energy spectrum of the two-dimensional electron gas.

We investigated In–GaAs/AlGaAs contacts, fabricated using molecular beam epitaxy on a single-crystal semi-insulating GaAs wafer 300 μm thick by systematically growing the following layers:

1) an undoped n-GaAs buffer layer (0.7 μm thick);

2) an undoped AlGaAs layer (spacer) (0.005 μm thick);

3) a doped $Al_xGa_{1-x}As$ layer ($x=0.3$, $n\sim 7\times 10^{17}$ cm^{-3}, 0.06 μm thick);

4) an Si-doped n^+-GaAs layer ($n\sim 2\times 10^{18}$ cm^{-3}, 0.02 μm thick).

The prepared wafer was cut into various square sections (substrates) with a side length of 5 mm. Ohmic point contacts to the region containing the two-dimensional electron gas were fabricated in each corner of the substrate and were used to measure the Hall effect by the van der Pauw method (the area of each point contact was $\sim 0.3\times 0.3$ mm).

The Ohmic contacts were formed by the thermal deposition of In followed by brazing at $T=300$ °C for 5 min. After four corner point contacts had been prepared, the SC–2DEG contact was formed. An indium tunneling contact with a circular cross section of diameter 4 mm was formed by thermal deposition of a 0.2 μm thick In film through a metal mask and then annealing the sample at $T=300$ °C for less than 5 min.

The mobility and carrier concentration in the region containing the two-dimensional electron gas was estimated experimentally at room temperature and liquid-nitrogen temperature from measurements of the Hall effect. It was observed that the electron mobility increases from 2900 cm^2/V·s at room temperature to 20 000 cm^2/V·s at liquid-nitrogen temperature, which is a direct consequence of the existence of a two-dimensional electron gas in the GaAs/AlGaAs heterostructure after the thermal processes have been completed.

Measurements of the current-voltage characteristics of the In-GaAs/AlGaAs contact were made by a four-probe method: I^+ and V^+ probes were connected to the central circular cross-section indium contact while the I^- and V^- probes were connected to two corner Ohmic contacts. The differential resistance dV/dI of the contact was measured by sinusoidal current modulation using synchronous detection of the signal at the contact.

At room temperature the current–voltage characteristic of the contact was linear in the range of voltages up to ± 4 mV (the resistance of the contact was 146 Ω). When the temperature was reduced to 4.2 K, the current-voltage characteristic became nonlinear and the resistance of the contact increased at $V=0$. The nonlinearity of the characteristic showed up clearly on the dependence of dV/dI on the bias voltage V. Figure 1 shows curves of $dV/dI(V)$ measured at different temperatures. The curves $dV/dI(V)$ measured in the range $T_c<T<4.2$ K (for indium $T_c=3.4$ K) were similar with a slight increase in the dV/dI peak at zero bias. As the temperature then decreased further below T_c, a sharp increase in the dV/dI peak was observed at $V=0$ and characteristic dV/dI minima appeared at $V\sim 0.5$ mV. These characteristics were observed earlier for Sn–GaAs contacts[3] and n^{++}GaAs–Nb contacts[4] at low temperatures. At $T=1.6$ K—the lowest temperature achieved in this experiment—well-defined oscillations with a characteristic period of ~ 1 mV were detected on the curve $dV/dI(V)$ (Fig. 2).

It is known that tunneling processes through the Schottky barrier in superconductor-degenerate semiconduc-

 © 1998 American Institute of Physics

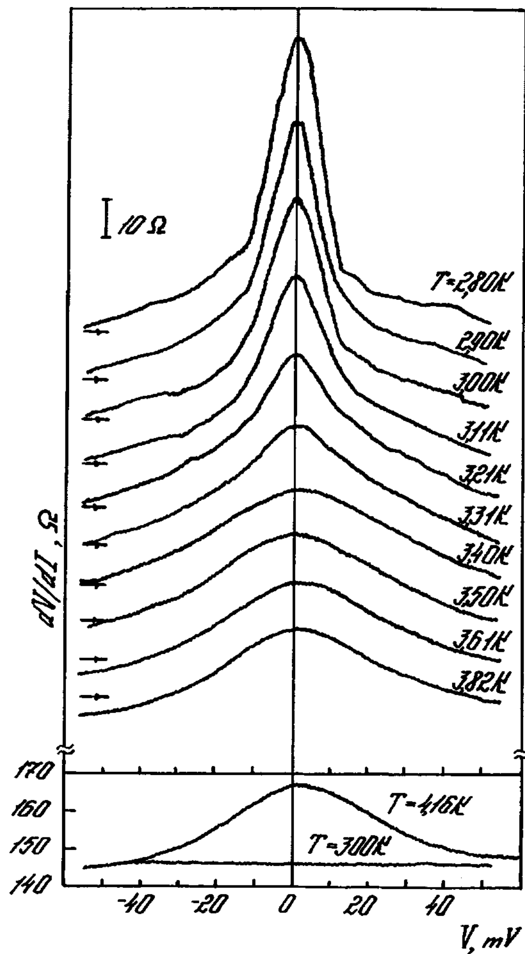

FIG. 1. Curves of $dV/dI(V)$ at various temperatures. The curves measured in the range $T \leqslant 3.82$ K are shifted relative to each other (for each curve the arrow indicates the value $dV/dI = 150\ \Omega$).

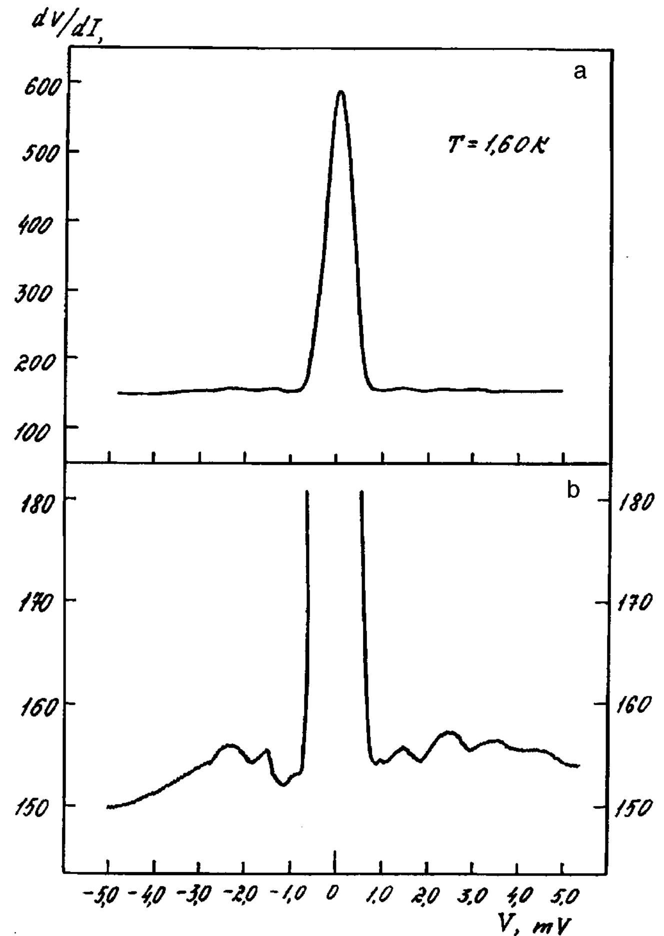

FIG. 2. a—Curve of $dV/dI(V)$ measured at $T = 1.6$ K; b—the same curve shown on an enlarged current scale.

tor contacts at voltages $V \lesssim \Delta/e$ (Δ is the energy gap of the superconductor and e is the electron charge) are similar to the processes which take place in superconductor-insulator-normal metal (SIN) contacts. In fact, the form of the dependences $dV/dI(V)$ measured at $T < T_c$ is similar to those of an SIN contact. From this it can be concluded that the observed current-voltage characteristics and curves $dV/dI(V)$ reflect the tunneling of single-particle excitations through the Schottky barrier formed at the interface between the indium and the doped $Al_xGa_{1-x}As$ and the characteristic $dV/dI(V)$ minima are caused by the presence of an energy gap in the quasiparticle spectrum of the superconducting In.

The oscillations of $dV/dI(V)$ observed at $T = 1.6$ K with a typical period of ~ 1 mV are most likely caused by the appearance of quantum levels in the electronic spectrum of the excitations of the two-dimensional electron gas when charge is transported perpendicular to the plane of the electron gas.[5] The characteristic scale of the oscillations on the voltage axis is of the same order of magnitude as the results of theoretical estimates of the difference between the electronic quantization levels in a two-dimensional electron gas using the triangular potential model.[6] The dispersion of the period of the dV/dI oscillations may be caused by blurring of the distance between the region containing the two-dimensional electron gas and the diffused indium in the contact plane.

To sum up, when In was transferred to the superconducting state, these In–GaAs/AlGaAs contacts possessed properties corresponding to those of a superconductor–Schottky barrier–doped semiconductor–two-dimensional electron gas structure with charge transport perpendicular to the plane of the two-dimensional electron gas.

This work was financed by the Russian Fund for Fundamental Research, Grant No. 95-02-04449.

[1] A. W. Kleinsasser, T. N. Jackson, D. McInturff *et al.*, Appl. Phys. Lett. **55**, 1909 (1989).
[2] J. R. Gao, J. P. Heida, B. J. van Wees *et al.*, Surf. Sci. **305**, 470 (1994).
[3] J. R. Gao, J. P. Heida, B. J. van Wees *et al.*, Appl. Phys. Lett. **63**, 334 (1993).
[4] V. I. Barchukova, V. N. Gubankov, E. N. Enyushkina *et al.*, Pis'ma Zh. Tekh. Fiz. **21**(6), 12 (1995) [Tech. Phys. Lett. **21**, 208 (1995)].
[5] M. Shur, *Physics of Semiconductor Devices*, in 2 Books [in Russian], Mir, Moscow (1992), Book 1, p. 479.
[6] M. Shur, *Modern Devices Using Gallium Arsenide* [in Russian], Mir, Moscow (1991), p. 632.

Translated by R. M. Durham

Electric dynamic fatigue in ferroelectric complex oxides

V. G. Gavrilyachenko, N. V. Reshetnyak, L. A. Reznichenko, S. V. Gavrilyachenko, A. F. Semenchev, and S. I. Dudkina

Rostov State University, Scientific-Research Institute of Physics
(Submitted July 23, 1997)
Pis'ma Zh. Tekh. Fiz. **24**, 62–66 (April 26, 1998)

Data are presented on the fatigue of ferroelectric materials induced by cyclic polarization reversal by an ac field. It is suggested that the electric fatigue of the samples is caused by an increase in the defect concentration in the crystal structure. © *1998 American Institute of Physics.* [S1063-7850(98)02504-X]

Ferroelectric materials are widely used in electronic engineering devices operated under extreme conditions, for example as cold cathodes in electric vacuum devices. An informative test as to the suitability of a material for operation under these conditions involves studying the kinetics of the electric dynamic fatigue—the degradation of the electrophysical properties under cyclic polarization reversal by an ac field.[1,2]

For the investigations we prepared samples of ferroelectric solid solutions of different structural types:

—lead zirconate titanate solid solutions belonging to different regions of the phase diagrams of the corresponding systems (rhombohedral, tetragonal, and the morphotropic phase transition region);

—sodium niobate solid solutions of the type $NaNbO_3$–$ANbO_3$ where A=Li, K, and $NaNbO_3$–$PbTiO_3$.

All the samples were prepared by hot pressing. The dielectric hysteresis loops were used to determine the relative changes in the remanent polarization P_r and the coercive field E_c as a function of the number of switching cycles N. Dielectric, x-ray structural, and electron-microscopic analyses were also made.

An analysis of data for samples of different compositions and structural types showed that the fatigue kinetics differs appreciably in ferrosoft and ferrohard compositions. In ferrosoft compositions a hysteresis loop forms over several cycles, then P_r decreases and E_c increases.

For the ferrosoft six-component system

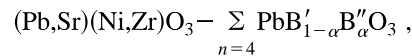

$$(\mathrm{Pb,Sr})(\mathrm{Ni,Zr})\mathrm{O}_3 - \sum_{n=4} \mathrm{PbB}'_{1-\alpha}\mathrm{B}''_{\alpha}\mathrm{O}_3 ,$$

where B'=W,Nb and B''=Zn,Mg,Ni,Li, we established that compositions from the orthorhombic region exhibit the highest stability—P_r decays by 50% for $N \geqslant 2\times10^7$. For compositions belonging to the morphotropic phase transition region, P_r typically increases by (15–20)% for $N \simeq 10^5$ and then decreases to 50% of the initial value for $N \leqslant 10^7$. The fatigue rates of compositions from the tetragonal region are the highest, with a 50% decrease in P_r for $N=10^6$. For all compositions in the system E_c increases smoothly with increasing N and the permittivity ε decreases by a factor of approximately 2–3 as N increases from 10^3 to 10^6. We obtained similar results in studies of ferrosoft solid solutions based on sodium niobate, PKR-1 and PKR-7m, and lead zir-

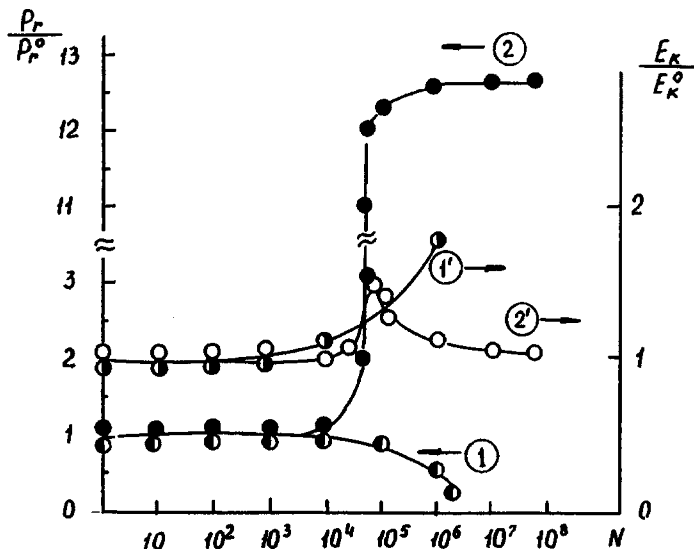

FIG. 1. Relative changes in the remanent polarization P_r/P_r^0 and the coercive field E_c/E_c^0 as a function of the number of switching cycles N for tetragonal compositions: ferrosoft (*1*) and (*1′*) and ferrohard (*2*) and (*2′*).

 © 1998 American Institute of Physics

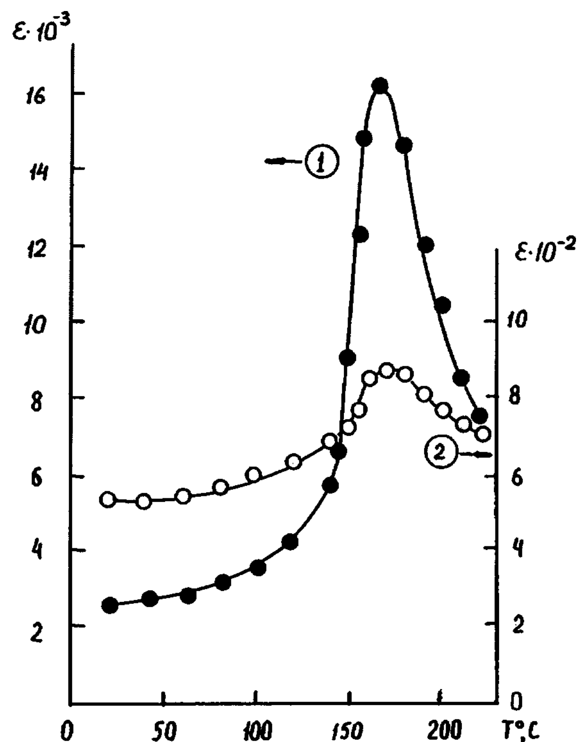

FIG. 2. Temperature dependences of the permittivity ε of a ferrosoft composition: *1*—initial state and *2*—after $N=10^6$ switching cycles.

conate titanate in which the lead is partially substituted by lanthanum 8/65/35. The authors of Refs. 1 and 2 also obtained similar results.

In ferrohard compositions the formation of a hysteresis loop takes longer (P_r and E_c increase up to $N=10^5$).

For comparison Fig. 1 shows the relative variations of P_r and E_c for tetragonal compositions from the ferrosoft six-component system ($P_r^0=0.21$ C/m^2, $E_C^0=6\times10^5$ V/m) and the ferrohard four-component system

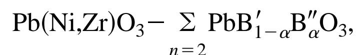

$$\mathrm{Pb(Ni,Zr)O_3}-\sum_{n=2}\mathrm{PbB'_{1-\alpha}B''_{\alpha}O_3},$$

where B′=W,Nb and B″=Mn ($P_r^0=0.02$ C/m^2, $E_C^0=2.5\times10^6$ V/m). In the second case, an avalanche-like increase in P_r is observed after a fairly large number of cycles and then P_r remains the same as far as $N=10^8$. It is interesting to note that E_c increases as P_r increases rapidly, and then decreases smoothly to E_c^0. This behavior is also typical of the ferrohard materials PKR-8 and PKR-13 and differs fundamentally from the data for PZT-8 (Ref. 2).

What is the reason for this unexpected difference in the electrical fatigue rates of ferrosoft and ferrohard materials? It has already been established that the domain structure of the crystallites in the ferrosoft materials PKR-1, PKR-7m, and others consists mainly of 180° domains. Under the action of a strong dc or ac electric field, the concentration of twins in the crystallites increases appreciably.[3] We postulate that under cyclic polarization reversal, nonuniform mechanical stresses are created in the ceramic samples, leading to continuous twinning and untwinning of crystallites. This process generates defects in the crystal structure which then serve as obstacles for the twin walls. As a result, the twins lose their capacity to move, the complex domain structure of the crystallites becomes frozen, and P_r decreases. Subsequently, microcracks evolve in the bulk of the crystallites and at their boundaries, as was established by electron-microscopic examinations. X-ray structural analyses indicate that the concentration of linear and point defects increases with increasing N.

The defect structure of the "fatigued" samples may explain the suppression and broadening of the phase transition in these samples (Fig. 2).

The stability of ferrohard compositions under cyclic polarization reversal indicates that the defect structure of the crystals changes negligibly. This is confirmed by the absence of any broadening of the phase transition and by the x-ray structural data. This effect may be achieved if, after the formation of the hysteresis loop, only 180° processes take place in the crystallites.

To conclude, electric fatigue in ferroelectric complex oxides is mainly caused by the buildup of defects in the crystal structure and some ferrohard compositions such as PKR-8 and PKR-13 are promising for applications under extreme conditions.

This work was supported by the Russian Fund for Fundamental Research, Grant No. 96-02-18513a.

[1] Q. Y. Jiang, T. C. Subbarao, and L. E. Cross, J. Appl. Phys. **75**, 7433 (1994).
[2] W. Pan, S. Sun, and P. Fuierer, J. Appl. Phys. **74**, 1256 (1993).
[3] V. É. Borodin, É. I. Eknadiosyants, and A. P. Pinskaya, *Semiconductors Ferroelectrics* Vol. 6 [in Russian], Kniga, Rostov (1996), pp. 125–126.

Translated by R. M. Durham

Negative turbulent heat conduction and its role in the formation of large-scale structures

G. V. Levina and S. S. Moiseev

Institute of Continuum Mechanics, Urals Branch of the Russian Academy of Sciences, Perm; Institute of Space Research, Russian Academy of Sciences, Moscow

(Submitted October 23, 1997)
Pis'ma Zh. Tekh. Fiz. **24**, 67–75 (April 26, 1998)

A mechanism is proposed for the establishment of negative heat conduction under conditions of advanced turbulent convection, which leads to the formation of large-scale structures. A semi-empirical model of turbulent convection and experimental results are used to give some quantitative estimates. © *1998 American Institute of Physics.* [S1063-7850(98)02604-4]

Large-scale motion caused by nonuniform heating of a medium can be found in the convective zones of the sun and the stars, in planetary atmospheres, and in the Earth's atmosphere and oceans. A clear illustration of these phenomena may be tropical cyclones—large-scale, long-lived helical vortices of enormous intensity—which occur tens of times a year in the Earth's tropical atmosphere.

In our opinion, two physical mechanisms play a particular role in the generation of these structures. The first, spiral, mechanism appears under conditions of small-scale helical turbulence and creates a tendency for small vortices to merge.[1,2] The second, thermal mechanism appears in the case of a quasi-thermally insulated surface which bounds a region of advanced turbulent convection.[3,4] Whereas the helicity of the velocity field particularly influences the momentum transfer[5] (a drop in pressure and viscosity under conditions where the motion has a helical component can substantially alter the buoyancy and frictional resistance, for example), the thermal insulation of the boundary leads to anisotropy of the thermal conductivity (and even reverses its sign), as will be shown below.

We shall discuss the effect observed by us by considering the convective motion of an incompressible fluid in an infinite planar horizontal layer heated from below. If the thermal conductivity of the boundaries is high, the evolution of mechanical equilibrium instability will lead to the establishment of convective motion in the form of a system of cells, each having a horizontal scale of the order of the layer thickness. An increase in the horizontal scale of the structures in laminar regimes is observed when the thermal conductivity of the layer boundaries decreases.[6] In this case, the cells should tend to expand in the horizontal direction in order to improve the efficiency of heat transfer to the surrounding medium by longer contact between the rising heated fluid and the heat exchange surface. In the limiting case of thermally insulated boundaries, the horizontal scale of the structures tends to infinity (the critical wave number vanishes).

It was shown in Ref. 3 that in turbulent convection the improved thermal insulation of the boundaries combined with the high intensity of the convective motion produces a qualitatively new physical effect, which is responsible for the generation of large-scale structures and ensures their long-lived, stable, existence by transfer of energy from small-scale convection. The authors of Ref. 3 proposed a physical mechanism for the formation of large-scale structures and constructed a semi-empirical model of turbulent convection to describe this effect. An analysis and generalization of the results of recent theoretical studies,[4] laboratory modeling,[4] and natural experiments[7] during the Typhoon-89 and Typhoon-90 expeditions have deepened our understanding of the processes caused by the action of this mechanism (described by the authors as the anomalous heat transfer mechanism) and have yielded an interpretation of this mechanism as an example of anisotropic turbulent heat conduction.

The anomalous heat transfer mechanism is established if two conditions are satisfied. First, small-scale heat carriers must be present in the liquid. Turbulent convection regimes with such heat carriers are well-known from experimental studies[8–10] and are established for Rayleigh numbers Ra $=10^6-10^{10}$ when so-called thermals are generated in boundary layers with unstable temperature stratification. The second condition is that the horizontal boundaries of the flow region must have strong thermal insulation. The principle of the mechanism is shown schematically in Fig. 1.

The effect is based on long-wavelength instability caused by the evolution of random thermal perturbations which create horizontal temperature gradients. These temperature nonuniformities induce convective circulation with liquid rising at the hotter center of the heat spot (see Fig. 1) and sinking at the edges, thereby generating shear flows which are antisymmetric relative to the center of the layer. Thermals which become detached from the boundary layers to form fast-moving vertical thermals (rising hot and sinking cold ones) enter the shear flows and are entrained by them. It is easy to see that the cold thermals from the upper boundary layer are displaced to the peripheral regions of lower temperature while the hot thermals are displaced from the lower boundary to the heated center of the spot.

Thus, some additional advective heat flux is created by the motion of the thermals in the shear flows, directed along the horizontal gradient of the average temperature, i.e., in the direction of higher temperatures. This is an anomalous heat flux unlike that produced by molecular heat conduction,

 © 1998 American Institute of Physics

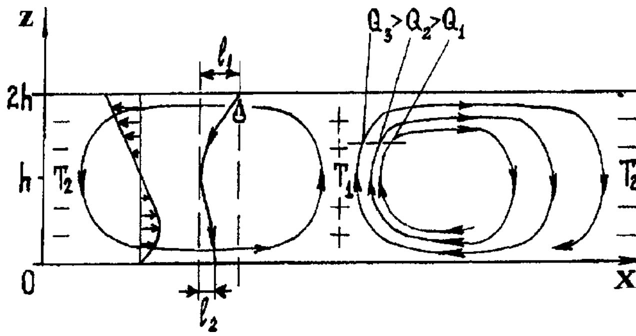

FIG. 1. Schematic showing anomalous heat transfer mechanism.

which is naturally directed toward lower temperature. As a result, the initial temperature difference of the perturbation increases and the rising hot elements thus acquire a larger stored heat per unit mass. Now the hot fluid moving along the upper boundary must cover a greater distance to reach the temperature at which it begins to sink as a result of being cooled by heat transfer to the surrounding medium. This implies that as the intensity increases, the horizontal scale of the perturbation also increases. The most important role in the evolution of the entire instability process is played by the thermal insulation of the boundary, preventing the temperature perturbation from dissipating rapidly. The action of the mechanism results in the formation of convective structures with large-scale circulation, which are stable against a background of small-scale turbulent convection.

In this scenario the turbulent heat transfer processes are accomplished by convective fluxes propagating in all three spatial directions, which is naturally interpreted as the appearance of anisotropy of the turbulent thermal conductivity. This thermal conductivity can now be represented as a tensor $\varkappa^{ij}$ whose diagonal components are determined by the heat fluxes in the corresponding spatial directions. The turbulent thermal conductivity is then positive in the vertical direction and may become negative in the horizontal directions. Quantitative estimates for this effect may be obtained by using a semi-empirical model which describes turbulent convection in a planar infinite horizontal layer of incompressible fluid.

A procedure for deriving averaged equations of turbulent convection from the Boussinesq equations, based on the method of moments, was described in detail in Refs. 3 and 4. In this approach which can isolate large-scale motion from the general turbulent field structure, the physical field is represented as an expansion

$$F(x,y,z,t)=F_0(x,y,t)+(lz-1)F_1(x,y,t)+\dots +F'(x,y,z,t), \quad (1)$$

where $l=h^{-1}$ (the layer thickness is taken as $2h$), F_0 and F_1 are the zeroth- and first-order transverse spatial moments which are given by

$$F_0=\frac{1}{2}l\int_0^{2h}F\,dz, \quad F_1=\frac{3}{2}l\int_0^{2h}F(lz-1)\,dz;$$

F' denotes turbulent fluctuations which in this case are measured from the instantaneous large-scale fields determined by the set of lower moments.

By applying the method of moments to the Boussinesq equations and using various simplifying assumptions,[4] the main one being the "shallow water" approximation, after eliminating the pressure we can obtain the following mathematical model in which, in accordance with Ref. 3, only the two lower moments need be taken into account in the expansions (1) to describe the anomalous heat transfer effect:

$$\Omega_t+\left(\Omega V^i+\frac{1}{3}\omega v^i\right)_i+e^{3ij}(\gamma v^j)_i=-e^{3ij}(M_k^{jk}-\Sigma^j)_i,$$

$$\Theta_t+\left(\Theta V^i+\frac{1}{3}\vartheta v^i\right)_i=-N_i^i+\Lambda,$$

$$\omega_t+(\omega V^i+\Omega v^i)_i=-e^{3ij}(m_k^{jk}-3lM^{j3}-\sigma^j)_i,$$

$$\gamma_t+(\gamma V^i)_i+2V_j^i v_i^j+g\beta h\Theta_{ii}=-(m_j^{ij}-3lM^{i3}-\sigma^i)_i,$$

$$\vartheta_t+(\vartheta V^i+\Theta v^i)_i-\Theta\gamma=-n_i^i+3lN^3+\lambda, \quad (2)$$

where $\Omega=V_x^y-V_y^x$, $\omega=v_x^y-v_y^x$, $V_x^x+V_y^y=0$, $v_x^x+v_y^y=\gamma$.

Here the characteristics of the large-scale fields are written on the left-hand sides of the equations using the following notation: V^i, v^i; Θ and ϑ are the zeroth and first moments of the velocity and temperature, Ω and ω are the z-components of the curl of the field of the zeroth and first moments of the velocity, and γ is the divergence of the field of the first moments of the velocity. The superscripts denote the components of the vectors and tensors while the subscripts denote differentiation with respect to the appropriate variables: $i,j,k=1,2$. The right-hand sides of the equations contain the quantities which characterize the small-scale convective turbulence: M^{ij} and m^{ij} are the momentum transfer tensors, N^i and n^i describe the convective heat transfer, Σ^i and σ^i are the frictional forces at the boundaries, and Λ and λ are the heat influxes from the boundaries. These quantities are given by the following relations:

$$M^{ij}=\frac{1}{2}l\int_0^{2h}u^iu^j\,dz, \quad m^{ij}=\frac{2}{3}l\int_0^{2h}u^iu^j(lz-1)\,dz,$$

$$N^i=\frac{1}{2}l\int_0^{2h}u^iT'\,dz, \quad n^i=\frac{3}{2}l\int_0^{2h}u^iT'(lz-1)\,dz,$$

$$\Sigma^i=\frac{\nu}{2}lu_z^i\Big|_0^{2h}, \quad \sigma^i=\frac{3\nu}{2}l[(lz-1)u_z^i-lu^i]\Big|_0^{2h},$$

$$\Lambda=\frac{\chi}{2}lT_z'\Big|_0^{2h}, \quad \lambda=\frac{3\chi}{2}l[(lz-1)T_z'-lT']\Big|_0^{2h},$$

where u^i, u^j, and T' are the velocity and temperature fluctuations, ν and χ are the kinematic viscosity and the thermal diffusivity of the fluid.

The closing relations for the equations in system (2) obtained and substantiated in Refs. 3 and 11 using the floating thermals model, have the following form:

$$-e^{3ij}(M_k^{jk}-\Sigma^j)_i=\mu\Delta\Omega-\sigma\Omega,$$

$$-N_i^i+\Lambda=\mu\Delta\Theta+\delta\gamma-\alpha\Theta,$$

$$-e^{3ij}(m_k^{jk}-3lM^{j3}-\sigma^j)_i=\mu\Delta\omega-\frac{\mu}{4h^2}\omega-\sigma\omega,$$

$$-(m_j^{ij}-3lM^{i3}-\sigma^i)_i=\mu\Delta\gamma-\frac{\mu}{4h^2}\gamma-\sigma\gamma,$$

$$-n_i^i+3lN^3+\lambda=\mu\Delta\vartheta-\frac{\mu}{4h^2}\vartheta-\alpha\vartheta. \qquad (3)$$

Here the terms containing Laplacians describe turbulent diffusion of the corresponding flow characteristics which leads to equalization of the spatial inhomogeneities of the large-scale fields and ultimately damps them. The terms $\mu\omega/(4h^2)$, $\mu\gamma/(4h^2)$, and $\mu\vartheta/(4h^2)$ describe the damping of large-scale shear flows and inhomogeneities of the vertical temperature gradient by turbulent exchange of momentum and heat between the lower and upper halves of the layer; μ denotes the coefficients of turbulent viscosity and thermal diffusivity, which are assumed to be equal. Wall effects are taken into account by the terms: friction—$\sigma\Omega$, $\sigma\omega$, $\sigma\gamma$, heat transfer—$\alpha\Theta$, α,ϑ, where α and σ are constants. The horizontal convective transfer of heat by moving thermals is described by the term $\delta\gamma$.

Thus, the closing relations contain four empirical constants: α, σ, μ, and δ for which theoretical estimates were obtained in Refs. 3 and 11 using experimental data from Refs. 8 and 9:

$$\alpha=10^{-2}\mathrm{Bi}\,\frac{\sqrt{\nu\chi}}{h^2}\,\mathrm{Ra}^{1/3}, \quad \delta=10^{-3}\frac{\sqrt{\nu\chi^3}}{g\beta h^3}\,\mathrm{Ra}^{5/6},$$

$$\mu=10^{-1}\sqrt{\nu\chi}\mathrm{Ra}^{1/3}, \quad \sigma=10^{-2}\frac{\sqrt{\nu\chi}}{h^2}\,\mathrm{Ra}^{1/3}, \qquad (4)$$

where $\mathrm{Bi}=2h\alpha_1/\varkappa$ is the Biot number which is defined in terms of the coefficient of heat transfer α_1 of the layer and the thermal conductivity $\varkappa$ of the liquid, $\mathrm{Ra}=g\beta\Delta T(2h)^3/(\nu\chi)$ is the Rayleigh number, and g and β are the acceleration due to gravity and the coefficient of thermal expansion of the liquid, respectively.

We shall now make quantitative estimates for the convective heat fluxes in all the spatial directions.

We begin with the horizontal heat fluxes created only by the motion of the thermals. The velocity field in horizontal shear flows generated by a random thermal perturbation (see Fig. 1) is described by the distribution $U^i=v^i(lz-1)$, $i=x,y$. We assume that the hot and cold thermals which become detached from the boundary layers and enter these flows are completely entrained by them, thus acquiring horizontal velocities in opposite directions in the upper and lower halves of the layer. This creates a horizontal convective heat flux in the direction opposite to the corresponding coordinate axis.

Some approximate quantitative estimates for the generated convective fluxes may be obtained from the equations for the zeroth moment of the temperature Θ in Eq. (2) using the appropriate closing relation from system (3). In fact, the rate of change in the average temperature of the fluid in the vertical cross section of the layer as a result of anomalous heat transfer by thermals is equal to the divergence of the heat flux N^i $(i=x,y)$, divided by the specific heat of a fluid column of height $2h$ per unit cross-sectional area:

$$\Theta_t+\left(\Theta V^i+\frac{1}{3}\vartheta v^i\right)_i=-\frac{N_i^i}{2h\rho c}=\delta\gamma,$$

where ρ and c are the density and specific heat of the fluid. Substituting the values of the empirical constant δ from Eq. (4) and assuming that $\gamma=v_i^i$, we obtain estimates for the negative heat flux generated by the thermals:

$$|N_T^i|=2\cdot 10^{-3}\,\frac{\varkappa\sqrt{\nu\chi}}{g\beta h^2}\,\mathrm{Ra}^{5/6}v^i. \qquad (5)$$

An estimate for the vertical heat flux, expressed in terms of the parameters of the thermals, was obtained in Ref. 11 using a general procedure which was proposed to determine the empirical constants in the closing relations (4). The heat transfer law for the floating thermals was obtained in Ref. 11 as follows:

$$\mathrm{Nu}\approx 2\times 10^{-2}\,\mathrm{Ra}^{1/3},$$

where Nu is the Nusselt number. This result agrees satisfactorily with the numerous experimental data now available on the establishment of a heat transfer law for turbulent convection in the range of Rayleigh numbers of interest to us, 10^6-10^{10}.

The horizontal heat fluxes produced by molecular heat conduction are given by

$$|N_\mu^i|=\varkappa(\mathrm{grad}\ T)^i. \qquad (6)$$

Assuming that the molecular and convective heat fluxes in the horizontal plane of the layer are in opposite directions, we obtain from Eqs. (5) and (6) the condition for which $\varkappa^{xx}$ and $\varkappa^{yy}$—the components of the tensor turbulent thermal conductivity—become negative

$$|N_T^i|>|N_\mu^i|. \qquad (7)$$

This condition allows us to obtain an approximate estimate of the order-of-magnitude horizontal velocity for which anomalous heat transfer takes place. As an example we substitute into Eq. (7) values from the operating range of parameters used in Ref. 4 in laboratory experiments to model large-scale structures: $\nu=0.4674\times 10^{-6}$ m^2/s, $\chi=0.157\times 10^{-6}$ m^2/s, $\beta=0.51\times 10^{-3}$ K^{-1}, $h=10^{-2}$ m, $\mathrm{Ra}=6\times 10^6$ and for the thermal perturbation we take a typical temperature difference of 1 K at a distance of 0.5 m. Then, shear flow velocities of $u^i>0.42\times 10^{-2}$ m/s are required for the negative heat conduction effect.

In experiments using natural systems during the Typhoon-89 and Typhoon-90 expeditions, an additional advective heat flux was recorded,[7] directed in some cases at an acute angle ($\approx 20°$) to the horizontal gradient of the average temperature in agreement with the analysis described above.

This work was supported by the Russian Fund for Fundamental Research under Grants No. 95-01-01094a and 96-02-19506.

[1] S. S. Moiseev, R. Z. Sagdeev, A. V. Tur *et al.*, Zh. Éksp. Teor. Fiz. **85**, 1979 (1983) [Sov. Phys. JETP **58**, 1149 (1983)].
[2] S. S. Moiseev, P. B. Rutkevich, A. V. Tur *et al.*, Zh. Éksp. Teor. Fiz. **94**(2), 144 (1988) [Sov. Phys. JETP **67**, 294 (1988)].
[3] V. D. Zimin, G. V. Levina, S. S. Moiseev *et al.*, Dokl. Akad. Nauk SSSR **309**, 88 (1989) [Sov. Phys. Dokl. **34**, 1003 (1989)].
[4] V. D. Zimin, G. V. Levina, S. S. Moiseev *et al.*, Izv. Ross. Akad. Nauk. Ser. Mekh. Zhidk. Gaza No. 5, 20 (1996).
[5] S. S. Moiseev, H. H. Branover, A. A. Eidelman *et al.*, Phys. Chem. Earth **21**, 545 (1996).
[6] G. Z. Gershuni and E. M. Zhukhovitskiĭ, *Convective Stability of an Incompressible Fluid* [in Russian], Nauka, Moscow (1972).
[7] V. D. Zimin, G. V. Levina, S. S. Moiseev *et al.*, *Nonlinear Dynamics of Structures* (World Scientific, Singapore 1991).
[8] I. F. Davenport and C. J. King, Trans. ASME C **97**, 476 (1975).
[9] S. S. Kutateladze and V. S. Berdnikov, Int. J. Heat Mass Transf. **27**, 1595 (1984).
[10] V. D. Zimin and P. G. Frik, *Turbulent Convection* [in Russian] Nauka, Moscow (1988).
[11] G. V. Levina and M. V. Starkov, *Mechanics and Control Processes, Nonlinear Dynamic Systems* [in Russian], Perm State University Press, Perm (1997)

Translated by R. M. Durham

Influence of corrosion of a metal electrode on the polarization sensitivity of a photodetector based on an Ag–GaAs(InP) Schottky barrier with a corrugated interface

N. L. Dmitruk, O. Yu. Maeva, S. V. Mamykin, O. V. Fursenko, and O. B. Yastrubchak

Institute of Semiconductor Physics, Ukraine National Academy of Sciences, Kiev
(Submitted August 12, 1997)
Pis'ma Zh. Tekh. Fiz. **24**, 76–82 (April 26, 1998)

An analysis is made of the influence of corrosion of a metal electrode (Ag) on the total photoresponse of a barrier structure with a corrugated interface and on the component associated with the excitation of a surface polariton. Current-voltage and ellipsometric measurements are used to determine the variation of the barrier parameters and the thickness of the upper electrode as a function of time. © *1998 American Institute of Physics.*
[S1063-7850(98)02704-9]

The main structural element of a photodetector which is sensitive to the wavelength, angle of incidence, and polarization of light, is a Schottky barrier with a corrugated interface (diffraction grating). The formation of the resonant photoresponse of this structure is determined by the excitation of surface plasma polaritons at the air–metal interface. The selective properties of a photodetector can be enhanced by optimizing its parameters (the depth of the relief, the thickness, and optical properties of the metal layer).[1] Under conditions of polariton resonance, the intensity of the electromagnetic field in the medium near the metal surface increases by orders of magnitude. This characteristic of plasma polaritons is responsible for their high sensitivity to changes in the optical properties of the medium near the metal surface. Here we attempt to utilize this characteristic of plasma polaritons to investigate the degradation of polarization-sensitive photodetectors based on Ag–GaAs(InP) Schottky barriers. Silver was selected to reduce the dissipative losses of plasma polaritons in the metal film and the associated decrease in the spectral width of the resonant photoresponse peak.

Measurements were made of the spectral photosensitivity curves under conditions where plasma polaritons were excited in Ag–GaAs Schottky diodes ($N_d \approx 4\times10^{15}$ cm^{-3}) with a diffraction grating at the interface and the change in the photosensitivity caused by prolonged exposure of the diodes to air was studied. A diffraction grating with period $a=826$ nm and depth $h=125$ nm was formed by holographic exposure of a photoresist to an Ar laser. A sinusoidal profile was transferred from the photoresist to the semiconducting substrate by chemical etching. Silver of varying thickness (20–70 nm) was then deposited on the substrate through the masks. The thickness of the silver was monitored by a piezoelectric transducer during the deposition process. The optical characteristics of the Ag films of varying thickness deposited on the quartz substrates at the same time as the structures were measured during their corrosion in air using multi-angle ellipsometry[2] and also using the transmission and reflection of film satellites on the quartz substrates.

Prior to deposition of the Ag film, the InP structures were oxidized in hot nitric acid to produce a tunnel-thin oxide of uniform composition,[3] to increase the effective height of the barrier, and to optimize the recombination and transport properties of the detectors, which were monitored by measuring the current-voltage and capacitance–voltage characteristics.

Figures 1 and 2 give experimental dependences of the photosensitivity of the GaAs and InP photodetectors, respectively, showing successive stages in their aging (degradation). The photoresponse peaks correspond to the re-emission of plasma polaritons propagating at the air–Ag interface by the diffraction grating to form a bulk light wave, followed by the generation of electron–hole pairs. The phase-matching condition for re-emission of plasma polaritons at the diffraction grating has the form

$$K_{\mathrm{pp}}=mG+\frac{2\pi}{\lambda}\sin\theta, \tag{1}$$

where K_{pp} is the wave vector of the plasma polaritons, $G=2\pi/a$ is the wave vector of a diffraction grating with the

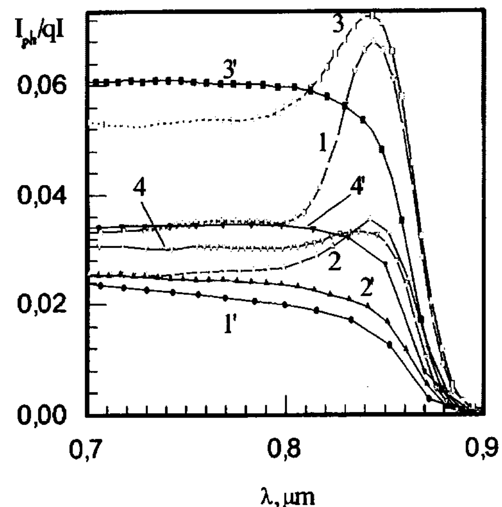

FIG. 1. Photocurrent spectra of Ag–GaAs structures recorded before exposure to air (*1*, *1'*), and two (*2*, *2'*), six (*3*, *3'*), and nine (*4*, *4'*) months after exposure for *p*- (*1–4*) and *s*-polarized light (*1'–4'*) and various metal layer thicknesses: 70 nm (*1*, *1'–3*, *3'*) and 20 nm (*4*, *4'*).

 © 1998 American Institute of Physics

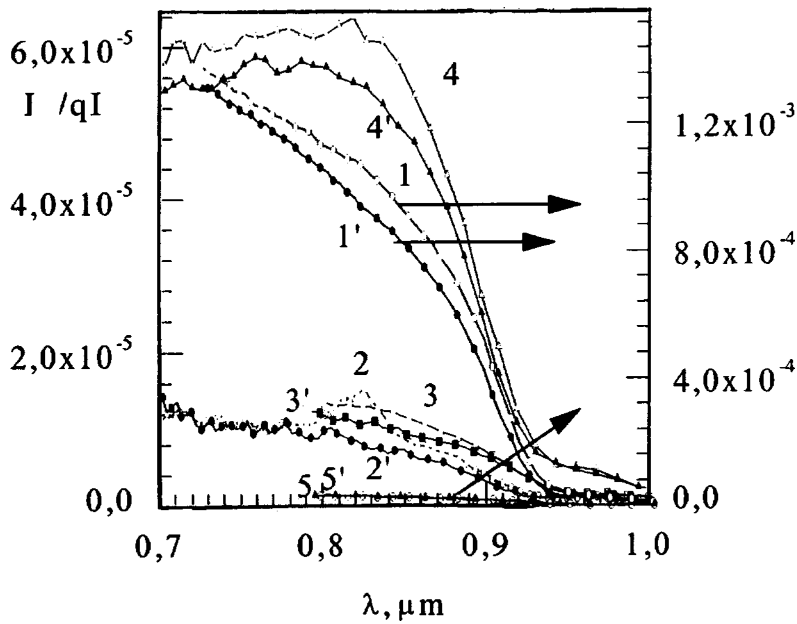

FIG. 2. Photocurrent spectra of Ag–CO–InP structures recorded before exposure to air (*1,1′,2,2′*), and three (*3,3′;5,5′*) and nine months after exposure (*4,4′*) for p-(*1–5*) and s-polarized (*1′–5′*) light and various metal layer thicknesses: 70 nm (*2,2′–4,4′*), 20 nm (*1,1′;5,5′*).

period $a, m = \pm 1, \pm 2 \ldots$ (the diffraction order), and θ is the angle of incidence of the light ($\theta = 0$ in our case). On exposure to air, which usually contains water vapor and hydrogen sulfide, the upper electrode (Ag) corrodes and becomes covered with a mat film (Ag_2S). The coating of the metal electrode with a surface film slightly changes the frequency of the plasma polaritons in accordance with the dispersion relation (see Ref. 4). The intensity peak of the polariton resonance and its half-width are determined by the imaginary part of the metal permittivity.[5] Thus, after exposure to air and a reduction in the thickness of the Ag film, the photosensitivity peak of the Ag–GaAs structure varies and its half-width increases. The nature of this dependence varies with the thickness of the metal film, decreasing for a thin film and varying nonmonotonically for a thick film.

In addition, the polarization sensitivity varies over the entire spectrum (and not only at the peak). In the region outside resonance interaction between the photodetector interface and s-polarized light is intensified when the electric field vector is parallel to the lines of the diffraction grating (curves *2* and *2′* for thick Ag films and curves *4* and *4′* for thin Ag films in Fig. 1). This tendency is increased with further aging of the photodetector (curves *3* and *3′* in Fig. 1).

A similar but more significant variation in the polarization sensitivity near the peak is observed for Ag–CO–n-InP structures (Fig. 2). These results confirm the view put forward in Ref. 6 that interfaces with InP are quantitatively more reactive than similar interfaces with GaAs. However, qualitatively the reactions at these interfaces are similar. The chemical reactions at the interfaces are highly sensitive to the presence of oxide, its local stoichiometry, and its pore content which facilitates the interdiffusion of metal and volatile components of the substrate (As, P). An absorbing Ag_2S layer clearly begins to form at projections of the grating relief and initially grows as an island-like film.[7] Each of these two processes makes some contribution to the corrosion of the metal electrode and the aging of the structures which are intensified under an applied bias and illumination. The barrier characteristics of the contact also vary in accordance with the microstructural transformations of the surface film: the forward current decreases and the ideality parameter of the current–voltage characteristic increases (Fig. 3), particu-

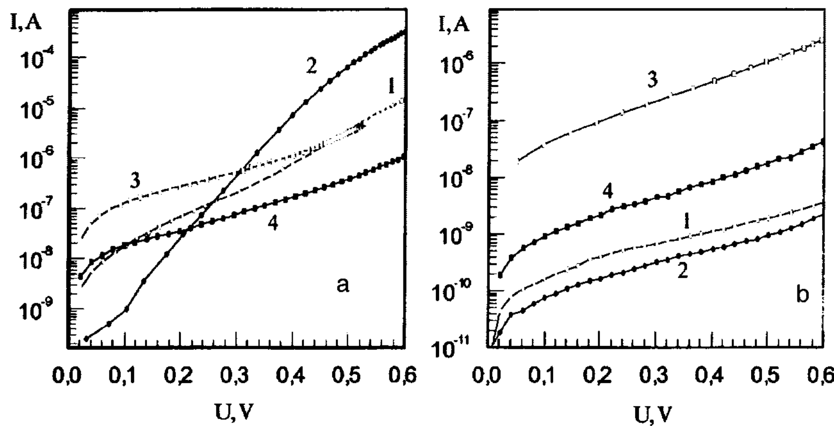

FIG. 3. Current–voltage characteristics of freshly prepared Ag–GaAs structures before (*1, 3*) and two months after (*2, 4*) exposure to air for metal layer thicknesses: a—70 nm and b—20 nm.

TABLE I. Optical parameters.

Sample No.	Freshly prepared Ag film						
	n_{Ag}		k_{Ag}		d_{Ag}, nm		Im ε
1	0.055		3.941		22.0		0.434
2	0.066		4.106		66.5		0.542
	Twelve months after deposition of Ag						
	n	k	d, nm	n_{Ag}	k_{Ag}	d_{Ag}, nm	Im ε
1	1.372	0.349	8.6	0.900	4.400	17.8	7.92
2	1.262	0.030	8.7	0.050	4.270	47.7	0.43

larly for a thin silver layer and a corrugated interface. Note that for a planar interface, the barrier parameters even initially improve: the ideality parameter decreases from 3.4 to 1.34 and the barrier height increases from 0.724 to 0.84 eV. This behavior of the barrier characteristics is clearly caused by the diffusion of silver toward the intermediate layer and the semiconductor, and also toward the outer surface of the film to form a layer of chemical compounds of silver. The reduction in the thickness of the metal layer and the changes in its optical parameters were determined by an ellipsometric method.

Ellipsometric measurements were made by a two-zone technique using an LÉF-3M ellipsometer ($\lambda = 632.8$ nm). The measurements were made using freshly prepared Ag films two days after deposition and then after twelve months. The parameters of a two-layer ''Ag+compound layer'' film given in Table I were obtained using a specially developed program to solve the inverse ellipsometric problem.[2] Also given are values of the imaginary part of the metal permittivity $\mathrm{Im}\,\varepsilon = 2nk$, which determines the intensity of the plasma polariton resonance. It can be seen that this parameter increases particularly significantly for thin Ag films, i.e., the resonance is suppressed, which is the main cause of the degradation. For thick Ag films however, Im ε decreases as the thickness of the metal layer decreases and increases the transmission of light to the semiconductor. The first factor is responsible for an increase in the polariton photosensitivity of the surface-barrier structures while the second factor causes an increase in the photosensitivity over the entire spectrum. The degradation processes of the Ag–GaAs(InP) barrier itself are superposed on these plasma resonance characteristics, which is responsible for such complex (nonmonotonic) variations in the photosensitivity of the Schottky diodes.

[1] L. V. Belyakov and O. M. Sreseli, Fiz. Tekh. Poluprovodn. **25**, 1281 (1991) [Semiconductors **25**, 773 (1991)].
[2] V. N. Antonyuk, N. L. Dmitruk, and M. F. Medvedeva, *Ellipsometry in Science and Engineering* [in Russian], Siberian Branch of the Academy of Sciences of the USSR, Novosibirsk (1987), pp. 66–71.
[3] O. Wad, A. Majerfeld, and P. Robson, Solid-State Electron. **25**, 381 (1982).
[4] N. L. Dmitruk, V. G. Litovchenko, and V. L. Strizhevskiĭ, *Surface Polaritons in Semiconductors and Insulators* [in Russian], Naukova Dumka, Kiev (1989).
[5] K. Holst and H. Raether, Opt. Commun. **2**, 312 (1970).
[6] T. Kendelenicz, N. Newman, R. S. List *et al.*, J. Vac. Sci. Technol. B **3**, 1206 (1985).
[7] D. K. Burge, J. M. Bennett, R. L. Peck *et al.*, Surf. Sci. **16**, 303 (1969).

Translated by R. M. Durham

Topological phase of optical vortices in few-mode fibers

A. V. Volyar, V. Z. Zhilaĭtis, T. A. Fadeeva, and V. G. Shvedov

Simferopol State University

(Submitted November 4, 1997)
Pis'ma Zh. Tekh. Fiz. **24**, 83–89 (April 26, 1998)

It has been found that as they propagate, the natural optical vortices of a few-mode parabolic fiber acquire a topological phase in addition to the dynamic phase. The magnitude of this phase is numerically equal to the polarization correction to the propagation constant of the CV and IV vortices. An analysis revealed that this phase is a new type of optical manifestation of the topological Berry phase. The already known Pancharatnam and Rytov-Vladimirskiĭ phases are associated with changes in the magnitude and direction of the angular momentum flow of the wave. In the fields of natural vortices of a few-mode fiber all the explicit parameters of the wave remain unchanged during propagation. However, the direction of the momentum density vector of the vortex undergoes cyclic variations along the trajectory of the energy flow line. These cyclic variations of the implicit vortex parameter are responsible for the new type of topological phase. Unlike the study made by van Enk (Ref. 6), where the topological phase was only related to the angular momentum for the lowest-order Gaussian beams ($l=\pm 1$), this topological phase describes guided vortices with any values l of the topological charge. The results can be used to estimate the stability of CV and IV vortices relative to external perturbing influences on the optical fiber. © *1998 American Institute of Physics.*
[S1063-7850(98)02804-3]

It was shown in Ref. 1 that a cyclic variation in the parameters of a quantum system leads to the formation of a topological phase in addition to the dynamic phase of the state function. Four manifestations of this effect are known in optics, caused by cyclic variations in the parameters of the system: 1) the polarization state of light—the Pancharatnam phase;[2] 2) the direction of the wave vector—the Rytov-Vladimirskiĭ phase;[3,4] 3) the Gaussian beam profile,[5,6] and 4) the squeezed state of light.[6] All these types of topological phase depend on cyclic variations in the explicit parameters of the system. In addition, the first three types of phases are conjugate with cyclic variations in the angular momentum flow of the optical field.[6] In the optics of multimode fibers these changes cause depolarization of the light.[7] However, in few-mode fibers we frequently encounter the situation where no visible changes in the field parameters are observed but the topological phase still accumulates. Attention to this factor was first drawn by the authors of Ref. 8, having qualitatively related the polarized correction to the propagation constants of the natural modes and the topological phase.

Our aim was to study the processes responsible for the appearance of the topological phase in fields of stable CV and unstable IV vortices of few-mode fibers.

It has been noted that one manifestation of the topological phase in a wave process is known in optics as the Rytov-Vladimirskiĭ effect.[3,4] In this effect, the wave acquires an additional phase shift γ as a result of a cyclic variation in the coordinates of the fixed Frenet trihedron of a nonplanar ray trajectory. The sign of this phase shift is determined by the direction of twist of the trihedron and by the direction of circulation σ_z of the state vector $\mathbf{e}(x,y,z)$ undergoing parallel transport along the ray trajectory.

In few-mode fibers ($l=1$) the natural modes can exist in the form of optical vortices[8,9] with the topological charge l and the direction of circulation of the circular polarization (helicity) σ_z. This pair of numbers (σ_z,l) characterizes two subgroups of vortices: CV and IV, having different propagation constants β. For CV vortices we have ($\sigma_z=+1$, $l=+1$) or ($\sigma_z=-1$, $l=-1$), and for IV vortices ($\sigma_z=+1$, $l=-1$) or ($\sigma_z=-1$, $l=+1$). For weakly guiding fibers, the difference between the refractive indices of the core and the cladding is small ($\Delta\rightarrow 0$), so that the CV and IV vortices have the same wave numbers $\tilde{\beta}$ (Ref. 10).

The optical vortices of a parabolic few-mode fiber propagate along its z axis without any change in the polarization state and intensity. Thus, it is not quite clear which cyclic variations in the wave parameters are responsible for the additional phase shift of the vortices which is characterized by the polarization correction to the propagation constant $\tilde{\beta}$.

We consider the evolution of the parameters of CV and IV vortices in a fiber with a parabolic refractive index profile $n^2(R)=n_{co}^2(1-2\Delta R^2)$, where Δ is the height of the refractive index profile and $R=r/\rho$ is the radial coordinate normalized to the radius ρ of the fiber core. It was shown in Ref. 10 that the density of the components of the Poynting vector for the CV and IV vortices may be expressed in the form

$$P_r=0,\quad P_\varphi=-2KF_l(R)G_l^{\pm}(R),$$

$$P_z=2K\frac{V}{\sqrt{2\Delta}}F_l(R), \tag{1}$$

where

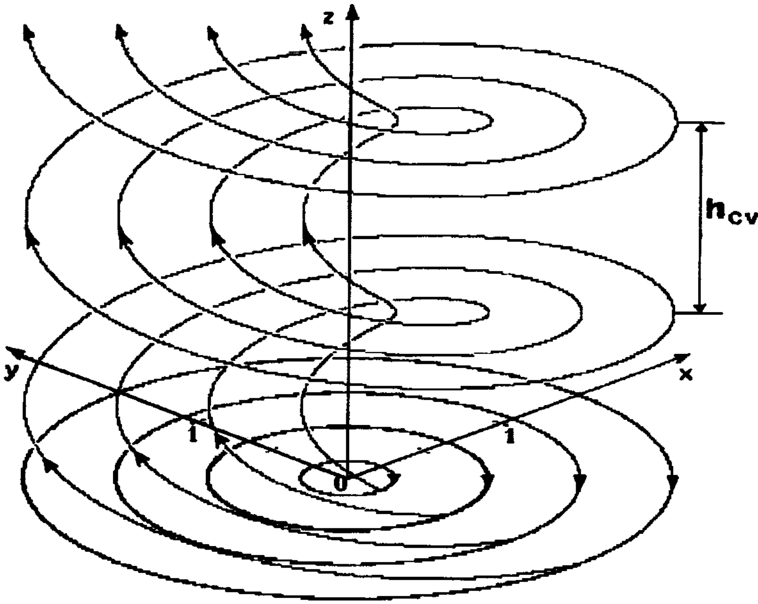

FIG. 1. Lines of energy flow **P** for a stable CV vortex.

$$F_l(R)=R^l\exp(-VR^2/2),\quad G_l^{\mp}=\frac{dF_l}{dR}\pm\frac{l}{R}F_l,$$

$$K=\frac{E_0^2}{2}n_{co}\sqrt{\frac{\varepsilon_0}{\mu_0}}\frac{\sqrt{2\Delta}}{V},$$

V is the waveguide parameter and the "$-$" and "$+$" signs in the function $G_l^{\mp}$ refer to the CV and IV vortices, respectively.

1. It follows from expression (1) that for a CV vortex the total energy flux P (and thus the angular momentum flux M_z) through the fiber cross section does not vary over the fiber length. We shall find the energy flow lines for a stable CV vortex. It can be shown that these lines are a family of helixes wound around the z axis of the fiber (Fig. 1). All the helixes lie on the surface of a right helicoid having a constant pitch:

$$h_{CV}=\frac{2\pi\rho}{\sqrt{2\Delta}}. \tag{2}$$

The pitch of the helixes (2) does not depend on the field characteristics of the CV vortex and is exclusively determined by the fiber parameters: the fiber radius ρ and the profile height Δ. Expression (2) will only be satisfied for those fibers for which the approximations of paraxial optics are valid. A comparison between expression (2) and the expression for the pitch of a light ray trajectory in a parabolic fiber (expression (2.38) in Ref. 10) reveals that these are exactly the same. Along the given helical trajectories, the direction of the momentum density vector undergoes cyclic variations. We shall find the topological phase associated with these cyclic variations of the implicit parameter of the vortex field. For this purpose we force parallel transport of the state vector **e** of the optical vortex along one of the helical lines of the energy flux density. Using the rules for the construction of a spherical map in parallel transport,[11] we find that the topological phase is given by:

$$\gamma=\varphi\left(1-\frac{P_z}{P}\right), \tag{3}$$

where $P^2=P_\varphi^2+P_z^2$ and φ is the azimuthal angle of a point on the energy flow line.

The specific topological phase (the topological phase per unit length) is written as

$$\beta_{CV}=\frac{\partial\gamma}{\partial z}=\left(1-\frac{P_z}{P}\right)\frac{\partial\varphi}{\partial z}=\frac{2\pi}{h_{CV}}\left(1-\frac{P_z}{P}\right)$$
$$=\frac{\sqrt{2\Delta}}{\rho}\left(1-\frac{1}{\sqrt{1+2\Delta R^2}}\right). \tag{4}$$

In multimode fibers it is always possible to select particular directions of energy propagation characterized by the ray trajectories of local plane waves.[10] In few-mode fibers all the energy flow lines are equally probable. Using expression (1), we find the specific topological phase β_{CV} averaged over the state **P**

$$\langle\beta_{CV}\rangle=\frac{\int_{\beta_{CV}}\beta_{CV}P\,d\beta_{CV}}{\int_{\beta_{CV}}P\,d\beta_{CV}}=-\frac{(\sqrt{2\Delta})^3}{2\rho V}(l+1). \tag{5}$$

It follows from expression (5) that the specific topological phase of the CV vortex, averaged over the state **P**, characterized by the quantum numbers $(+l,+1)$ or $(-l,-1)$, is numerically equal to the polarization correction $\delta\beta_l$ to the propagation constant $\tilde{\beta}$ for even and odd HE modes which may form the CV vortex (Table 14.1 in Ref. 10).

2. It can be shown from expression (1) for an IV vortex that the angular momentum flow through the fiber cross section for any z coordinate is zero. We estimate the specific topological phase of an unstable IV vortex. The energy flow lines of an IV vortex also have the form of helical curves wound around the z axis (Fig. 2). The pitch of the helical lines now also depends on the helix radius R:

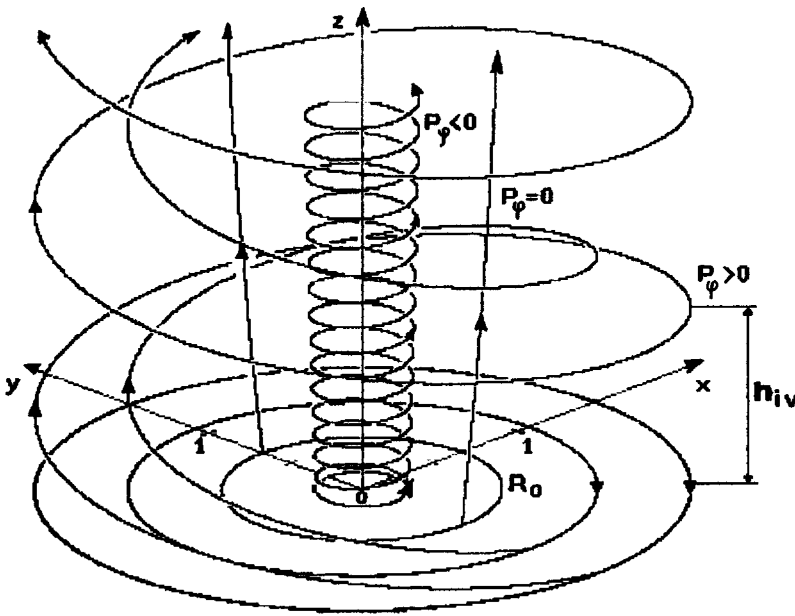

FIG. 2. Lines of energy flow **P** for an unstable IV vortex.

$$h_{IV}=\frac{2\pi\rho}{\sqrt{2\Delta}}\frac{1}{1-\frac{R_0^2}{R^2}},\quad R_0=\sqrt{\frac{2l}{V}}. \tag{6}$$

This implies that for small radii ($R\rightarrow 0$) the pitch of the helixes is $h_{IV}\rightarrow 0$, i.e., unlike the CV vortex, the point $R=0$ is a singular point of the energy flow of IV vortices, at which the winding pitch of the helixes tends to zero and the specific topological phase is $\beta_{IV}\rightarrow\infty$. The line R_0 is also a singular line of the field of IV vortices since the value of β_{IV} changes sign on it. It can be seen from Fig. 2 that the radius R_0 corresponds to a family of energy flow lines with zero twist, the pitch of the helixes increases without bound ($h_{IV}\rightarrow\infty$ for $R\rightarrow R_0$), and the z component of the angular momentum density m_z of the IV vortex is zero. This physical situation arises because of the structural characteristics of an IV vortex. The fact that the sign of the helicity σ_z is opposite to that of the topological charge l formally corresponds to the fact that the sign of the polarization component of the angular momentum of an IV vortex is opposite to the orbital component of the angular momentum m_z. The geometric structure of an IV vortex is topologically nonuniform. Thus, it is difficult to determine the state-averaged topological phase by the method described above. These difficulties can be eliminated if we consider a multimode fiber with a fairly large waveguide parameter V. In this case, the radius of the zero energy flow line is $R_0\rightarrow 0$, i.e., two singular points with different types of singularity are superposed. This annihilation of the singularities corresponds to a substantial reduction in the contribution of the polarization component of the angular momentum compared with the orbital component. The pitch of all the energy flow helixes is then $h_{IV}\rightarrow h_{CV}$ and the specific topological phase is $\beta_{IV}\rightarrow\beta_{CV}$. The CV vortex may be represented as a superposition of even and odd $HE_{l+1,m}$ modes with the azimuthal index $l_{CV=l+1}$ whereas the IV vortex is a superposition of even and odd $EH_{l-1,m}$ modes with the azimuthal index $l_{IV}=l-1$ (Ref. 9). Thus, by making the substitution $l_{CV}\rightarrow l_{IV}$, we obtain the average specific topological phase of an IV vortex in the form

$$\langle\beta_{IV}\rangle=\frac{(\sqrt{2\Delta})^3}{1\rho V}(l-1). \tag{7}$$

The difference between the signs of the topological phases for the CV and IV vortices in expressions (5) and (7) arises because for the IV vortex with parallel transport of the state vector, the direction of twist of the helixes and the direction of circulation of the polarization are of different sign.[1,3]

It follows from expression (7) that the specific topological phase $\langle\beta_{IV}\rangle$, averaged over state **P**, characterized by the states $(+l,-1)$ or $(-l,+1)$, is numerically equal to the polarization correction $\delta\beta_2$ to the propagation constant for the even and odd EH modes (Table 14.1 in Ref. 10).

For a few-mode fiber ($l=1$) we have from expression (7) $\langle\beta_{IV}\rangle=\delta\beta_2=0$ because the angular momentum flow of an IV vortex is zero. Thus, the field of an IV vortex has the propagation constant $\tilde{\beta}$. Expressions (5) and (7) describe the interrelation between the topological phase and the angular momentum density for any topological charge l of the waveguide vortices. The difference between the propagation velocities of the vortices, expressed in terms of the topological phase of the field, is a consequence of the spin-orbit interaction in the field of CV and IV vortices.

[1] M. Berry, Proc. R. Soc. London, Ser. A **392**, 40 (1984).
[2] S. Pancharatnam, Proc. Ind. Acad. Sci. A **44**, 247 (1956).
[3] S. M. Rytov, Dokl. Akad. Nauk SSSR **28**, 263 (1938).
[4] V. V. Vladimirskiĭ, Dokl. Akad. Nauk SSSR **31**, 222 (1940).
[5] D. Subbararo, Opt. Lett. **20**, 2162 (1995).
[6] S. J. van Enk, Opt. Commun. **102**, 59 (1993).
[7] A. V. Volyar, T. A. Fadeeva, and Kh. M. Reshitova, Pis'ma Zh. Tekh. Fiz. **23**(5), 70 (1997) [Tech. Phys. Lett. **23**, 198 (1997)].
[8] B. Ya. Zel'dovich and V. S. Liberman, Kvant. Élektron. (Moscow) **17**, 493 (1990) [Sov. J. Quantum Electron. **20**, 427 (1990)].

[9] A. V. Volyar and T. A. Fadeeva, Pis'ma Zh. Tekh. Fiz. **22**(8), 63 (1996) [Tech. Phys. Lett. **22**, 333 (1996)].
[10] A. W. Snyder and J. D. Love, *Optical Waveguide Theory* (Methuen, London, 1984; Radio i Svyaz, Moscow, 1987)
[11] V. F. Kogan, *Principles of Surface Theory*, Part 1 [in Russian] OGIZ, (1947).

Translated by R. M. Durham

Fabrication of regular three-dimensional lattices of submicron silicon clusters in an SiO_2 opal matrix

V. N. Bogomolov, V. G. Golubev, N. F. Kartenko, D. A. Kurdyukov, A. B. Pevtsov, A. V. Prokof'ev, V. V. Ratnikov, N. A. Feoktistov, and N. V. Sharenkova

A. F. Ioffe Physicotechnical Institute, Russian Academy of Sciences, St. Petersburg

(Submitted November 3, 1997)
Pis'ma Zh. Tekh. Fiz. **24**, 90–95 (April 26, 1998)

Silicon is now the most important material in modern solid-state electronics. Regular systems of silicon nanoclusters containing up to 10^{14} cm^{-3} elements were obtained in a sublattice of opal (SiO_2) voids. By using three-dimensional dielectric matrix-carriers similar to opal, it may be possible to obtain three-dimensional ensembles of semiconductor nanodevices. Various parameters of these ''opal-silicon'' nanocomposites were measured. © *1998 American Institute of Physics.* [S1063-7850(98)02904-8]

One method of fabricating three-dimensional systems of semiconductor nanodevices with a high bulk density is a matrix method, using dielectric matrices having a regular sublattice of submicron channels and voids in which three-dimensional lattices of different nanostructures containing up to 10^{14} cm^{-3} elements can be formed. Sublattices of Te, GaAs, HgSe, and CdS clusters have now been obtained in opals.[1,2] Regular three-dimensional lattices of silicon nanostructures based on matrices of synthetic opals may prove to be invaluable objects for microelectronics as the basis of two-electrode semiconductor devices with $p-n$ junctions or Schottky diodes. Such a composite would have the advantage of a large junction area per unit volume (up to $10\ \mathrm{m^2/cm^3}$). This would allow the fabrication of Si devices operating at current densities between three and four orders of magnitude lower than those in conventional planar systems.

Here we report the synthesis of opal-silicon composites for the first time. Single crystals of synthetic opals exhibiting an optically perfect structure were obtained using the technology described in Ref. 3. The opals consist of SiO_2 spheres which form a face-centered cubic lattice with sublattices of voids between the spheres with a volume of up to 26% and capable of being filled by other substances.[4] The fabrication technology allows the parameters of the opals to be varied by varying the sphere sizes and their porosity. Here we used opals consisting of SiO_2 spheres 250 nm in diameter.

Thermal chemical vapor deposition (thermo-CVD) technology was used to incorporate silicon in the opal samples. The CVD reactor was a quartz tube with an external heater through which a mixture of monosilane (5%) and argon gas was passed. An opal wafer was positioned perpendicular to the gas stream. The design of the reactor prevented any gas from going past the wafer. As a result of the thermal dissociation of the silane, a silicon film was deposited inside the opal on the inner surfaces of the pores. The dissociation conditions were isothermal. The pressure gradient created in the sample by the high hydraulic resistance of the opal resulted in nonuniform filling of the matrix. The filling profile of the opal pores over the thickness of the sample was investigated by measuring the x-ray photoelectric absorption. The measurements were made with a DRON-2.0 diffractometer using monochromatic Cu Kα_1 radiation (beam size 0.1×1 mm). It was observed that a sample 300 μm thick had a region 120 μm thick 100% filled with Si, the degree of filling of the pores then decreased linearly to 0% over 80 μm, and the remaining 100 μm was unfilled. In order to obtain uniformly filled samples, the pressure gradient must clearly be counterbalanced by an opposite temperature gradient. The structure of the samples was investigated by x-ray structural analysis and Raman spectroscopy. The samples underwent ion etching (Ar^+, $V=5$ kV, $I=10\ \mu$A) to prevent the Raman spectra from being influenced by the silicon film formed on the outer surface of the opal during the growth process. We used a VUP-4 vacuum system fitted with an ion polishing attach-

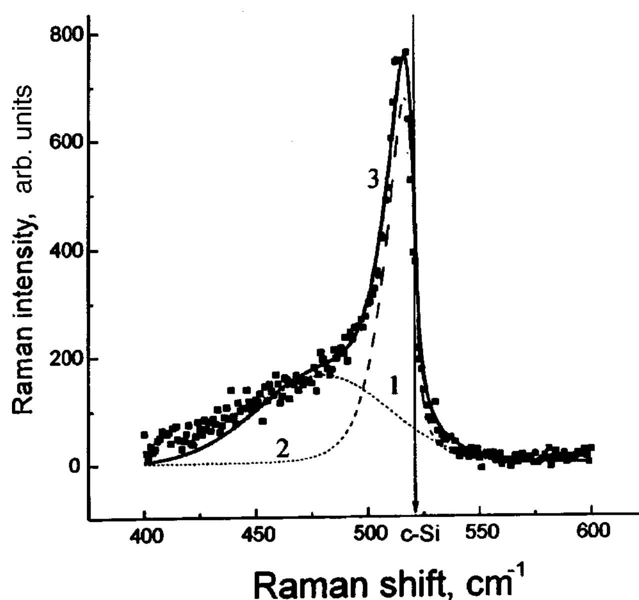

FIG. 1. Diffraction patterns: *1*—diffraction pattern of unfilled opal, *2*—diffraction pattern of opal-silicon nanocomposite, and *3*—bar diagram of crystalline silicon .

 © 1998 American Institute of Physics

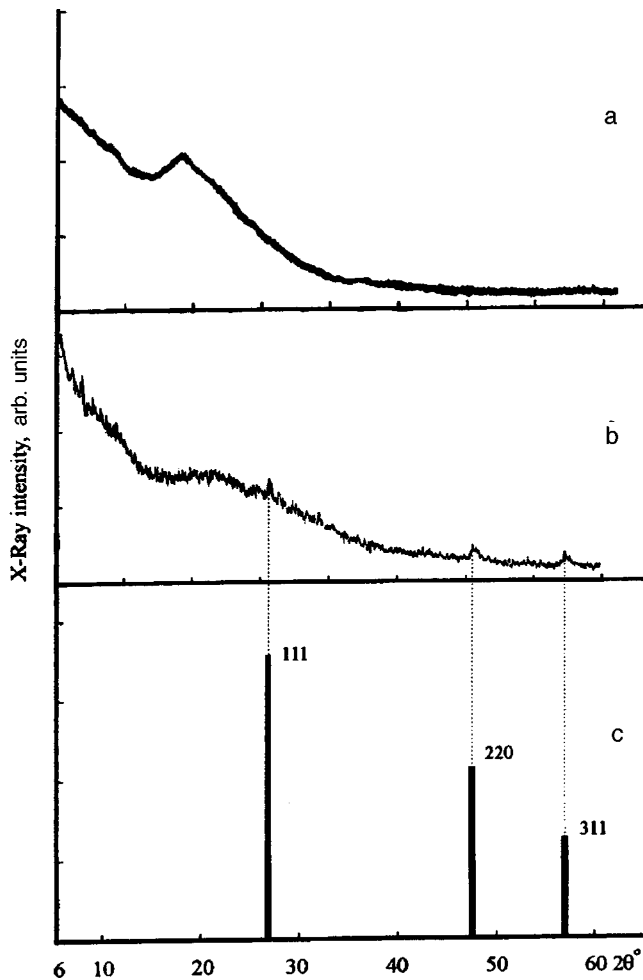

FIG. 2. Raman spectrum of opal-silicon nanocomposite: a—amorphous component; b—nanocrystalline component, and c—"sum" spectrum. *c*-Si is the crystalline silicon line.

ment, manufactured by the Institute of Technical Physics, Hungary.

The measurements showed that the Raman spectrum contains a broad ($\approx 70\ \mathrm{cm}^{-1}$ half-width) line with a maximum near $480\ \mathrm{cm}^{-1}$ characteristic of silicon with an amorphous structure.[5]

In order to obtain silicon crystallites, the sample was annealed in a sealed, evacuated ampoule at $t = 800\ ^\circ\mathrm{C}$ for 10 min. The Raman spectrum of the annealed samples is shown in Fig. 1. It can be seen that against the background of a broad amorphous component there is a narrower line shifted toward low frequencies relative to the Raman-active TO phonon mode of the crystalline silicon. This transformation of the spectrum indicates that a nanocrystalline silicon phase is formed.[5] An analysis of the Raman spectra using the model of strong spatial confinement of optical phonons found in nanosize crystallites[6–8] yielded an estimate of their average size ($L \approx 40$ Å) and bulk fraction ($\chi = 52\%$) in a silicon two-phase (amorphous-nanocrystalline) system.

Figure 2 shows x-ray diffraction patterns of an opal sample before filling with silicon and an annealed sample. The diffraction pattern of the sample before annealing is similar to that of the unfilled opal. The diffraction patterns

TABLE I. Results of calculations.

Reflection	$2\theta^\circ$	β_{mod}, rad	b_{stand}, rad	D, Å
111	28.42	7.8×10^{-3}	2.18×10^{-3}	190 ± 25
220	47.20	12×10^{-3}	1.92×10^{-3}	130 ± 10

were recorded using a DRON-2 diffractometer (Cu-K_α radiation).

The dimensions of the coherent scattering region in the sample were determined by an approximation method. For the calculations it was assumed that the physical broadening (β) of the diffraction lines is only caused by the small size of the coherent scattering region. Powder from well-crystallized silicon was used as a standard.

The calculations were made using the results of measurements of the "half-width" of the 111 and 220 silicon reflections. The doublet component α_1 was isolated for the 220 reflection (see Table I).

The value of D_{111} may be overestimated because of the superposed diffuse opal halo which creates an increased scattering background near the 111 silicon reflection.

The difference between the results of determining the sizes of the silicon crystallites from the Raman spectra and the diffraction patterns in the opal may be attributed to the neglected influence of the stresses produced during crystallization and also to large dispersion of the silicon cluster sizes.

It has thus been shown that CVD technology followed by annealing can be used to synthesize a new composite material—nanocrystalline silicon in a regular dielectric matrix based on synthetic opal. It is suggested that the difference in the dimensions of the nanocrystalline Si obtained by independent methods is attributable to the dispersion of D and the neglect of the stresses in the crystallites. Some dispersion of the crystallite sizes (between tens and hundreds of angstrom) has been observed. It has been established that the material is nonuniformly distributed over the thickness of the sample, so that any required degree of filling can be obtained by varying the size of the matrix.

The problem was formulated and discussed in detail jointly with I. G. Grekhov to whom the authors express their thanks.

[1] V. N. Bogomolov, S. S. Ktitorov, D. A. Kurdyukov *et al.*, Abstracts of Papers presented at the International Symposium on *Nanostructures: Physics and Technology,* St. Petersburg, 1995, pp 189–192.

[2] V. N. Astratov, V. N. Bogomolov, A. A. Kaplyanskii *et al.*, Nuovo Cimento D **7**, 1349 (1995).

[3] V. N. Bogomolov, D. A. Kurdyukov, A. V. Prokof'ev, and S. M. Samoĭlovich, JETP Lett. **63**, 520 (1996).

[4] V. N. Bogomolov and T. M. Pavlova, Fiz. Tekh. Poluprovodn. **29**, 826 (1995) [Semiconductors **29**, 428 (1995)].

[5] Z. Igbal and Veprek, J. Phys. C **15**, 377 (1982).

[6] L. H. Campbell and P. M. Fauchet, Solid State Commun. **58**, 739 (1986).

[7] A. B. Pevtsov, V. Yu. Davydov, N. A. Feoktistov, and V. G. Karpov, Phys. Rev. B **52**, 955 (1995).

[8] V. G. Golubev, V. Yu. Davydov, A. B. Pevtsov, and N. A. Feoktistov, Fiz. Tverd. Tela (St. Petersburg). **39**, 1348 (1997) [Phys. Solid State **39**, 1197 (1997)]

Translated by R. M. Durham